School of Civil and Mechanical Engineering

# Computational modelling of iron-ore mineralisation with stratigraphic permeability anisotropy

Juan Felipe Giraldo Avila

This thesis is presented for the Degree of
Doctor of Philosophy
of
Curtin University of Technology

June 2023

# Acknowledgements

I want to express my gratitude to my supervisor, Prof. Victor Calo, for his guidance and feedback throughout my research journey; to my external advisor from CSIRO, Dr. Thomas Poulet, for his significant contributions and insights; and to Prof. Dimple Quey, whose support and confidence in my work were invaluable during this process.

I am grateful to my mother and sisters for always being my source of motivation and encouragement. Their care has been a wellspring of strength. I also want to thank my friends for their companionship and support regardless of the distance. Finally, I want to acknowledge my partner, Milena, for her love, patience, and unconditional presence by my side.

This work is supported by the close collaboration between Curtin University and CSIRO under the CSIRO DEI FSP postgraduate top-up scholarship (Grant no. 50068868). I gratefully acknowledge Roberto Rocca Education Program for its support during this research.

# Abstract

Minerals represent an ever-growing component of the global economy, primarily fuelled by the escalating need for new deposits stemming from, for example, the ongoing energy transition to batteries. Many sought-after minerals can be found in sedimentary basins, and exploration techniques for those valuable deposits require a solid understanding of the movement of mineralising fluids in such environments; this understanding is crucial for developing genetic models that explain the origin of deposits and for more direct prospecting purposes. A quantitative examination of subsurface fluid transport in sedimentary basins is also critical in other areas, including conventional and unconventional energy sources, carbon capture, geothermal energy, and nuclear waste disposal.

Iron ore is a critical commodity due to its essential role in the steel industry, which sustains the world's industrial base. While the major iron ore regions have been identified, such as Australia's Hamersley Basin, no agreed-upon genetic model for iron ore exists. This lack of consensus complicates the prediction of resource volume and mineral location, thereby impeding efforts to reduce exploration costs and environmental impacts. In conjunction with observational and experimental studies, quantitative modelling techniques have effectively analysed flow and transport in sedimentary basins across geological time and length scales. These methodologies have shown that, for some minerals, regional patterns of fluid flow controlled the transport of minerals from specific ore deposits. However, for iron ore, these methodologies have yet to offer definitive evidence regarding the nature of the fluids involved and the precise processes underlying their formation. Iron ore deposits display hypogene and supergene characteristics in different places, leaving uncertain the direction of fluid flow and the exact mechanisms, fluid composition, and physical and chemical processes involved. Regardless of the complex chemical interactions involved, it is widely acknowledged that fluid transport plays a pivotal role in forming iron ore deposits, necessitating

a deeper understanding of these processes. Addressing this issue involves various challenges, including managing strong anisotropy following the rock strata, the need for a small-scale homogenisation model, and the high permeability contrast between Banded Iron Formation (BIF) and shale units at a larger scale.

This thesis introduces a robust computational framework to model fluid transport in porous media. This work's findings suggest that the transport alone can explain forming Banded Iron Formation (BIF) supergene Martite-Goethite ore deposits. A simplified flow model uses a potential function for the implicit representation of strata, which accurately orients the permeability tensor from a paleo reconstruction of all geological features, including topography and strata properties. The model accounts for the permeability anisotropy of the paleostratigraphy, which allows greater permeability along the strata than across it, a unique feature that influences the supergene enrichment transport process and the mineralisation pattern distribution.

The proposed physical model addresses two critical computational challenges: the pure transport problem, which describes variations in concentration for the species responsible for the formation of ore deposits, and the highly anisotropic and heterogeneous diffusion, which shapes the transport problem's vector field. A novel, numerically stabilised finite element method is introduced to overcome these challenges, developed within a variational multiscale framework. This innovative method achieves coarse-scale approximations by minimising the residual on a dual discontinuous Galerkin norm and derives the fine-scale approximation using the variational multiscale framework. The stability of solutions across each adaptive mesh iteration is ensured through a symmetric saddle-point formulation and a posterior error indicator that guides automatic adaptivity. The model effectively handles sharp permeability changes, eliminating the need for stabilisation terms in the variational formulation and reducing computational effort through an optimal adaptive refinement scheme.

The powerful predictive capacity of this methodology enables more precise, targeted drilling, thereby narrowing down prospective areas and reducing exploration costs. Moreover, the broad applicability of this methodology extends to other commodities in sedimentary basins involving supergene processes, enriching our understanding of various genetic models.

# Contents

**Acknowledgements** iii

**Abstract** v

**1 Introduction** 1

1.1 Iron-ore genetic model . . . . . 1

1.1.1 Geological understanding . . . . . 1

1.1.2 Numerical approach . . . . . 4

1.2 Thesis overview . . . . . 9

1.3 Motivation and Objectives . . . . . 9

1.4 Structure of the thesis . . . . . 11

**2 Numerical framework for steady convection-diffusion-reaction problems** 13

2.1 Continuous problem and its discretisation . . . . . 14

2.1.1 Convection-diffusion-reaction equation . . . . . 14

2.1.2 Discontinuous Galerkin (dG) discretisation . . . . . 15

2.2 Residual minimisation formulation . . . . . 18

2.3 A variational multiscale interpretation of the residual minimisation framework . . . . . 19

2.3.1 A multiscale partition of the trial and test spaces . . . . . 19

2.3.2 Adjoint multiscale reconstruction . . . . . 21

2.4 Numerical examples . . . . . 24

2.4.1 Diffusion in a domain with a re-entrant corner . . . . . 25

2.4.2 Diffusion in a 3D domain with a Fichera corner . . . . . 26
2.4.3 Heterogeneous Diffusion problem . . . . . 27
2.4.4 Strongly anisotropic diffusion . . . . . 28
2.4.5 3D Eriksson-Johnson problem . . . . . 30
2.5 Extension to nonlinear conservation laws . . . . . 31
2.5.1 Discontinuous Galerkin discretisation . . . . . 32
2.5.2 Residual minimisation formulation . . . . . 33
2.5.3 Nonlinear variational multiscale method . . . . . 34
2.5.4 Adjoint multiscale reconstruction . . . . . 36
2.5.5 Burgers' equation . . . . . 36
2.6 Concluding Remarks . . . . . 39

**3 Unsteady convection-diffusion-reaction problems 41**
3.1 Problem definition . . . . . 42
3.2 Discontinuous Galerkin discretisation and time marching . . . . . 43
3.2.1 Space Semi-discretisation . . . . . 43
3.2.2 Backward Euler time discretisation . . . . . 45
3.2.3 Second-Order Backward Differencing Formula . . . . . 47
3.3 Fully Discrete Residual minimisation . . . . . 47
3.4 Variational multiscale reconstruction . . . . . 49
3.5 Numerical examples . . . . . 50
3.5.1 Heat equation (2D) . . . . . 50
3.5.2 Advection-diffusion problem . . . . . 52
3.5.3 Rotating flow transporting a Gaussian profile . . . . . 54
3.6 Unsteady nonlinear systems . . . . . 57

**4 A paleo stratigraphic model with anisotropic permeability for the genesis of martite-goethite iron-ore deposits 63**
4.1 Permeability anisotropy . . . . . 64
4.2 Numerical simulation . . . . . 65
4.3 Preprocessing . . . . . 68

4.4 Results . . . . . 70
4.4.1 Brockman Syncline deposit . . . . . 70
4.4.2 Marandoo deposit . . . . . 74
4.4.3 South Flank deposit . . . . . 76
4.5 Discussion . . . . . 78

**5 Conclusions and research perspectives** **83**
5.1 Concluding Remarks . . . . . 83
5.2 Research Outlook . . . . . 85

**Appendices** **87**

**A Proof. Discrete coercivity and inf-sup condition for $B_{h,\tau}$** **89**
A.1 Discrete coercivity . . . . . 89
A.2 Inf-sup condition . . . . . 90

**B Quantifying the fit between simulations and observations** **92**

**Bibliography** **95**

# List of Figures


1.1 Detailed image of a banded iron formation (BIF) from Hamersley Basin, Western Australia, highlighting the fine banding and contrasting porosity between darker magnetite and lighter chert/-carbonate/silicate bands. The ellipse at the centre sketches the permeability tensor, indicating the longitudinal ($k_{\parallel}$) and transverse ($k_{\perp}$) permeability components. . . . . 2

1.2 Simplified version of a typical geological cross-section from the Brockman Syncline BS4 deposit, with drill-hole traces, shown in Sommerville et al. [2014]. Mineralised areas include hydrated and non-hydrated domains. . . . . 4

2.1 Notation of the element interface. . . . . 16

2.2 Solution for the re-entrant corner problem for different refinement levels . . . . . 25

2.3 $\mathbb{V}_h-$ & $L_2-$norm convergence for Laplace problem . . . . . 25

2.4 $\mathbb{V}_h-$ and $L_2-$norm convergence for Fichera corner, $q = \frac{1}{10}$ . . . . 27

2.5 $\mathbb{V}_h-$ and $L_2-$norm convergence for Fichera corner, $q = \frac{1}{3}$ . . . . . 27

2.6 $\mathbb{V}_h-$ & $L_2-$norm convergence for heterogeneous diffusion problem 28

2.7 Coarse- & fine-scale solutions with final mesh for strongly anisotropic diffusion problem with $r = 10^6$ & $p = 1$ . . . . . 29

2.8 $\mathbb{V}_h-$ and $L_2-$norm convergence for anisotropy ratio $r_\kappa = 10^4$. . . 30

2.9 $\mathbb{V}_h-$ and $L_2-$norm convergence for anisotropy ratio $r_\kappa = 10^6$. . . 30

2.10 Convergence in $L_2$ norm for the 3D Eriksson-Johnson problem . . 31

2.11 $\mathbb{V}_h-$ and $L_2-$norm convergence for 3D Eriksson-Johnson problem, $p = 1, 3$ . . . . . 31

2.12 $\mathbb{V}_h-$ and $L_2-$norm convergence for 3D Eriksson-Johnson problem, $p = 2, 4$ . . . . . 31

2.13 Solution for Burgers' equation for $\kappa = 10^{-3}$ & $p = 1$ . . . . . 36

2.14 Solution for the isotropic Burgers equation for different refinement levels at $\kappa = 10^{-3}$ . . . . . 37

2.15 Convergence plots for Burgers' equation in the $L_2$ and $\mathbb{V}_h$ norms, $p = 1, 3$ . . . . . 37

2.16 Convergence plots for Burgers' equation in the $L_2$ and $\mathbb{V}_h$ norms, $p = 2, 4$ . . . . . 37

2.17 Coarse-scale solution and scale approximations for different diffusivities. (top: $\kappa = 10^{-2}$, middle: $\kappa = 10^{-3}$ ,bottom: $\kappa = 10^{-4}$). . . 38

2.18 Solution for the Burgers equation for different refinement levels at $\kappa = 10^{-2}$ . . . . . 39

3.1 BDF1 spatial convergence using fixed time step and uniform meshes. 51

3.2 BDF2 spatial convergence using fixed time step and uniform meshes 51

3.3 Time convergence for backward Euler (BDF1) and BDF2 for a fixed mesh. . . . . 52

3.4 Mesh refinement $\tau = 0.005$, $T = 0.1, p = 1$. . . . . 53

3.5 Spatial convergence for adaptive refinement (BDF1 : $\kappa = 10^{-2}$,$T = 0.1$, $\tau = 0.005$) . . . . . 53

3.6 Energy norm convergence in space ($\tau$) for adaptive refinement (BDF2: $T = 0.1$, $\tau = 0.005$). Left: $\kappa = 10^{-2}$ for p=1,2. Right: $\kappa = 10^{-3}$ for p=2. Bottom: $\kappa = 10^{-4}$ for p=2 . . . . . 54

3.7 Solution convergence to the steady Eriksson–Johnson solution. . . 55

3.8 Time evolution $p = 1$ ($T = \pi, \tau = \pi/512$). . . . . 55

3.9 Computational cost [s] vs total degrees of freedom. . . . . 56

3.10 Bratu's bifurcation diagram for T=1.0 and $\tau$=0.1. . . . . 59

3.11 Solution's temporal evolution for $\lambda = 2$ for the lower and upper branches. . . . . 60

4.1 Simplified detail cross section of the Marra Mamba formation redrawn from [Knight et al., 2018], schematically represented from the original data of [Kepert, 2018]. The mineralisation is covering the whole layer in parts but only some sub-layers in others. . . . 65

4.2 Input potential field (top) and mesh (bottom) to the supergene mineralisation model. We generate them from the digitised points (red, top figure) representing the stratigraphic layers, either as isopotential values or geometrical boundaries, using respectively *LoopStructural* and *gmsh* programmatically. . . . . 69

4.3 Snapshots, respectively shown from (a) to (d), of cropped tracer distribution for paleo water table altitude $a = 680m$ at $t = t_1 < t_2 < t_3 < t_4$ during a simulation, highlighting the propagation from the paleo water table (top of the model) and following the strata. 70

4.4 Tracer distribution for paleo water table altitude $a = 680m$, superimposed over Figure 1.2, using a single set of longitudinal and transverse permeability values in all BIF areas. We define mineralisation by proxy in the area, shaded in red, where the tracer concentration exceeds 20% of the maximal input. . . . . 71

4.5 Decreased permeability above dolerite sill; (a) flow vectors and final mesh after automatic refinement for hydraulic pressure computation; colours display model's arbitrary partition regions highlighting stratigraphy; (b) tracer concentration and mesh after automatic refinement for the final transient transport; (c) tracer concentration, cropped and superimposed over geological cross section for comparison, showing the mineralised areas in orange below the existing topography and in pink in the paleo-reconstruction. The orange colour enhances the visual contrast between the simulation results and the reference geological cross section. . . . . 72

4.6 Sensitivity analysis for water table level $a$, showing tracer results for $a = 650$, 680, 700 and $750m$. . . . . 73

4.7 Permeability anisotropy $r$ sensitivity, tracer results for BIF ratios $r = 1$, 20, 100, while other parameters remain unchanged, superimposed over the geological cross section. . . . . 74

4.8 Marandoo scenario from [Morris, 1982], 1.5x vertical exaggeration. (a) Redrawn version of the original, with observed and inferred mineralisation areas marked, and (b) new proposed model, only altering the geometrical configuration of the Marra Mamba formation around the paleo-topography at the southern end of the cross section to add an extra undulation, as Morris suggested elsewhere on the same figure. . . . . 75

4.9 Simulation results from initial configuration of Figure 4.8b; mineralisation pattern below current topography is restricted to the upper part of the Marra Mamba Iron Formation and matches therefore observations (see Figure 4.8a). Note, however, the main difference with Figure 4.8a above current topography, where mineralisation covers most of the unit. . . . . 76

4.10 Model of a section of the South Flank deposit, redrawn from [Pering et al., 2020], showing localized mineralisation mainly within three geological units. The dashed line indicates the upper part of West Angela 2, above which we do not capture the stratigraphy since not relevant for this example. We extrapolate the stratigraphic model above the current topography to suggest an interpreted configuration that could be responsible for the observations. 77

4.11 Two tracer concentrations scenarios, see Figure 4.10. (a) Geological units from West Angela 1 downwards have the same anisotropic permeability. (b) Thin shale layers added at interfaces between West Angela 1, Newman 3, Newman 2 and Newman 1 sub-units. . 78

4.12 Analogy with fluid pipes to highlight the conceptual effect of paleo water table level given a particular stratigraphic geometry and strong permeability anisotropy. The scenario at the centre leads to visible mineralisation (i.e., below topography) only in one part of the model, whereas the other scenarios do not allow for it. . . 79

4.13 Schematic drawing of reconstructed strata for the scenario of Section 4.4.1, to highlight the role of the paleo water table (horizontal dashed line) as top boundary condition for the fluid flow (black arrows), whose direction and intensity is strongly affected by the strata orientation and anisotropy coefficient. . . . . 80

B.1 Quantifying the fit between simulation (red) and reference (blue) areas of mineralisation. Image processing allows to classify the match in zones of True Positive (TP), False Positive (FP), True Negative (TN) and False Negative (FN). . . . . 92

# Chapter 1

# Introduction

## 1.1 Iron-ore genetic model

The increasing demand for minerals highlights their significant contribution to diverse global industry sectors, contributing to economic growth and driving the transition towards sustainable energy practices [Ramanaidou & Wells, 2014]. Iron, in particular, plays a crucial role in the steel industry as a critical component for various industrial applications, including construction, transportation, and manufacturing. The heightened reliance on this mineral has drawn attention to basin-hosted iron systems, emphasising the importance of comprehending their geological settings and ore-forming processes [USGS, 2022].

### 1.1.1 Geological understanding

The Hamersley Basin in Western Australia hosts some of the largest iron-ore deposits globally [Australia, 2021; USGS, 2022]. These deposits can be classified into three groups: 1) banded iron formation (BIF) hosted iron ores, 2) channel iron deposits (CID), and 3) detrital iron deposits (DID) with relatively lower abundance [Ramanaidou & Wells, 2014]. The combined CID and DID deposits account for approximately 20 billion tonnes [Knight et al., 2018], while the BIF-hosted or bedded iron deposits hold 50 billion tonnes, which can be further divided into two types: martite-microplaty (roughly 5%) and martite-goethite iron ores (about 95%). Over the past decade, martite-microplaty iron ores have been extensively mined, leading to martite-goethite (M-G) becoming the dominant iron ores extracted in Western Australia. Despite their critical importance, much

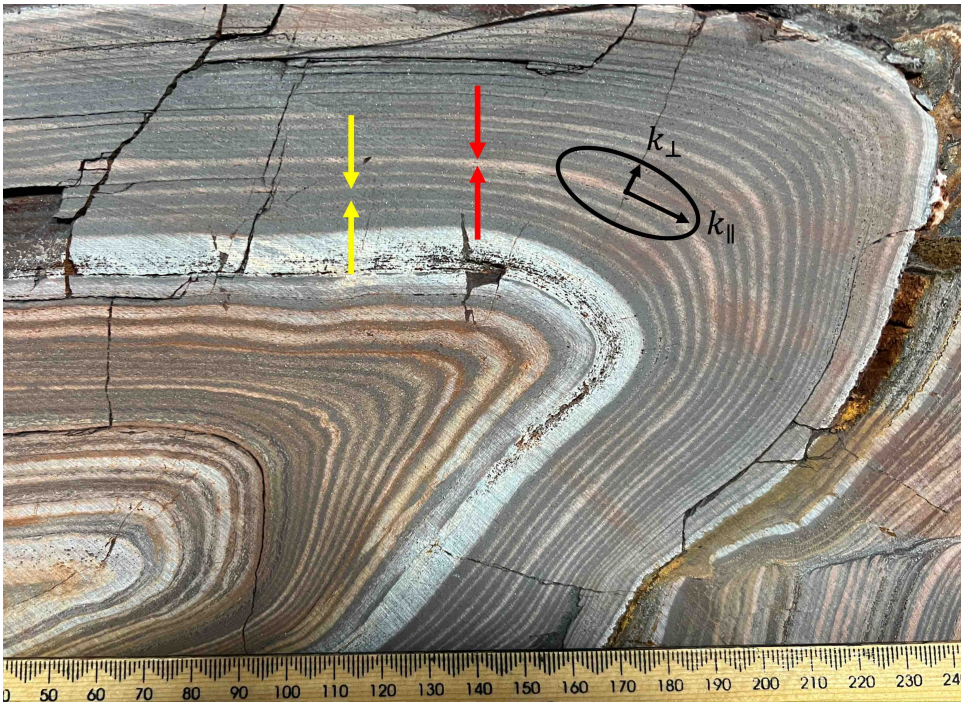


**Figure 1.1:** Detailed image of a banded iron formation (BIF) from Hamersley Basin, Western Australia, highlighting the fine banding and contrasting porosity between darker magnetite and lighter chert/carbonate/silicate bands. The ellipse at the centre sketches the permeability tensor, indicating the longitudinal ($k_\parallel$) and transverse ($k_\perp$) permeability components.

remains to be discovered about these deposits, particularly regarding exploration. Various genetic models have been proposed, yet a consensus on the formation of these deposits is still lacking.

The mineralogy of the host rock, the Banded Iron Formation (BIF), is critical to understanding the mechanisms behind Martite-Goethite (M-G) ore genesis [Morris, 1985; Ramanaidou & Wells, 2014]. BIFs are metasedimentary rocks consisting of alternating layers of magnetite ($Fe_3O_4$) and gangue minerals, including chert, silicates, and carbonates (see Figure 1.1). The formation of M-G ore involves two main processes: supergene lateritic and mimetic enrichment, with the latter further subjected to lateritic weathering [Morris, 1985; Ramanaidou & Wells, 2014]. Most M-G ores in Australia undergo supergene mimetic enrichment within the Banded Iron Formation (BIF). This process involves the replacement of gangue minerals by goethite while retaining the original petrological characteristics of the BIF [Morris, 1980; Ramanaidou & Morris, 2010; Perring, 2021]. Subsequent weathering affects the primary ore; nevertheless, this study focuses on the ore genesis and disregards the subsequent steps.

Various genetic models, such as the electrochemical cell model, seek to explain the M-G ore formation and the mimetic replacement of gangue minerals by goethite [Morris, 1980, 1985; Ramanaidou & Morris, 2010]. These models sparked renewed interest in understanding iron-ore genesis, with researchers suggesting a supergene-modified hypogene-hydrothermal model that involves warm basinal brines and ascending or descending heated meteoric fluids in transforming iron formation into high-grade ore deposits [Barley et al., 1999; Webb et al., 2003; Taylor et al., 2001]. An alternative model by Lascelles [2002, 2016] suggests that certain parts of the Banded Iron Formation (BIF) undergo silica loss during compaction and diagenesis, resulting in chert-free BIF layers. These specific BIF layers then undergo supergene enrichment, leading to the formation of martite-goethite ore. Expanding on this concept, Perring et al. [2020] recently proposed a comprehensive physical process model for martite-goethite (M-G) mineralisation; a model incorporating continuous Cenozoic uplift of the BIF-rich Hamersley Province, the generation of acidic and reducing fluids resulting from interactions between meteoric water and organic matter, and the subsequent leaching of $Fe^{2+}$ from magnetite. This process produces a supergene ore-fluid that descends into the alkaline groundwater, transforming magnetite into martite and replacing gangue minerals with goethite.

Understanding the broad range of physical attributes within the long history of the rocks is a substantial challenge. This complexity arises from the problem's multi-scale and multi-physics features, the interplay of multiple processes, and the superposition of various enrichment events [Morris, 1985; Angerer et al., 2014]. Multiple factors, including the structural layout, stress environment, permeability during the mineralisation period, and several phases of rock-fluid interactions and weathering processes, interact in a complex manner.

Most iron-ore discoveries in Western Australia were made in the 1960s through outcrop mapping. This underscores the crucial role of the Marra Mamba and Brockman Iron Formations as host rocks [Campana, 1966]. Present geological inquiries are shifting towards pinpointing the specific locations of high-grade iron-ore deposits within these formations. The Brockman Syncline BS4 deposit exemplifies this trend [Sommerville et al., 2014], where distinct mineralisation areas are observed within the same formation (see Figure 1.2).

This localisation question calls for a more detailed geological approach, transitioning from the scale of entire formations to more localised studies. Understand-

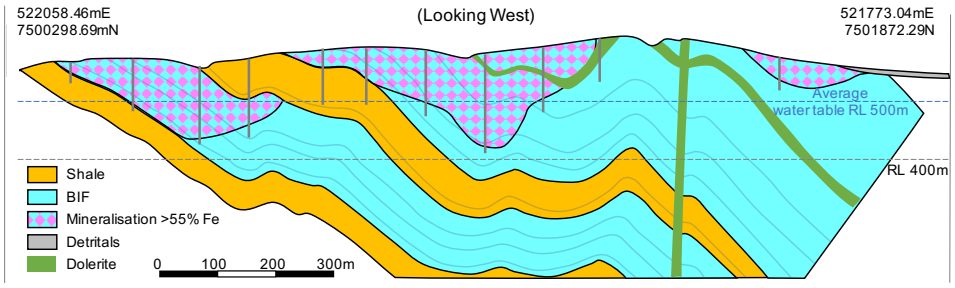


**Figure 1.2:** Simplified version of a typical geological cross-section from the Brockman Syncline BS4 deposit, with drill-hole traces, shown in Sommerville et al. [2014]. Mineralised areas include hydrated and non-hydrated domains.

ing the permeability contrast between formations remains critical, with shales functioning as aquicludes that concentrate fluids [Morris, 1985], as indicated by the mineralised areas in the cross-section (Figure 1.2). Nonetheless, the permeability characteristics within the BIFs themselves also need consideration. The first and most straightforward hypothesis to test is the stratigraphic control of permeability within the BIFs, prioritising the study of the fluid flow path as a preliminary step for mineralisation before delving into any chemical aspects.

### 1.1.2 Numerical approach

Recent decades have seen a surge in research aimed at quantitatively describing subsurface fluid transport in sedimentary basins. This is crucial for developing quantitative models of sediment diagenesis and efficient exploration techniques for mineral deposits [Bethke, 1989]. When combined with observational and experimental study results, quantitative modelling techniques have proven efficient in analysing flow and transport in sedimentary basins across geologic time and length scales. These techniques underscore the control of fluid transport on the formation of certain ore deposits [Tóth, 2016].

The crucial role of groundwater in subsurface transport and mineral accumulation is well established, with paleochannels serving as conduits for the long-distance transit of ore-forming components. However, questions remain about the mechanism of fluid content and migration, source bed locations and extents, the influence of porosity and permeability on concentration patterns, the timing of mineralisation, and the flow rates required for significant ore body deposition [Erőss et al., 2018].

Pioneering work by White [1971] in groundwater-type calculations was crucial

in shaping strata-bound ore genesis modelling , and subsequent studies have further explored the relationship between groundwater flow and ore formation [Ortiz et al., 1980; Garven, 1985; Wood & Hewett, 1984; Baskov, 1987; Garven et al., 1993]. Yet, despite these advancements, the understanding of supergene Martite-Goethite iron-ore enrichment through this lens remains limited.

Groundwater flow theory provides a framework for analysing subsurface permeability distributions and water table configurations as boundary value problems in a continuum model. The key parameter in this theory is the hydraulic permeability tensor, $K$, which encapsulates the local principal directions in a rotated coordinate system aligned with the principal contributions in the longitudinal ($k_{\parallel}$) and transverse ($k_{\perp}$) components of the permeability with respect to the stratigraphic orientation. Darcy's law is fundamental in this context as it defines the specific discharge, $\mathbf{q}$, in terms of the hydraulic conductivity, $K$. The relationship between them is governed by the simplified equation $\nabla \cdot \mathbf{q} = 0$, assuming steady-state conditions and based on the hypothesis of incompressible flow. Consequently, this equation leads to the classical diffusion problem, where $\phi$ is introduced as the hydraulic head, a measure of the total energy per unit weight of water at a specific location in the groundwater system. Groundwater flow direction and magnitude are determined by the gradient of $\phi$, denoted as $\nabla\phi$. The equation for this diffusion problem is expressed as:

$$\nabla \cdot (K \nabla \phi) = 0. \tag{1.1}$$

Groundwater flow theory provides a framework for analysing subsurface permeability distributions and water table configurations as boundary value problems in a continuum model. The key parameter in this theory is the hydraulic permeability tensor, $K$, which encapsulates the local principal directions in a rotated coordinate system aligned with the principal contributions in the longitudinal ($k_{\parallel}$) and transverse ($k_{\perp}$) components of the permeability with respect to the stratigraphic orientation. Darcy's law is fundamental in this context as it defines the specific discharge, $\mathbf{q}$, in terms of the hydraulic conductivity, $K$. The relationship between them is governed by the simplified equation $\nabla \cdot \mathbf{q} = 0$, assuming steady-state conditions and based on the hypothesis of incompressible flow. Consequently, this equation leads to the classical diffusion problem, where $\phi$ is introduced as the hydraulic head, a measure of the total energy per unit weight of water at a specific location in the groundwater system. Groundwater

flow direction and magnitude are determined by the gradient of $\phi$, denoted as $\nabla\phi$. The equation for this diffusion problem is expressed as:

Given a near-constant water table, the timescale for ore production is on par with the time frame over which steady-state theory models regional fluid flow in large sedimentary basins. Accounting for the potential heterogeneity and anisotropy in hydraulic conductivity and spatial variation in porosity, solute transport within this groundwater system can be described by the unsteady linear advection-diffusion-reaction equation:

$$\frac{\partial C}{\partial t} = \nabla \cdot (\mathbf{D}\nabla C) - \nabla \cdot (\mathbf{q}C) + \mu C, \tag{1.2}$$

where $C$ denotes an inert solute concentration, $\mu$ is the medium response rate per fluid volume, and $\mathbf{D}$ represents the dispersion tensor.

Although this model problem is simple and has been widely studied during the last few decades, obtaining reliable simulation results is still challenging for traditional numerical methods. Standard discretisations, such as the finite element method (FEM), suffer from unphysical oscillations for advection-dominated regimes if the mesh's resolution is insufficient. Specifically, there are two issues for the proposed model in an advection-dominated regime: first, a limit case when the equation becomes advection-dominated, showing sharp internal or boundary layers (1.1) and, second, the highly anisotropic and heterogeneous diffusion problem (1.2).

Brooks & Hughes [1982] introduced the SUPG method to overcome these difficulties. This method adds a residual-based stabilising term to induce a numerical diffusion along the streamlines. This enhances control and stability in the convective operator while conserving consistency in the formulation. The Galerkin/least-squares method (GLS) [Hughes et al., 1989] generalises this idea, using a least-squares formulation into the stabilisation term to enhance control of the whole residual. Although these methods have proven effective at stabilising the numerical solution of convection-dominated problems, the accuracy of these approaches highly depends on a user-stabilised parameter, which turns challenging to tune for most real-world problems.

Hughes [1995] unified these ideas in the variational multiscale method (VMS). This method captures the sub-scales in the variational form and improves stability properties while maintaining the consistency of the former residual-based methods

[Hughes et al., 1998, 2000; Bazilevs et al., 2007, 2010; Chang et al., 2012; Ghaffari Motlagh et al., 2013; Garikipati & Hughes, 2000]. The main idea of VMS is to decompose the solution into two different scales and keep the coupled influence among them, approximating the effect of the fine scale that a given mesh cannot capture. The VMS paradigm led to a reinterpretation of the traditional residual-based methods as approximate sub-grid scale models and identified the unresolved fine scales as an essential key in the stabilisation, even for linear systems including the advection-diffusion equation [Hughes, 1995; Masud & Khurram, 2004].

Cohen et al. [2012] extended the stabilisation ideas with least-squares/minimum residual minimisation in GLS to encompass general dual norms. They introduced a saddle point formulation of this residual method, which refers to a VMS formulation. These ideas were extended in the Discontinuous Petrov-Galerkin method (DPG) [Demkowicz & Gopalakrishnan, 2010, 2011; Demwkowicz & Gopalakrishnan, 2011] using different non-standard dual norms for stabilisation [Zitelli et al., 2011; Niemi et al., 2013a, 2011, 2013b; Calo et al., 2014]. DPG is introduced in the context of a VMS for the convection-diffusion equation in Chan & Evans [2013], offering an alternative, well-behaved sub-grid model to approximate the fine scale. Extensions to these ideas regarding parabolic problems include studies by Cockburn & Shu [1998]; Borker et al. [2017]; Rivière [2008]; Di Pietro & Ern [2011] for dG and Demkowicz & Gopalakrishnan [2010]; Demwkowicz & Gopalakrishnan [2011]; Führer et al. [2021]; Roberts & Henneking [2020] for DPG methods.

Although these methods show stability for advection-dominated problems, the lack of a priori localisation of the inner or boundary layers in the exact solution leads to expensive simulations on quasi-uniform meshes. Additionally, the lack of robust refinement strategies limits their use in unsteady problems where the solution varies in space and time. Here, this computational cost is reduced using adaptive methods that rely on a posteriori error estimators to refine solution singularities. A posteriori error estimators for unsteady advection-diffusion-reaction problems are described in studies by Ern & Vohralík [2010]; Zhu & Schötzau [2010] and for unsteady dG implementations in publications by Ern & Proft [2005]; Araya & Venegas [2014]; Cangiani et al. [2014].

The Discontinuous Galerkin Method (dG), initially proposed by Reed & Hill [1973], has offered an alternative stabilisation technique over the last few decades and was rapidly extended in numerous applications due to its good stability prop-

erties [Arnold et al., 2001; Ayuso & Marini, 2009; Cockburn et al., 2012; Di Pietro & Ern, 2011]. dG is advantageous over classical methods in providing robustness and high-order accurate approximations, especially for advective operators associated with hyperbolic equations [Johnson & Pitkäranta, 1986]. Its stability is induced by the numerical fluxes imposed on internal element interfaces, leading to discretely stable solutions with local conservation. dG is related to residual-based stabilisation methods in Johnson & Pitkäranta [1986]; Brezzi et al. [2006] and is used for new stabilised methods based on VMS, including the Multiscale Discontinuous Galerkin method (MSDG) [Bochev et al., 2005; Buffa et al., 2006; Hughes et al., 2006], the Discontinuous residual-free bubble method [Sangalli, 2004], among other recent approaches [Coley & Evans, 2018; Stoter et al., 2022].

Alternative stabilisation techniques that generalise dG ideas are the Interior Penalty methods that use continuous functions and can handle difficulties encountered by continuous finite element methods in advection-diffusion problems [Babuška & Zlámal, 1973; Douglas & Dupont, 1976]. These methods penalise flux jumps at mesh interfaces and were applied to biharmonic operators and second-order elliptic and parabolic problems [Douglas & Dupont, 1976]. Burman and collaborators have advanced the error estimates for interior penalty methods [Burman & Hansbo, 2004; Burman & Zunino, 2006] and generalised the ideas to introduce the high-order Continuous Interior Penalty (CIP) finite element method [Burman & Ern, 2007, 2005]. Effectively, Burman [2009] introduced a formulation relating stabilised continuous and discontinuous Galerkin frameworks with the CIP formulation.

Calo et al. [2020b] introduced a new class of adaptive stabilised conforming finite elements via residual minimisation for steady problems. The method combines residual minimisation ideas with the stability of the discontinuous Galerkin formulations. As a result, the method delivers a stable continuous solution and a robust error representation to perform on-the-fly adaptivity. The authors introduce the framework in a series of papers for linear and nonlinear applications (e.g., advection-diffusion problems with heterogeneous and highly anisotropic diffusion [Cier et al., 2021b], its use combined with isogeometric analysis [Calo et al., 2021], nonlinear weak constraint enforcement [Cier et al., 2021b], goal-oriented adaptivity [Rojas et al., 2021], for incompressible flows [Kyburg et al., 2022; Łoś, et al., 2021], and dynamic fracture propagation [Labanda et al., 2022]).

In this document, we present a novel alternative method to overcome the

advection-dominated regime and the highly anisotropic and heterogeneous diffusion presented in the transport phenomena based on groundwater theory, interpreting these ideas for a conforming finite element method via residual minimisation on dual norms [Calo et al., 2020a] via the VMS formalism. The method builds on the concepts from MSDG to decompose a full-discrete discontinuous finite element space into discontinuous (fine) and continuous (coarse) components and leverages VMS analysis to define an inter-scale operator. The strategy begins with an arbitrary discontinuous finite element space and derives a continuous representation by minimising the residual on a dual discontinuous Galerkin norm. Using the VMS analysis and the residual representative obtained from the dual Galerkin orthogonality, we derive an inter-scale problem to define the stable fine-scale contribution and an error estimator to guide adaptivity. This approach results in a stable coarse- and fine-scale solution derived from a symmetric saddle-point formulation that delivers a robust a-posteriori error indicator.

## 1.2 Thesis overview

This work aims to develop a novel numerical framework for understanding the geological processes behind localised iron-ore deposits. It focuses on solving the groundwater flow problem to illustrate that supergene M-G iron-ore enrichment can be modelled as a non-reactive transport issue controlled by formation structure and stratigraphy. As a result of these explorations, this project aims to enhance prospecting techniques by innovatively integrating a physics-based approach with geophysical data sets, thereby providing a comprehensive understanding of the formation of these deposits.

## 1.3 Motivation and Objectives

This project seeks to build a computational model to describe the bedded iron-ore mineralisation process and it encompasses three main components:

1. The construction of a theoretical model to interpret the genesis of iron-ore in banded iron formations. This model simplifies a complex and poorly understood geochemical problem into a more manageable non-reactive flow simulation, incorporates the permeability anisotropy following the strata orientation, and improves current theories in iron-ore formation studies.

2. The development of a computational framework for both steady and unsteady problems, grounded in a variational multiscale approach.

3. The analysis of the genetic model through numerical experiments and the validation of the proposed numerical framework using well-documented case studies from industrial literature.

## Significance

This research is a significant undertaking that may benefit the mining and steel industries, thereby providing an advantage to the Australian economy. The existing models for predicting mineral formation are somewhat imprecise and often fail to align with geological observations. This project seeks to supply these industries with precise predictions concerning the location of mineral deposits; thus, mitigating the financial burden of exploration and the associated environmental impacts.

Consequently, our model will assist in predicting the iron mineralisation process and pinpointing the location of iron-ore deposits using geological information. Further work may allow the model to yield precise prospecting maps displaying anticipated iron-ore formations. These simulation results will reduce the costs associated with mineral exploration and a decrease in environmental damage, and refine the process of target drilling.

Furthermore, the approach used in this project can also be applied to other supergene mineralisation processes. This includes important mineral deposits such as supergene copper [Kidder et al., 2020; Kahou et al., 2021], lead [Sergeev et al., 2017], and zinc [Boni & Mondillo, 2015]. Each of these minerals has large economic effects, not just in terms of their direct value, but also in supporting a range of industries, demonstrating the wider significance of this project's methodology.

Moreover, the introduced numerical framework is notably adaptable and could be extended to tackle other physical challenges fraught with numerical instabilities. This simulator will improve various simulation fields, such as fluid mechanics, heat transfer, and structural analysis.

As such, the simulator's promise is not confined to the mining and steel industry alone. It signifies potential advancements in multiple other sectors, contributing widely to various scientific disciplines.

## 1.4 Structure of the thesis

This document is divided into two main parts. The first part (ch. 2&3 ) focuses on developing a numerical framework based on a variational multiscale approach, while the second part (see Chapter 4) applies this framework to the specific issue of iron-ore mineralisation. **Chapter 2** outlines the numerical framework utilised in this research, rooted in a variational multiscale approach. This framework is designed to tackle convection-dominated diffusion equations—an important aspect of this research due to the pronounced anisotropy and heterogeneity of the diffusion tensor. In **Chapter 3**, the numerical approach is extended to unsteady problems using the methods of lines. This chapter evaluates the reliability and efficiency of the approach by testing it with challenging problems. **Chapter 4** introduces a genetic model that explains the mechanisms behind the formation of BIF supergene MG iron-ore deposits. The model is tested against well-known deposits from the literature. Finally, **Chapter 5** concludes the document with a summary of the research and suggestions for future work.

# Chapter 2

# Numerical framework for steady convection-diffusion-reaction problems

This chapter introduces a numerical framework for simulating convection-dominated diffusion problems, including highly anisotropic and heterogeneous diffusion tensor as an important feature for this research. [1] We interpret the stabilised finite element method via residual minimisation in Calo et al. [2020a] as a variational multiscale method. We approximate the solution of partial differential equations using two discrete spaces that we build on a triangulation of the domain; we denote these spaces as coarse and enriched. Building on the adaptive stabilised FEM approach in Calo et al. [2020a], we find a coarse-scale approximation in a continuous space by minimising the residual on a dual discontinuous Galerkin norm; this process allows us to compute a robust error estimate to construct an on-the-fly adaptive method. We reinterpret the residual projection using the variational multiscale framework to derive a fine-scale approximation. So, on each mesh of the adaptive process, we get stable coarse- and fine-scale solutions from a symmetric saddle-point formulation and an a-posteriori error indicator to guide automatic adaptivity. Moreover, we introduce a heuristic dual-term contribution in the variational form to improve the full-scale approximation for symmetric formulations (e.g., diffusion problem). In the following sections, we

[1] The content of this chapter is published in: Giraldo & Calo [2023]. A variational multiscale method derived from an adaptive stabilized conforming finite element method via residual minimization on dual norms. *Computer Methods in Applied Mechanics and Engineering (CMAME),2023.*

test our framework in several challenging scenarios for linear diffusion problems to demonstrate the framework's performance in providing stability in the solution with optimal convergence rates in the asymptotic regime and robust performance in the pre-asymptotic regime.

## 2.1 Continuous problem and its discretisation

### 2.1.1 Convection-diffusion-reaction equation

Let $\Omega \in \mathbb{R}^d$, with $d = 2, 3$ be an open, bounded Lipschitz polygon with boundary $\Gamma := \partial\Omega$. Let $\kappa \in [L^\infty(\Omega)]^{d,d}$ represent a positive definite diffusion tensor, $\beta \in [L^\infty(\Omega)]^d$ a smooth, divergence-free velocity field (i.e., $\nabla \cdot \beta = 0$), and $\mu \in L^\infty$ the reaction coefficient. For a given open and bounded domain $K$, we represent its $L^2$ inner product and $L^2$ norm as $(\cdot,\cdot)_{0,K}$ and $||\cdot||_{0,K}$, respectively. We set $(\cdot,\cdot)_0 := (\cdot,\cdot)_{0,\Omega}$ and $||\cdot||_0 := ||\cdot||_{0,\Omega}$ for convenience. We define the well-known Hilbert space $H^1(\Omega) := \{v \in L^2(\Omega) : \nabla v \in L^2(\Omega)\}$ with the inner product on $\Omega$ denoted by $(\cdot,\cdot)_1$. We define the inflow and outflow boundaries, respectively, by

$$\Gamma^- := \{x \in \Gamma \mid \beta \cdot \mathbf{n} < 0\}, \qquad \Gamma^+ := \{x \in \Gamma \mid \beta \cdot \mathbf{n} \geq 0\}.$$

We denote by $\Gamma_D$ the Dirichlet and $\Gamma_N$ the Neumann boundary functions, which are a complementary subset of $\Gamma$ (i.e., $\Gamma = \overline{\Gamma_N} \cup \overline{\Gamma_D}$). Thus, we define the inflow and outflow parts of the Neumann boundary as follows:

$$\Gamma_N^- := \Gamma_N \cap \Gamma^-, \qquad \Gamma_N^+ := \Gamma_N \cap \Gamma^+. \tag{2.1}$$

We consider the advection-diffusion-reaction equation in strong form as follows:

$$\begin{aligned} -\mathrm{div}\,(\kappa\nabla u) + \beta \cdot \nabla u + \mu u &= f && \text{in } \Omega, \\ u &= u_D && \text{on } \Gamma_D, \\ (-\beta u + \kappa\nabla u) \cdot \mathbf{n} &= h_N && \text{on } \Gamma_N^-, \\ \kappa\nabla u \cdot \mathbf{n} &= h_N && \text{on } \Gamma_N^+, \end{aligned} \tag{2.2}$$

where $f \in L_2(\Omega)$ is the source term, and $u_D \in H^{1/2}(\Gamma_D)$ and $h_N \in H^{-1/2}(\Gamma_N)$ are the Dirichlet and Neumann boundary conditions, respectively.

### 2.1.2 Discontinuous Galerkin (dG) discretisation

Let $\mathfrak{T}$ be a triangulation that decomposes $\Omega$ into $n$ subdomains $K$, denoted as $\mathfrak{T} := K_{i i=1}^{n}$. Here, the broken space of discontinuous functions is

$$\mathbb{V}_h := \{v \in L_2(\mathfrak{T}) : v|_K \in \mathbb{P}^p(K), \forall K \in \mathfrak{T}\}, \tag{2.3}$$

where $\mathbb{P}^p$ is the set of functions of degree $p$ or less. Let $K_1$ and $K_2$ represent two separate elements in $\mathfrak{T}$ sharing a common face $F$. The entire set of such faces is defined as $\mathscr{S}_h := \bigcup_{K\in\mathfrak{T}} F$. We denote the collection of interior faces by $\mathscr{S}_h^0 = \mathscr{S}_h \backslash \Gamma$ and boundary faces by $\mathscr{S}_h^\partial = \mathscr{S}_h \cap \Gamma$. Furthermore, we define inflow boundary faces as $\mathscr{S}_h^{\partial^-} := \mathscr{S}_h^\partial \cap \Gamma^-$ and outflow boundary faces as $\mathscr{S}_h^{\partial^+} := \mathscr{S}_h^\partial \cap \Gamma^+$. Lastly, $\mathscr{S}_h^D = \mathscr{S}_h \cap \Gamma^D$ and $\mathscr{S}_h^N = \mathscr{S}_h \cap \Gamma^N$ are defined as the sets of Dirichlet and Neumann faces, respectively. Let $h_K$ be the diameter of the element and $h_F$ be the diameter of the face. For the face $F$, we define $\mathbf{n}_F$ as the unit normal vector directed from $K_1$ to $K_2$, as illustrated in Figure 2.1. Furthermore, the vectors $\mathbf{n}_{F,1}$ and $\mathbf{n}_{F,2}$ represent the unit normals on the face $F$, pointing outwards from $K_1$ and $K_2$, respectively. It follows from the definitions that $\mathbf{n}_{F,1} = -\mathbf{n}_{F,2}$ and $\mathbf{n}_{F,1} = \mathbf{n}_F$. Given a scalar field $v$ and denoting $v_{1,2} := v|_{K_1,K_2}$, we define the arithmetic average $\{v\}$, weighted average $\{v\}_\omega$ and jump $[\![v]\!]$ on an internal face $F \in \mathscr{S}_h^0$ by

$$\{v\} := \frac{1}{2}(v_1 + v_2), \qquad \{v\}_\omega := v_1\omega_1 + v_2\omega_2, \qquad [\![v]\!] := v_1\mathbf{n}_{F,1} + v_2\mathbf{n}_{F,2}$$

whit weights $\omega_1$ and $\omega_2$ that satisfy $\omega_1 + \omega_2 = 1$ and $\omega_1, \omega_2 \geq 0$.
For heterogeneous diffusion we use:

$$\omega_1 = \frac{\delta_1}{\delta_1 + \delta_2}, \qquad \omega_2 = \frac{\delta_2}{\delta_1 + \delta_2}, \tag{2.4}$$

with $\delta_1 = \mathbf{n}_F \cdot \kappa_1 \mathbf{n}_F$ and $\delta_2 = \mathbf{n}_F \cdot \kappa_2 \mathbf{n}$. In the homogeneous diffusion case, these weights reduce to $\omega_1 = \omega_2 = \frac{1}{2}$, recovering the arithmetic average. We set on boundary faces $F \in \mathscr{S}_h^\partial$ that $\{v\} = \{v\}_\omega = v$ and $[\![v]\!] = v\mathbf{n}_F$. For further details in the discrete setting, see Ern et al. [2009].

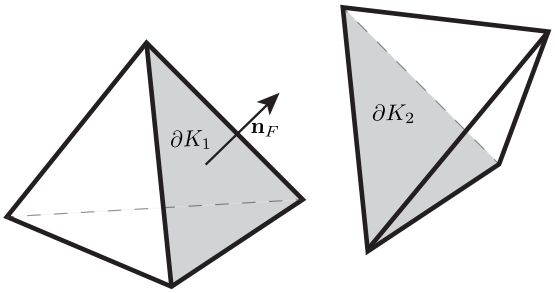


**Figure 2.1:** Notation of the element interface.

We use the following dG discrete form:

$$\begin{cases} \text{Find } u_h \in \mathbb{V}_h, \text{such that:} \\ b_h(v_h, u_h) = \ell_h(v_h) \quad \forall\, v_h \in \mathbb{V}_h, \end{cases} \tag{2.5}$$

where $b_h$ defines the dG discrete bilinear form considering the contribution of the diffusive part from the Symmetric Weighted Interior Penalty form (SWIP) and the advective part from the upwinding formulation:

$$b_h(v,u) := b_h(v,u)^{\text{swip}} + b_h(v,u)^{\text{upw}}, \tag{2.6}$$

with,

$$\begin{aligned} b_h(v,u)^{\text{swip}} := & \sum_{K\in\mathfrak{T}} (\nabla v, \kappa\,\nabla u)_K \\ & - \sum_{F\in\mathscr{S}_h^0} \Big( (\llbracket v \rrbracket\,,\, \{\kappa\nabla u\}_\omega \cdot \mathbf{n}_F)_F + (\{\kappa\nabla v\}_\omega \cdot \mathbf{n}_F\,,\, \llbracket u \rrbracket)_F - n_e\gamma_\kappa(\llbracket v \rrbracket, \llbracket u \rrbracket)_F \Big) \\ & - \sum_{F\in\mathscr{S}_h^D} \Big( (v,\, \kappa\nabla u \cdot \mathbf{n}_F)_F + (\kappa\nabla v \cdot \mathbf{n}_F\,,\, u)_F - n_e\gamma_\kappa(v,u)_F \Big), \end{aligned} \tag{2.7}$$

$$\begin{aligned} b_h(v,u)^{\text{upw}} := & \sum_{K\in\mathfrak{T}} (v, \beta\cdot\nabla u)_K + \sum_{K\in\mathfrak{T}} (v, \mu u)_K + \sum_{F\in\mathscr{S}_h^{\partial-}} (v, (\beta\cdot\mathbf{n}_F)\, u)_F \\ & + \sum_{F\in\mathscr{S}_h^0} \Big( \big(\llbracket v \rrbracket, \tfrac{n_a}{2}|\beta\cdot\mathbf{n}_F|\llbracket u \rrbracket\big)_F - (\{v\}, (\beta\cdot\mathbf{n}_F)\llbracket u \rrbracket)_F \Big), \end{aligned} \tag{2.8}$$

where $(\cdot,\cdot)_F$ and $(\cdot,\cdot)_K$ represent the inner product over the discrete face and internal element, respectively. The diffusion penalty $\gamma_\kappa$ is defined for all internal faces $F \in \mathscr{S}_h^0$ as

$$\gamma_\kappa := \frac{2\kappa_1\kappa_2}{\kappa_1+\kappa_2},$$

and $n_e$ and $n_a$ are two positive penalty coefficients for the diffusion and advection bilinear forms. We define $n_e$ as [Shahbazi, 2005]:

$$n_e := \frac{(p+1)(p+d)}{d} \begin{cases} \frac{1}{2}\left(\frac{\mathcal{A}(\partial K_1)}{\mathcal{V}(K_1)} + \frac{\mathcal{A}(\partial K_2)}{\mathcal{V}(K_2)}\right) & \text{if} \quad F = \partial K_1 \cap \partial K_2, \\ \frac{\mathcal{A}(\partial K)}{\mathcal{V}(K)}, & \text{if} \quad F = \partial K \cap \Gamma, \end{cases} \tag{2.9}$$

where $d$ denotes the problem dimension, and $p$ represents the polynomial degree of the test space. In both 3D and 2D, $\mathcal{V}$ and $\mathcal{A}$ represent the volume and area (or length in 2D) of an element, respectively. The parameter $n_a$ adjusts the numerical flux associated with the upwinding bilinear form. Centered fluxes correspond to $n_a \to 0$ while upwind fluxes are associated with $n_a \to 1$. As the scenarios we explore in this work are primarily advective dominant, we set $n_a = 1$; However, this parameter can be adjustable, as seen in traditional dG methods. The right-hand side in (2.5) accounts for weakly imposed non-homogeneous Dirichlet and Neumann boundary conditions as:

$$\begin{aligned} \ell_h(v) := \sum_{K\in\mathfrak{T}} (v, f) + \sum_{F\in\mathscr{S}_h^D} (n_e\gamma_\kappa (v, u_D)_F - (\kappa\nabla v\cdot\mathbf{n}_F, u_D)_F) \\ - \sum_{F\in\mathscr{S}_h^D\cap\Gamma^-} (v, (\beta\cdot\mathbf{n}_F)\, u_D)_F + \sum_{F\in\mathscr{S}_h^N} (v, u_N)_F. \end{aligned} \tag{2.10}$$

We endow $\mathbb{V}_h$ with the norm:

$$\|w\|^2_{\mathbb{V}_h} := \|w\|^2_{\text{upw}} + \|w\|^2_{\text{swip}}, \tag{2.11}$$

with

$$\|w\|^2_{\text{upw}} := \|w\|^2_0 + \sum_{F\in\mathscr{S}_h} \left(\tfrac{1}{2}|\,\beta\cdot\mathbf{n}_F|\,[\![w]\!],[\![w]\!]\right)_{0,F} + \sum_{K\in\mathfrak{T}} \beta_c^{-1} h_K \|\,\beta\cdot\nabla w\,\|^2_{0,K}, \tag{2.12}$$

$$\|w\|^2_{\text{swip}} := \|\,\kappa\nabla w\,\|^2_0 + \sum_{F\in\mathscr{S}_h} (n_e\gamma_\kappa [\![w]\!],[\![w]\!])_{0,F}\,, \tag{2.13}$$

where $\|\cdot\|_0$ represents the $L_2$-norm on the domain $\Omega$ and $\|\cdot\|_{0,\Gamma}$ on its boundary $\Gamma$, whilst $\|\cdot\|_{0,K}$ and $\|\cdot\|_{0,F}$ denote the $L_2$-norm on the element $K$ and faces $F$, respectively. Additionally, we define $\beta_c$ as a reference velocity given by $\beta_c := \|\beta\|_\infty$.

Problem (2.5) is well-posed, and the inf-sup stability is established through the norm (2.11). Refer to Ayuso & Marini [2009] for further details. The sub-index h for the test and trial solutions (i.e., $u_h$ and $v_h$) are dropped in the following sections to keep the notation simple.

## 2.2 Residual minimisation formulation

Building upon the work of Calo et al. [2020b], we briefly recap the residual minimisation strategy that forms the basis of this formulation. The main idea is to deliver a stable approximation in a continuous space by minimising the residual onto a discontinuous Galerkin norm. First, we define $\bar{\mathbb{V}}_h$ as the $H^1$-conforming subspace (i.e., $\bar{\mathbb{V}}_h = \mathbb{V}_h \cap H^1$). Then, from the stable formulation in (2.5), we use the trial subspace $\bar{\mathbb{V}}_h$ to solve the following minimisation problem:

$$\begin{cases} \text{Find } \bar{u} \in \bar{\mathbb{V}}_h \subset \mathbb{V}_h, \text{such that:} \\ \bar{u} = \underset{z \in \bar{\mathbb{V}}_h}{\arg\min} \dfrac{1}{2} \| \ell_h - B_h\, z \|^2_{\mathbb{V}_h^*}, \end{cases} \tag{2.14}$$

where the operator $B_h$ is defined by $\langle \cdot, B_h w \rangle_{\mathbb{V}_h \times \mathbb{V}_h^*} := b_h(\cdot, w), \forall w \in \mathbb{V}_h$. We state (2.14) as a critical point of the minimising functional, which can be translated into the following linear problem:

$$\begin{cases} \text{Find } \bar{u} \in \bar{\mathbb{V}}_h, \text{such that:} \\ (B_h \delta u, \ell_h - B_h \bar{u})_{\mathbb{V}_h^*} = g(R_{\mathbb{V}_h}^{-1} B_h \delta u, R_{\mathbb{V}_h}^{-1}(\ell_h - B_h \bar{u})) = 0 \quad \forall \delta u \in \bar{\mathbb{V}}_h, \end{cases} \tag{2.15}$$

where $g(\cdot, \cdot)$ represents the inner product that induces the discrete norm $\| \cdot \|_{\mathbb{V}_h}$ and $R_{\mathbb{V}_h}$ denotes the Riesz operator which maps the elements in $\mathbb{V}_h$ to the dual space $\mathbb{V}_h^*$, such that:

$$\langle \cdot, R_{\mathbb{V}_h} y \rangle_{\mathbb{V}_h \times \mathbb{V}_h^*} := g(\cdot, y). \tag{2.16}$$

Let the residual representative be

$$\varepsilon := R_{\mathbb{V}_h}^{-1}(\ell_h - B_h \bar{u}) \in \mathbb{V}_h,$$

which implies

$$g(\varepsilon, v) = \ell_h(v) - b_h(\bar{u}, v), \quad \forall v \in \mathbb{V}_h;$$

thus, the residual minimisation problem in (2.14) leads to a saddle point problem:

$$\begin{cases} \text{Find } (\varepsilon, \bar{u}) \in \mathbb{V}_h \times \bar{\mathbb{V}}_h, \text{ such that:} \\ g(v,\varepsilon) + b_h(v,\bar{u}) + b_h(\varepsilon,\bar{w}) \;\; = \;\; \ell_h(v), \qquad \forall (v,\bar{w}) \in \mathbb{V}_h \times \bar{\mathbb{V}}_h, \end{cases} \tag{2.17}$$

where the orthogonality condition between the residual representation and the $H^1-$conforming subspace of $\mathbb{V}_h$ is enforced as $b_h(\varepsilon,\bar{w}) = 0$. Features of the methodology and the properties of the error estimator and continuous solution are discussed in detail in Calo et al. [2020b]; Cier et al. [2021b]; Rojas et al. [2021] in the context of advection-reaction-diffusion equations.

## 2.3 A variational multiscale interpretation of the residual minimisation framework

### 2.3.1 A multiscale partition of the trial and test spaces

Following the variational multiscale arguments, we decompose $\mathbb{V}_h$ into coarse and fine scales. Since we use a Petrov-Galerkin formalism, our test and trial spaces are different. Thus, starting from the $H^1-$conforming solution space $\bar{\mathbb{V}}_h$, we define appropriate direct-sum partitions of the entire function space $\mathbb{V}_h$ using the operators from the residual minimisation framework. First, we define the space $\mathbb{V}'_h$, as the annihilator of the bilinear form $b_h(\cdot,\bar{w})\ \forall \bar{w} \in \bar{\mathbb{V}}_h$ (e.g., the residual representative belongs to this set of linear functionals that map the operator's range to zero). Thus, given $\bar{\mathbb{V}}_h \subset \mathbb{V}_h$, we define $\mathbb{V}'_h$ as the annihilator of the bilinear form $b_h$ acting on $\mathbb{V}_h$, such that

$$\mathbb{V}'_h := \{v \in \mathbb{V}_h \mid b_h(v,\bar{w}) = 0, \qquad \forall\, \bar{w} \in \bar{\mathbb{V}}_h\}, \tag{2.18}$$

Next, we define $\hat{\mathbb{V}}_h$ as the orthogonal complement of $\mathbb{V}'_h$ with respect to the inner product $g(\cdot,\cdot)$, that is:

$$\hat{\mathbb{V}}_h := \{v \in \mathbb{V}_h \mid g(v,v') = 0, \qquad \forall\, v' \in \mathbb{V}'_h\}. \tag{2.19}$$

Last, we define the complement of the coarse-scale solution space as the kernel of the bilinear $b_h$ when tested by $\hat{\mathbb{V}}_h$. Thus, given $\hat{\mathbb{V}}_h \subset \mathbb{V}_h$, we define $\tilde{\mathbb{V}}_h$ to be

$$\tilde{\mathbb{V}}_h := \{u \in \mathbb{V}_h \mid b_h(\hat{v}, u) = 0, \qquad \forall\, \hat{v} \in \hat{\mathbb{V}}_h\}, \tag{2.20}$$

where the (full-scale) trial space is $\mathbb{V}_h := \bar{\mathbb{V}}_h \oplus \tilde{\mathbb{V}}_h$ and the (full-scale) test space is $\mathbb{V}_h := \hat{\mathbb{V}}_h \oplus \mathbb{V}'_h$. We have a direct sum decomposition of the trial space to deliver a solution $u \in \mathbb{V}_h$ in (2.5), such that:

$$u = \bar{u} + \tilde{u}, \tag{2.21}$$

where we denote $\bar{u} \in \bar{\mathbb{V}}_h$ and $\tilde{u} \in \tilde{\mathbb{V}}_h$ as the coarse- and fine-scale trial functions. Similarly, for any test function $v \in \mathbb{V}_h$, we can write

$$v = \hat{v} + v', \tag{2.22}$$

where we denote $\hat{v} \in \hat{\mathbb{V}}_h$ and $v' \in \mathbb{V}'_h$ as the coarse- and fine-scale test functions. Thus, we have two complimentary direct sum decompositions of $\mathbb{V}_h$.
Let $\varepsilon \equiv \varepsilon' \in V'_h$ be noted. Therefore, we can reformulate the saddle point problem in equation (2.17) as:

$$\begin{cases} \text{Find } (\varepsilon', \bar{u}) \in (\mathbb{V}'_h \times \bar{\mathbb{V}}_h), \text{such that:} \\ g(v, \varepsilon') + b_h(v, \bar{u}) = \ell_h(v), \quad \forall v \in \mathbb{V}_h. \end{cases} \tag{2.23}$$

Splitting the test function using (2.22), we reformulate problem (2.23) as two complementary but independent problems for the coarse-scale solution and the fine-scale residual representative:

- Residual reconstruction (fine-scale problem):

$$\begin{cases} \text{Find } \varepsilon' \in \mathbb{V}'_h, \text{such that} \\ g(v', \varepsilon') = \ell_h(v'), \qquad \forall v' \in \mathbb{V}'_h. \end{cases} \tag{2.24}$$

- $H^1-$conforming solution (coarse-scale problem):

$$\begin{cases} \text{Find } \bar{u} \in \bar{\mathbb{V}}_h, \text{such that} \\ b_h(\hat{v}, \bar{u}) = \ell_h(\hat{v}), \qquad \forall \hat{v} \in \hat{\mathbb{V}}_h, \end{cases} \tag{2.25}$$

which corresponds to a Petrov–Galerkin method with optimal test functions [Demkowicz & Gopalakrishnan, 2011; Zitelli et al., 2011; Niemi et al., 2013a; Calo et al., 2014].

From the definitions of the complementary direct sum decompositions (2.18)-(2.20), we have that $b_h(\hat{v}, \tilde{u}) = b_h(v', \bar{u}) = 0$; thus, problem (2.5) can be split into the following two problems:

$$\begin{cases} \text{Find } (\bar{u}, \tilde{u}) \in \bar{\mathbb{V}}_h \times \tilde{\mathbb{V}}_h, \text{ such that:} \\ b_h(\hat{v}, u) := b_h(\hat{v}, \bar{u}) = \ell_h(\hat{v}), \qquad \forall \hat{v} \in \hat{\mathbb{V}}_h, \\ b_h(v', u) := b_h(v', \tilde{u}) = \ell_h(v'), \qquad \forall v' \in \mathbb{V}'_h. \end{cases} \tag{2.26}$$

Consequently, from (2.24) and $(2.26)_2$, we can rewrite the fine-scale component of the discrete solution in terms of the residual error estimate

$$b_h(v', \tilde{u}) = \ell_h(v') = g(v', \varepsilon'), \qquad \forall v' \in \mathbb{V}'_h. \tag{2.27}$$

Thus, $(2.26)_2$ states that the fine-scale solution satisfies the following problem:

$$\begin{cases} \text{Find } \tilde{u} \in \tilde{\mathbb{V}}_h, \text{ such that:} \\ b_h(v', \tilde{u}) = g(v', \varepsilon'), \quad \forall v' \in \mathbb{V}'_h. \end{cases} \tag{2.28}$$

Lastly, since $b(\hat{v}, \tilde{u}) = g(\hat{v}, \varepsilon') = 0$, the fine-scale problem is equivalent to:

$$\begin{cases} \text{Find } \tilde{u} \in \mathbb{V}_h, \text{ such that:} \\ b_h(v, \tilde{u}) = g(v, \varepsilon'), \quad \forall v \in \mathbb{V}_h. \end{cases} \tag{2.29}$$

**Remark 1** (Relation between VMS reconstruction & dG solution)**.** *By construction, the partitioned full-scale approximation in* (2.21) *is identical to the classical dG solution. Next, we introduce an adjoint multiscale reconstruction; thus, we denote by* $\theta$ *the dG solution of* (2.5)*.*

### 2.3.2 Adjoint multiscale reconstruction

Using the direct sum partitions of the test and trial spaces, we exploit the insight behind the adjoint residual-based estimator proposed for goal-oriented adaptivity in Rojas et al. [2021]; therein, the authors obtained a residual representative for the quantity of interest by solving a well-posed ad hoc discrete problem. In the

present context, this adjoint residual problem is driven by $\varepsilon'$. We introduce the adjoint reconstruction by revisiting the multiscale partitions from the previous section. Given $\varepsilon'$ that solves (2.24), this error representation $\varepsilon'$ is proportional to the discrete system's residual [Calo et al., 2020b; Rojas et al., 2021]. From the definition of $\mathbb{V}'_h$, we know that

$$b_h(\varepsilon', \bar{v}) = 0, \qquad \forall \bar{v} \in \bar{\mathbb{V}}_h.$$

Also, from (2.29), we have that

$$b_h(v, \tilde{u}) = g(v, \varepsilon'), \qquad \forall v \in \mathbb{V}_h; \tag{2.30}$$

next we add a heuristic interaction of $\varepsilon'$ with the whole test space $\mathbb{V}_h$ to the fine-scale driving force. Thus, we postulate the following problem, where the heuristic fine scales $\check{u} \in \mathbb{V}_h$ solve

$$b_h(v, \check{u}) = g(v, \varepsilon') + b_h(\varepsilon', v) \qquad \forall v \in \mathbb{V}_h. \tag{2.31}$$

Thus, this heuristic fine-scale postprocessing of the error representative includes two extra contributions:

$$b_h(\hat{v}, \check{u}) = b_h(\varepsilon', \hat{v}) \qquad \forall \hat{v} \in \hat{\mathbb{V}}_h, \tag{2.32}$$

$$b_h(v', \check{u}) = \ell_h(v') + b_h(\varepsilon', v') \qquad \forall v' \in \mathbb{V}'_h, \tag{2.33}$$

where the first equation contributes to the coarse-scale trial space in $\bar{\mathbb{V}}_h$ while the second one contributes to the fine-scale trial space $\tilde{\mathbb{V}}_h$. In short, we propose the following heuristic adjoint variational multiscale reconstruction such that:

$$\phi = \bar{u} + \check{u},$$

where $\check{u} \in \mathbb{V}_h$ is the reconstructed fine-scale solution that solves (2.31) for a given error estimate $\varepsilon'$. Alternately, using equations (2.30) and (2.31), we can derive the reconstructed fine-scale solution ($\check{u}$) in terms of the fine scale $\tilde{u}$:

$$\check{u} = \tilde{u} + \acute{u},$$

where $\acute{u}$ represents the heuristic reconstructed fine-scale solution that satisfies:

$$b_h(v, \acute{u}) = b_h(\varepsilon', v) \qquad \forall v \in V_h. \tag{2.34}$$

In the next section, we evaluate the performance of $\phi$ in the norms $L_2$ and $\mathcal{V}_h$, relative to the exact solution $u_{\text{exa}}$ . Our findings reveal a notable improvement in the asymptotic regime, particularly for diffusion-dominated problems (i.e. $\|u_{\text{exa}} - \phi\|_{\mathcal{V}_h} \lesssim \|u_{\text{exa}} - u\|_{\mathcal{V}_h}$,)

## Adaptive Mesh Refinement

The adaptive refinement procedure unfolds through several stages. Initially, the saddle-point problem (2.23) delivers an error representation ($\varepsilon \in \mathbb{V}_h$) within the norm ($|\varepsilon|^2_{\mathbb{V}}$). Following this, a local adaptation of the norm (2.11) is constructed, thereby creating an error indicator for each cell ($E_K$), defined as follows:

$$\begin{aligned} E_K^2 = \|\varepsilon\|^2_{\mathbb{V},Loc} := \kappa\|\nabla\varepsilon\|^2_{0,K} + \beta_c^{-1} h_K \|\beta\cdot\nabla\varepsilon\|^2_{0,K} + \\ \sum_{F\in\mathscr{S}_h} \left(n_e\kappa + \tfrac{1}{2}|\beta\cdot\mathbf{n}_F|\right)([\![\varepsilon]\!],[\![\varepsilon]\!])_{0,F.} \end{aligned} \tag{2.35}$$

Here, we extend the original Dörfler bulk-chasing criterion [Dörfler, 1996] to mark the cells with the highest $E_K$ values based on an accumulative error in a cell loop [Calo et al., 2020b; Rojas et al., 2021]. We first organise the cells in the order of decreasing error per cell. Then, the algorithm marks the elements in two cases: when the accumulative error in a first loop reaches a user-defined fraction of the error $\|\varepsilon\|^2_{\mathbb{V}}$, and when the error of the remaining cells in the first loop is larger than a chosen fraction of the last refined element. By refining all elements with comparable errors in an iteration, we guarantee refinement in the elements close to the cutoff, which the original strategy did not mark; this combined strategy reduces the computational cost per iteration. Let $\eta_{ref}$ be 0.25 in 2D and 0.125 in 3D and $\nu = 0.2$ in all cases. Then, we refine the marked cells using bisection. Algorithm 1 summarises the marking strategy. The stopping criterion for the refinement algorithm is as follows. Starting with a coarse mesh, we refine while the total estimated error in the norm $\|\varepsilon\|_{\mathbb{V}}$ remains above a user-defined tolerance $C_{tol}$. We use in this research $C_{tol} = 1 \times 10^{-5}$.

**Algorithm 1** Marking strategy

**Input:** $\mathfrak{T}_h, \|\varepsilon\|^2_{\mathbb{V}}, \eta_{ref}, N, \nu$

Compute $E_K$ for all $K \in \mathfrak{T}_h$ from (2.35)
Sort and store in `sortK` all $K \in \mathfrak{T}_h$ from highest to lowest $E_K$ values
Initialise cell to mark `Kmarked` = `sortK`[0]
Initialise the local error of the marked mesh cell $E_{Km} = E_K$[`Kmarked`]
Initialise sum = 0, i = 0, flag = `True` and $E_{cut} = 0$
**while** (sum $< \eta^2_{ref}\|\varepsilon\|^2_{\mathbb{V}}$ **or** $E_{Km} \geq (1-\nu)E_{cut}$ ) **and** i $< N$ **do**
    Mark `Kmarked`
    **if** sum $< \eta^2_{ref}\|\varepsilon\|^2_{\mathbb{V}}$ **then**
        sum $\leftarrow$ sum $+E_{Km}$
    **else**
        **if** flag **then**
            $E_{cut} \leftarrow E_{Km}$
            flag $\leftarrow$ `False`
    i $\leftarrow$ i $+1$
    `Kmarked` $\leftarrow$ `sortK`[i]
    $E_{Km} \leftarrow E_K$[`Kmarked`]

## 2.4 Numerical examples

Drawing upon a series of numerical examples, we showcase the potency of our methods in diverse linear scenarios. We then turn our focus to the decay rate analysis for both the coarse and fully reconstructed solutions within the $L_2$ and energy ($\mathbb{V}_h$) norms, following a comparison with the traditional dG solution. Subsequently, convergence plots are illustrated, putting the error norm in context with the total degrees of freedom ($DoF^{1/d}$), that is, $\dim(\bar{\mathbb{V}}_h) + \dim(\mathbb{V}_h)$. We validate our formulation by evaluating and comparing the performance of our multiscale approach using some test problems described in Cier et al. [2021b].

$$\text{SOLVE} \rightarrow \text{ESTIMATE} \rightarrow \text{MARK} \rightarrow \text{REFINE} \tag{2.36}$$

We solve the saddle point problem in (2.17) employing an iterative algorithm described in Bank et al. [1989]; Calo et al. [2020b] and use FEniCS [Alnæs et al., 2015] as a platform to perform all the numerical simulations.

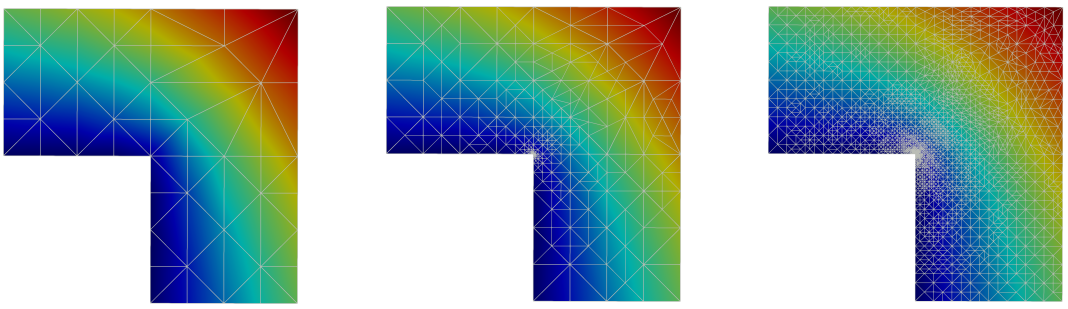

Level= 0 Level = 10 Level = 20

**Figure 2.2:** Solution for the re-entrant corner problem for different refinement levels

### 2.4.1 Diffusion in a domain with a re-entrant corner

We study the method's performance with the diffusion problem in a re-entrant corner domain [Mitchell, 2013]. The problem configuration induces a singularity at the inward-pointing vertex of the concave polygon. Since capturing corner singularities is challenging for uniform refinement techniques, this problem tests the adaptive grid refinement algorithms. We solve the following Laplace equation in an L-shape domain $\Omega$:

$$\begin{aligned} \Delta u &= 0, && \text{in } \Omega = (-1,1)^2 \backslash (-1,0]^2, \\ u &= u_D, && \text{on } \partial\Omega = \Gamma_D, \end{aligned}$$

where the Dirichlet boundary conditions ($u_D$) satisfy the exact solution:

$$u_{exa} = r^{\alpha} \sin(\alpha\theta),$$

with $r = \sqrt{x^2 + y^2}$, $\theta = \tanh^{-1}(y/x)$ and $\alpha = 2/3$.

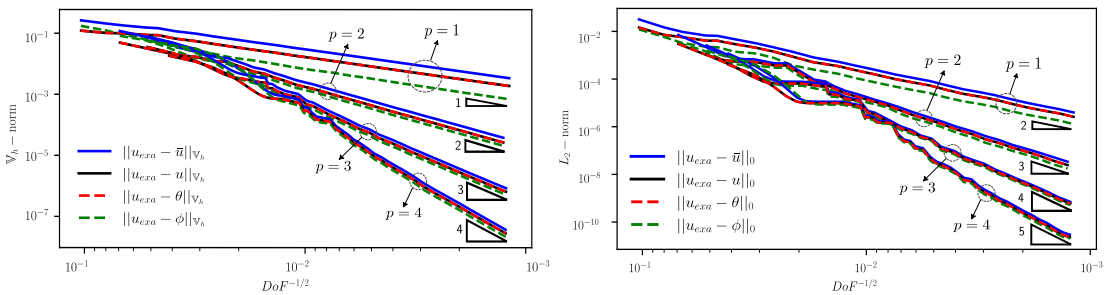


**(a)** $\mathbb{V}_h$ norm **(b)** $L_2$ norm

**Figure 2.3:** $\mathbb{V}_h-$ & $L_2-$norm convergence for Laplace problem

Figure 2.2 shows three surface plots of the full-scale solution and the corresponding meshes for different adaptive refinement levels. The results show the error estimator's robustness and the energy norm's effectiveness at capturing the singularity. Convergence plots are presented in Figure 2.3 for different test-function polynomial degrees ($p = 1, 2, 3, 4$) in the $L_2$ and energy norms. Here, we show optimal rate decay for coarse $\bar{u}$ and full-scale $\tilde{u}$ solutions and verify that the fine-scale contribution $\tilde{u}$ recovers the dG approximation $\theta$ (i.e., $u \approx \theta$ ). Besides, we also show in Figure 2.3 that the extended solution ($\phi$) improves the approximation compared to $u$ and $\theta$ regardless of the polynomial degree.

### 2.4.2 Diffusion in a 3D domain with a Fichera corner

We extend results in Section 2.4.1 for the 3D Fichera corner problem. In this problem, we induce the singularity in the re-entrant corner of a concave polyhedral with domain $\Omega = (-1, 1)^3 \backslash [0, 1)^3$. We consider the problem:

$$\begin{aligned} -\Delta u &= f, \quad \text{in } \Omega, \\ u &= u_D, \quad \text{on } \Gamma_D, \end{aligned} \tag{2.37}$$

where the source term $f$ and Dirichlet boundary conditions ($u_D$) are derived from the exact solution:

$$u_{exa} = \left(\sqrt{x^2 + y^2 + z^2}\right)^q,$$

with $q = 1/10$ and $q = 1/3$. Similarly to the 2D case, uniform refinement techniques may struggle to accurately capture the behavior in the Fichera corner. The high spatial gradients and the necessity for fine meshes at the singularity lead to suboptimal convergence when no adaptive refinement techniques are used [Calo et al., 2020b]. Figures 2.4 and 2.5 display the convergence plots in $L_2$ and $\mathbb{V}_h$ norms. Here, we test the robustness of the error estimator to provide optimal convergence rates for the coarse solution and to recover the dG solution and optimality in the full-scale solution for different $q$ values. Moreover, similar to the example in Section 2.4.1, the extended solution ($\phi$) not only provides a better approximation compared to the full-scale solution ($u$) in the $L_2$ and energy norm but also improves the pre-asymptotic convergence rates, especially for linear polynomial trial functions ($p = 1$).

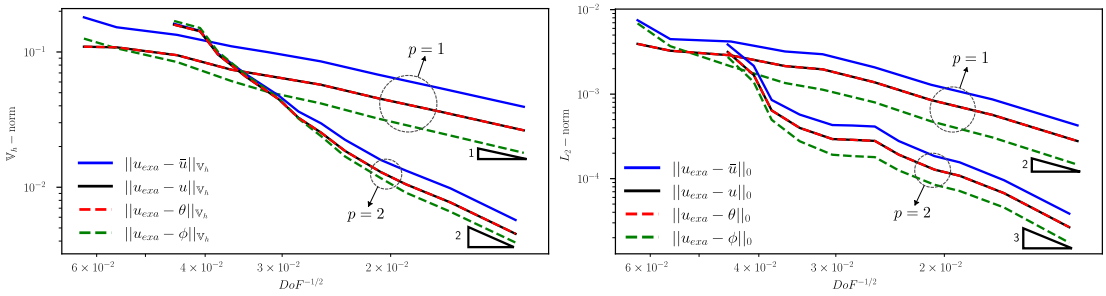


**(a)** $\mathbb{V}_h$ norm **(b)** $L_2$ norm

**Figure 2.4:** $\mathbb{V}_h-$ and $L_2-$norm convergence for Fichera corner, $q = \dfrac{1}{10}$

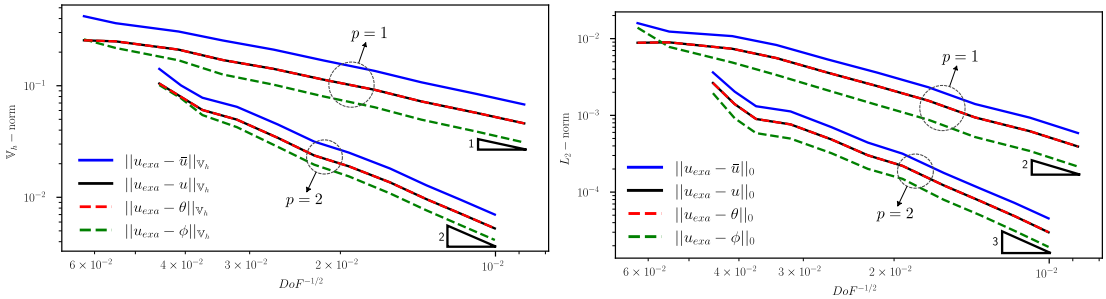


**(a)** $L_2$ norm

**Figure 2.5:** $\mathbb{V}_h-$ and $L_2-$norm convergence for Fichera corner, $q = \dfrac{1}{3}$

### 2.4.3 Heterogeneous Diffusion problem

For this case, we solve the following advection-diffusion equation with heterogeneous and anisotropic diffusion:

$$\begin{aligned} -\nabla(\kappa \cdot \nabla u) + \beta \cdot \nabla u = 0, \quad & \text{in } \Omega, \\ u = u_D, \quad & \text{on } \Gamma, \end{aligned} \tag{2.38}$$

where $\beta = (0, 1)^T$ and $\kappa$ has different $\epsilon_i$ values in each domain:

$$\kappa|_{\Omega_i} = \begin{pmatrix} \epsilon_i & 0 \\ 0 & 1.0 \end{pmatrix}.$$

We partition $\Omega = [0, 1]^2$ into two domains: $\Omega_1 = [0, \frac{1}{2}] \times [0, 1]$ and $\Omega_2 = [\frac{1}{2}, 1] \times [0, 1]$, such that $\epsilon_1 = 0.1$ and $\epsilon_2 = 1.0$, and the Dirichlet boundary condition

$(u_D)$ satisfy the exact solution for each domain [Burman & Zunino, 2006]:

$$u_{exa} = \begin{cases} \left(u_{1/2} - \exp\left(\frac{1}{2\epsilon_1}\right) + (1-u_{1/2})\exp\left(\frac{x}{\epsilon_1}\right)\right) / \left(1 - \exp\left(\frac{1}{2\epsilon_1}\right)\right) & \text{if} \quad x \in \Omega_1, \\ \left(-\exp\left(\frac{1}{2\epsilon_2}\right) u_{1/2} + u_{1/2}\exp\left(\frac{x-\frac{1}{2}}{\epsilon_2}\right)\right) / \left(1 - \exp\left(\frac{1}{2\epsilon_2}\right)\right) & \text{if} \quad x \in \Omega_2, \end{cases} \tag{2.39}$$

where

$$u_{1/2} = \left(\frac{\exp\left(\frac{1}{2\epsilon_1}\right)}{1-\exp\left(\frac{1}{2\epsilon_1}\right)}\right)\left(\frac{\exp\left(\frac{1}{2\epsilon_1}\right)}{1-\exp\left(\frac{1}{2\epsilon_1}\right)} + \frac{1}{1-\exp\left(\frac{1}{2\epsilon_2}\right)}\right)^{-1}.$$

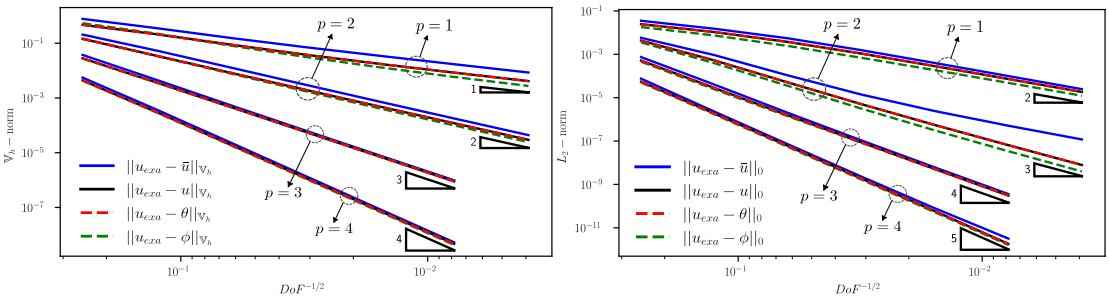


**(a)** $\mathbb{V}_h$ norm **(b)** $L_2$ norm

**Figure 2.6:** $\mathbb{V}_h-$ & $L_2-$norm convergence for heterogeneous diffusion problem

Figure 2.6 shows the $L_2$ and energy $(\mathbb{V}_h)$ norm convergence for polynomial orders 1 to 4. As in Cier et al. [2021b], Figure 2.6b shows a loss in the convergence rate in the $L_2$-norm for the coarse-scale solution $(\bar{u})$ for even polynomial degrees. However, we can recover dG optimality in both norms by including the fine-scale contribution in the full-scale solution $(u)$, regardless of the polynomial degree. Besides, as was shown in previous examples, the extended solution $(\phi)$ has better accuracy than the other discrete approximations on the same mesh.

### 2.4.4 Strongly anisotropic diffusion

We test the performance of our method in a highly anisotropic diffusion problem. We solve the equation (2.38) for $\beta = 0$ and high contrast in the permeability tensor:

$$\kappa|_\Omega = \begin{pmatrix} \alpha_\kappa & 0 \\ 0 & \gamma_\kappa \end{pmatrix}. \tag{2.40}$$

The anisotropy ratio is $r_\kappa$, that is, the ratio between the maximum and minimum

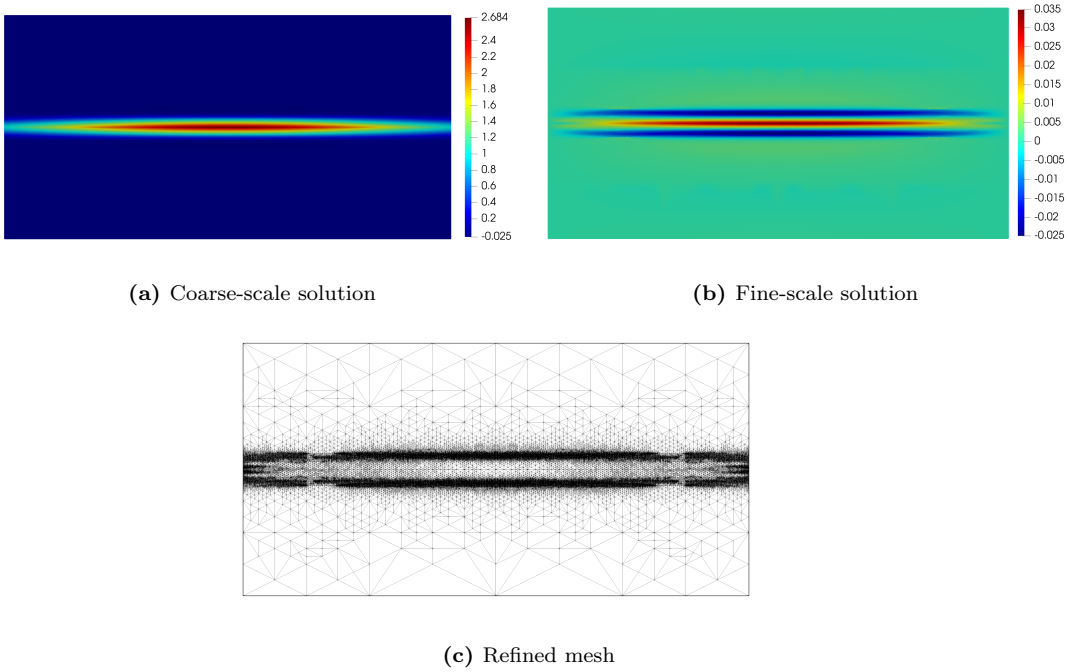


**(a)** Coarse-scale solution

**(b)** Fine-scale solution

**(c)** Refined mesh

**Figure 2.7:** Coarse- & fine-scale solutions with final mesh for strongly anisotropic diffusion problem with $r = 10^6$ & $p = 1$

values of the diffusion coefficients. Specifically, we set $r_\kappa := \alpha_\kappa/\gamma_\kappa$ for (2.40). The problem is more challenging for high $r_\kappa$ values, corresponding to locally small weights in the diffusion tensor, leading to advection-dominated regimes. We study the method's performance by solving (2.40) for different values of the anisotropy ratio by imposing a sharp inner layer problem based on the following Gaussian-function-type manufactured solution, as described in Pestiaux et al. [2014]:

$$u_{exa} = \frac{\exp(-[x^2 + r_\kappa \tau y^2])}{4\pi\sqrt{r_\kappa \tau}}, \tag{2.41}$$

with $\tau = 10^{-3}$. We use (2.41) and $\alpha_\kappa = 1$ to derive the source term $(f)$ and Dirichlet boundary conditions $(u_D)$ in the domain $\Omega = [-1, 1] \times [-0.5, 0.5]$. Figure 2.7 presents the coarse- and fine-scale solutions showing the discontinuity in $y = 0$ and the robustness in the error estimator to effectively refine the inner layers. Figures 2.8 and 2.9 show the convergence plots for $r_\kappa = 10^4$ and $r_\kappa = 10^6$, respectively. We obtain optimal rates for different polynomial degrees in the $\mathbb{V}_h$ and $L_2$ norms for all discrete approximations on the refined-mesh sequences.

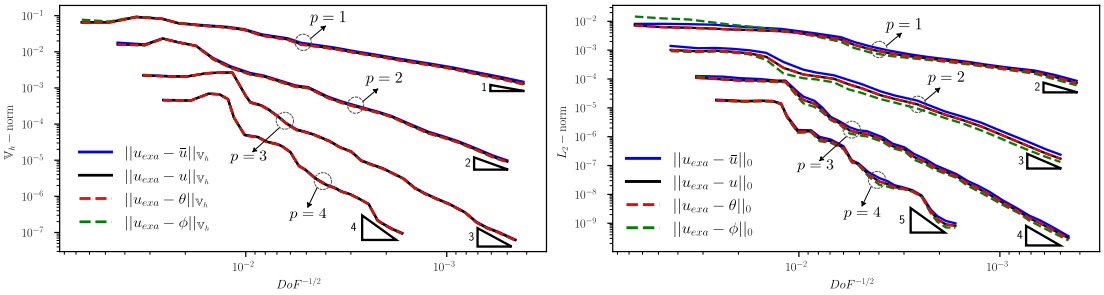


**(a)** $\mathbb{V}_h$ norm **(b)** $L_2$ norm

**Figure 2.8:** $\mathbb{V}_h-$ and $L_2-$norm convergence for anisotropy ratio $r_\kappa = 10^4$.

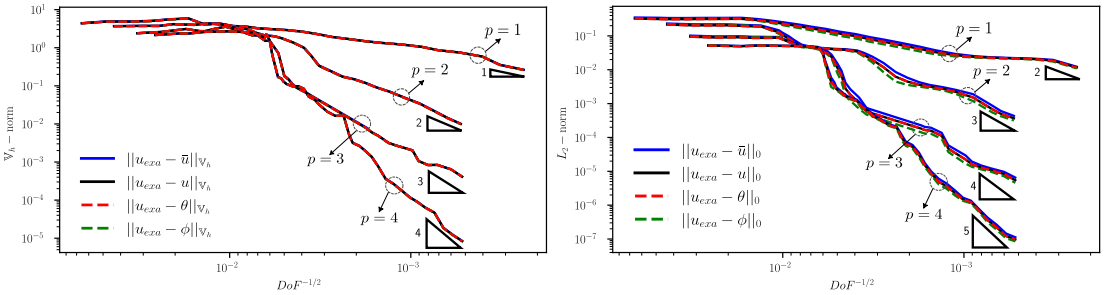


**(a)** $\mathbb{V}_h$ norm **(b)** $L_2$ norm

**Figure 2.9:** $\mathbb{V}_h-$ and $L_2-$norm convergence for anisotropy ratio $r_\kappa = 10^6$.

### 2.4.5 3D Eriksson-Johnson problem

We use a 3D version of the classical Eriksson-Johnson problem [Chan & Evans, 2013; Cier et al., 2021b]. We solve the equation (2.38) in the domain $\Omega = [0,1]^3$ with diffusion coefficient $\kappa = 10^{-2}$, velocity field $\beta = (1,0,0)^T$ and a source term $f = 0$. We impose Dirichlet boundary conditions using the analytical solution:

$$u_{exa} = \frac{\exp(r_1(x-1)) - \exp(r_2(x-1))}{\exp(-r_1) - \exp(-r_2)} \sin(\pi y),$$

with $r_{1,2} = 1 \pm \sqrt{1+4\kappa^2\pi^2}/2\kappa$. Figure 2.10 shows the coarse and fine scales for linear solutions, $p = 1$, and how the adaptive strategy captures the regions with sharp gradients, constructing a smooth solution. Figures 2.11 and 2.12 show the optimal convergence plot in $\mathbb{V}_h$ and $L_2$ norms for the coarse- and full-scale approximations. Again, the adjoint multiscale reconstruction improves the $\mathbb{V}_h$ norm and the pre-asymptotic convergence, especially for lower-order polynomials.

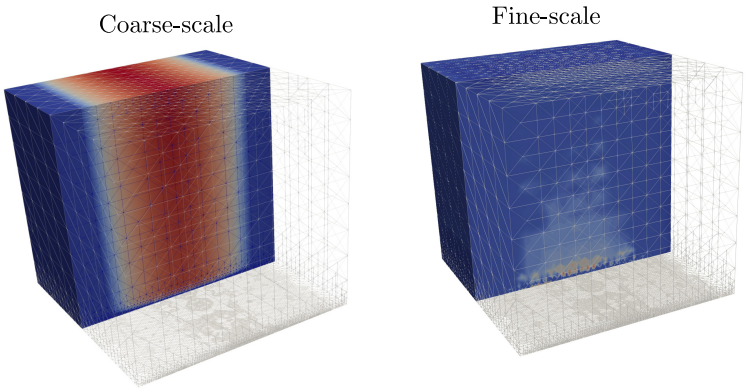


**Figure 2.10:** Convergence in $L_2$ norm for the 3D Eriksson-Johnson problem

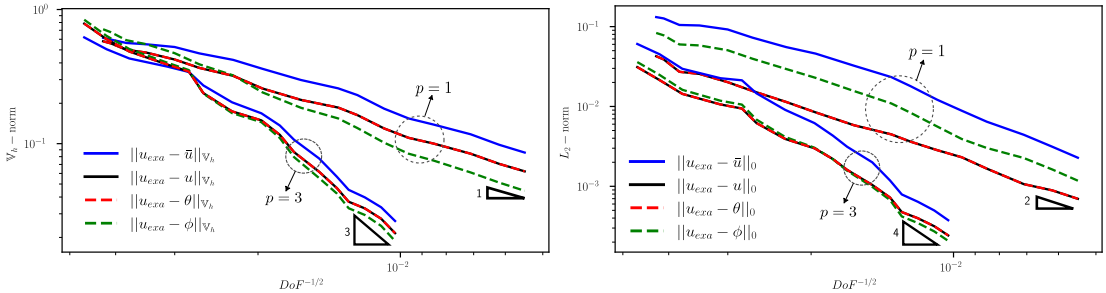


**(a)** $\mathbb{V}_h$ norm **(b)** $L_2$ norm

**Figure 2.11:** $\mathbb{V}_h-$ and $L_2-$norm convergence for 3D Eriksson-Johnson problem, $p = 1, 3$

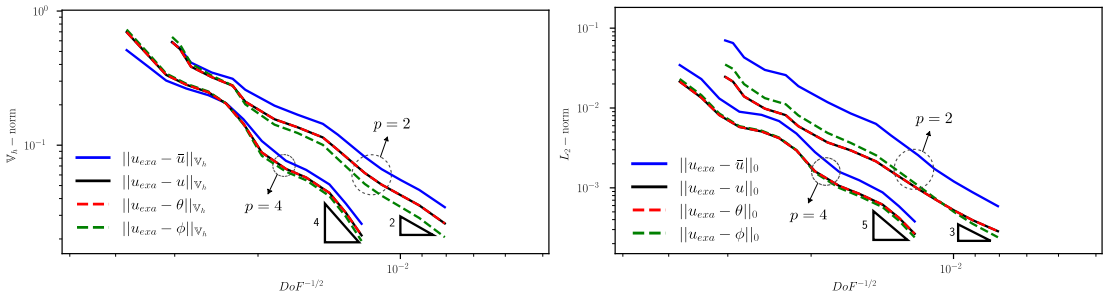


**(a)** $\mathbb{V}_h$ norm **(b)** $L_2$ norm

**Figure 2.12:** $\mathbb{V}_h-$ and $L_2-$norm convergence for 3D Eriksson-Johnson problem, $p = 2, 4$

## 2.5 Extension to nonlinear conservation laws

Next, we analyse the numerical stability of nonlinear conservation laws in the context of variational multiscale reconstructions. First, we formulate the discrete problem using the Lax-Friedrich flux for the nonlinear advective flux within the

discontinuous Galerkin (dG) framework. Then, we outline the variational multiscale method for nonlinear problems following Juanes & Patzek [2005], extending this framework to our adaptive stabilised finite element method to derive a nonlinear fine-scale approximation. We present some numerical results for Burgers' equation to demonstrate the accuracy and efficiency of our approach.

### 2.5.1 Discontinuous Galerkin discretisation

We consider the following nonlinear conservation law:

$$\begin{aligned} \nabla \cdot (\mathrm{f}(u) - \kappa \nabla u) &= f, \qquad && \text{in } \Omega, \\ u &= u_D, && \text{on } \Gamma_D, \end{aligned} \tag{2.42}$$

where $\mathrm{f}(u)$ is a nonlinear convective flux; thus, the dG discrete problem reads:

$$\begin{cases} \text{Find } u \in \mathbb{V}_h, \text{ such that:} \\ n_h(v;u) = \ell_h(v), \qquad \forall\, v \in \mathbb{V}_h, \end{cases} \tag{2.43}$$

where $n(v;u)$ represents the nonlinear form including a SWIP contribution in (2.7) and the Lax-Friedrichs numerical flux $\Phi$ for the nonlinear convective flux defined as follows:

$$n_h(v;u) = b_h(v,u)^{\text{swip}} - \sum_{K\in\mathfrak{T}} (\nabla v, \mathrm{f}(u))_K + \sum_{F\in\mathscr{S}_h} (\llbracket v \rrbracket, \Phi)_F, \tag{2.44}$$

with,

$$\begin{aligned} &\forall F \in \mathscr{S}_h^0, \quad \Phi := \frac{1}{2}(\mathrm{f}(u_1)\cdot\mathbf{n}_F + \mathrm{f}(u_2)\cdot\mathbf{n}_F + \eta_f(u_1-u_2)), \\ &\forall F \in \mathscr{S}_h^D, \quad \Phi := \frac{1}{2}(\mathrm{f}(u)\cdot\mathbf{n}_F + \eta_f\, u) + \frac{1}{2}(\mathrm{f}(u_D)\cdot\mathbf{n}_F - \eta_f\, u_D). \end{aligned} \tag{2.45}$$

where $\eta_f$ is a local dissipation parameter parametrised by the maximum eigenvalue of the flux function Jacobian. In equation (2.62), we set

$$\begin{aligned} &\forall F \in \mathscr{S}_h^0, \quad \eta_f := \max_{w=u_1,u_2} |\mathrm{f}'(w)\cdot\mathbf{n}_F|, \\ &\forall F \in \mathscr{S}_h^D, \quad \eta_f := |\mathrm{f}'(u)\cdot\mathbf{n}_F|. \end{aligned} \tag{2.46}$$

The right-hand side in (2.43) for weakly imposed non-homogeneous Dirichlet boundary conditions reads:

$$\ell_h(v) := \sum_{K\in\mathfrak{T}}(v,f) + \sum_{F\in\mathscr{S}_h^D}\left(n_e\kappa(v,u_D)_F - (\kappa\nabla v\cdot\mathbf{n}_F,u_D)_F\right) - \sum_{F\in\mathscr{S}_h^D\cap\Gamma}\tfrac{1}{2}\left(v,\mathrm{f}(u_D)\cdot\mathbf{n}_F-\eta_f u_D\right)_F. \tag{2.47}$$

We endow $\mathbb{V}_h$ with the norm:

$$\|w\|^2_{\mathbb{V}_h} := \|w\|^2_{\text{swip}} + \|w\|^2_{\text{conv}}, \tag{2.48}$$

with $\|w\|^2_{\text{swip}}$ the SWIP norm contribution (2.13) and $\|w\|^2_{\text{conv}}$ a convective norm defined as follows:

$$\|w\|^2_{\text{conv}} := \|w\|^2_0 + \sum_{F\in\mathscr{S}_h}\|[\![w]\!]\|^2_{0,F} + \sum_{K\in\mathfrak{T}} h_K\|\nabla w\|^2_{0,K}. \tag{2.49}$$

It is important to note that, in this non-linear problem, the advective and reactive coefficients vary with each iteration. Consequently, we enforced the energy norm with a unit values for both the $L^2$ and $H^1$ contributions. This approach guarantees a fixed reference for the residual convergence in the residual minimisation.

### 2.5.2 Residual minimisation formulation

Extending the residual minimisation formulation of Section 2.2 and the nonlinear approach for residual minimisation problems [Cier et al., 2021a], we formulate the following nonlinear saddle-point problem to obtain the coarse-scale solution and an error estimate:

$$\begin{cases} \text{Find } (\varepsilon,\bar{u})\in\mathbb{V}_h\times\bar{\mathbb{V}}_h, \text{ such that:} \\ g(v,\varepsilon)+n_h(v;\bar{u}) = \ell_h(v), \qquad \forall v\in\mathbb{V}_h, \\ n_h'(\varepsilon,\bar{w};\bar{u}) = 0, \qquad \forall\bar{w}\in\bar{\mathbb{V}}_h. \end{cases} \tag{2.50}$$

Here, $n_h'(v,\delta u;u)$ is the linearised form of the nonlinear operator (2.44), evaluated at $\bar{u}\in\mathbb{V}_h$, and defined through the discrete Gâteux derivative in the direction $\delta\bar{u}\in\mathbb{V}_h$ as:

$$n_h'(v,\delta\bar{u};\bar{u}) := \frac{d}{d\epsilon}n_h(v;\bar{u}+\epsilon\delta\bar{u})\big|_{\epsilon=0.} \tag{2.51}$$

We use the Newton-Raphson method to solve (2.50) so that, at each step of the nonlinear iteration, we solve the following linear problem:

$$\begin{cases} \text{Given } (\varepsilon_i, \bar{u}_i), \text{ find } (\delta\varepsilon, \delta\bar{u}) \in \mathbb{V}_h \times \bar{\mathbb{V}}_h, \text{ such that:} \\ g(v, \delta\varepsilon) + n'_h(v, \delta\bar{u}; \bar{u}_i) = \ell_h(v) - g(v, \varepsilon_i) - n_h(v, \bar{u}_i) \qquad \forall v \in \mathbb{V}_h, \\ n'_h(\delta\varepsilon, \bar{w}; \bar{u}_i) = -n'_h(\varepsilon_i, \bar{w}; \bar{u}_i) \qquad \forall \bar{w} \in \bar{\mathbb{V}}_h. \end{cases} \tag{2.52}$$

We update $u_i$ and $\varepsilon_i$ at every iteration $i$ such that:

$$\bar{u}_{i+1} = \bar{u}_i + k\delta\bar{u}, \qquad \varepsilon_{i+1} = \varepsilon_i + k\delta\varepsilon \tag{2.53}$$

and assume convergence when $\|\bar{u}_{i+1} - \bar{u}_i\|_{\mathbb{V}_h} < 10^{-6}$. We use a damped Newton algorithm to solve the corresponding nonlinear saddle point problem. We denote the relaxation parameter as $k$ in (2.53), following Bank & Rose [1981] (see algorithmic details in Cier et al. [2021a]). Regarding error estimation, we adopt a similar approach to that used in the linear problem. Here, $\varepsilon$ in equation (2.50) represents the residual error of the nonlinear operator, i.e., $g(v, \varepsilon) = \ell_h(v) - n_h(v; \bar{u})$. However, we use the updated residual error $(\varepsilon_{i+1})$ to guide adaptivity after the solution of (2.52) converges.

### 2.5.3 Nonlinear variational multiscale method

As above, a natural approach to solve (2.43) is to linearise the equation and update the solution with a correction term at every iteration as:

$$u_{i+1} = u_i + \delta u. \tag{2.54}$$

In a multiscale context, both $u_i$ and $\delta u$ in (2.54) are decomposed into fine-scale $(\tilde{u}_i,\ \delta\tilde{u})$ and coarse-scale $(\bar{u}_i,\ \delta\bar{u})$ components. We circumvent the need for decomposing $u_i$ at each iteration by using a decoupled scale system by employing the subsequent approximation [Juanes & Patzek, 2005]:

$$u_i \approx \bar{u}_i,$$

which assumes, at each iteration, that

$$u_{i+1} \approx \bar{u}_{i+1} + \delta\tilde{u}. \tag{2.55}$$

We simplify the notation in (2.55) by dropping the sub-index $i$:

$$u \approx \bar{u} + \delta\tilde{u}. \tag{2.56}$$

From this, we define a multiscale formulation through defining a nonlinear direct sum decomposition for both the trial and test function spaces:

$$u = \bar{u} + \delta\tilde{u} \qquad \forall u \in \mathbb{V}_h, \tag{2.57}$$

$$v = \hat{v} + v' \qquad \forall v \in \mathbb{V}_h, \tag{2.58}$$

where $\bar{u} \in \bar{\mathbb{V}}_h$, $\delta\tilde{u} \in \tilde{\mathbb{V}}_h$, $\hat{v} \in \hat{\mathbb{V}}_h$, and $v' \in \mathbb{V}'_h$. Using (2.57) in the nonlinear problem (2.43), and using a first-order Taylor expansion about the coarse-scale solution $\bar{u}$, the nonlinear form becomes:

$$n_h(v;u) = n_h(v;\bar{u}+\delta\tilde{u}) \approx n_h(v;\bar{u}) + n'_h(v,\delta\tilde{u};\bar{u}) \quad v \in \mathbb{V}_h. \tag{2.59}$$

Drawing from the first equation in the nonlinear saddle-point problem in (2.50) and employing (2.43) and (2.59), we obtain the following identity:

$$\begin{cases} \text{Find } \delta\tilde{u} \in \mathbb{V}_h, \text{ such that:} \\ n'_h(v,\delta\tilde{u};\bar{u}) = g(v,\varepsilon') \quad \forall v \in \mathbb{V}_h. \end{cases} \tag{2.60}$$

Here, we use $\varepsilon$ and $\bar{u}$ from (2.50) after the system converges. Similar to the linear case, in the subsequent sections, we represent the reconstructed full-scale solution (Equation (2.57)) as $(u)$ and the dG solution in (2.43) as $(\theta)$. Unlike the linear problem, $u$ is not equivalent to, but rather an approximation of $\theta$ (i.e., $u \approx \theta$). The decoupled multiscale formulation substantially reduces computational costs by eliminating the need for explicit decomposition of $u_i$ into coarse- and fine-scale components during each iteration. Instead, the decomposition is only performed once at each iteration level. In the next section, we demonstrate that our approach and the adaptive strategy yield an accurate and stable approximation of the coarse-scale solution and error indicator. This approximation enables the recovery of the full-scale solution following refinement.

### 2.5.4 Adjoint multiscale reconstruction

As for the linear case, we define the adjoint multiscale reconstruction $\phi$ as:

$$\phi = \bar{u} + \delta\check{u},$$

where $\delta\check{u}$ denotes the fine-scale adjoint reconstruction, such that:

$$\begin{cases} \text{Find } \delta\check{u} \in \mathbb{V}_h, \text{ such that:} \\ n'_h(v, \delta\check{u}; \bar{u}) = g(v, \varepsilon') + n'_h(\varepsilon', v; \bar{u}) \quad \forall v \in \mathbb{V}_h. \end{cases} \tag{2.61}$$

The next example shows the improved accuracy of the adjoint reconstruction ($\phi$) for the asymptotic regime in the energy norm (i.e., $||u_{exa} - \phi||_{\mathbb{V}_h} \lesssim ||u_{exa} - u||_{\mathbb{V}_h}$).

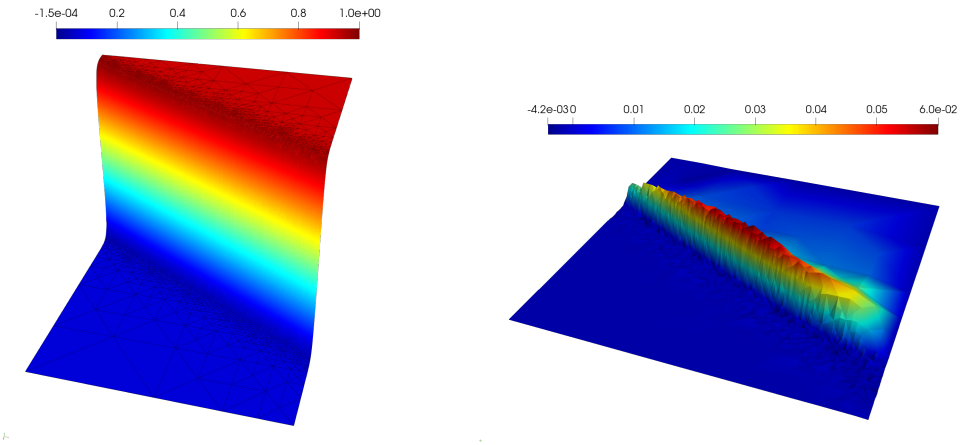


**(a)** Coarse-scale solution **(b)** Fine-scale solution

**Figure 2.13:** Solution for Burgers' equation for $\kappa = 10^{-3}$ & $p = 1$

### 2.5.5 Burgers' equation

We evaluate the performance of the proposed variational multiscale reconstructions in a nonlinear problem. We use the steady Burgers equation, a partial differential equation widely used in modelling physical phenomena such as fluid dynamics, shock waves, and traffic flow. In Burgers equation, the nonlinear term instigates the formation of shocks, while the viscous term serves to smooth the solution. In subsequent sections, we analyse the simulation results for both the isotropic and anisotropic versions of this equation.

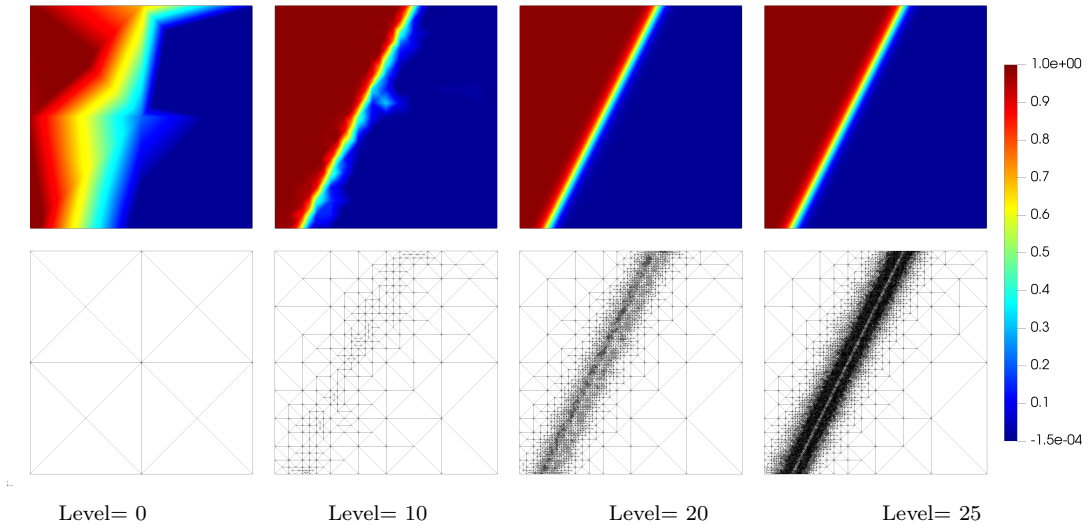


**Figure 2.14:** Solution for the isotropic Burgers equation for different refinement levels at $\kappa = 10^{-3}$

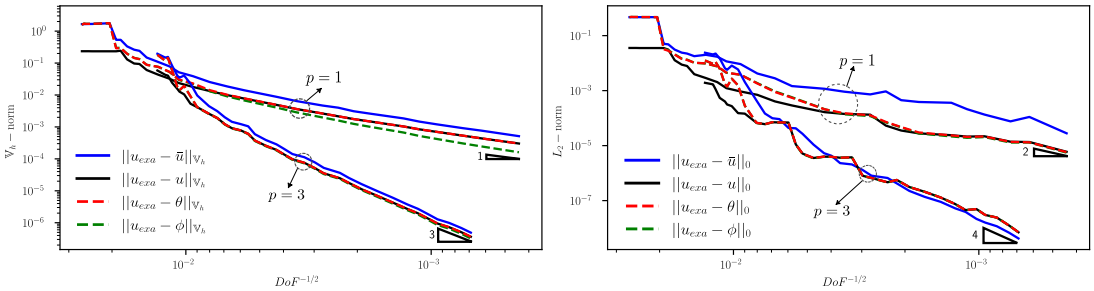


**(a)** $\mathbb{V}_h$ norm **(b)** $L_2$ norm

**Figure 2.15:** Convergence plots for Burgers' equation in the $L_2$ and $\mathbb{V}_h$ norms, $p = 1, 3$

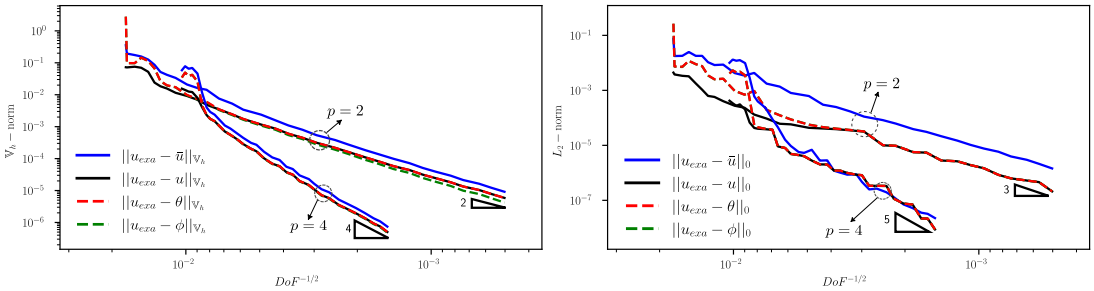


**(a)** $\mathbb{V}_h$ norm **(b)** $L_2$ norm

**Figure 2.16:** Convergence plots for Burgers' equation in the $L_2$ and $\mathbb{V}_h$ norms, $p = 2, 4$

### Isotropic Burgers' equation

We first solve the isotropic case where $\mathrm{f}(u) := \frac{\mathbf{b}u^2}{2}$ with $\mathbf{b} = [1, 1]^T$, which reads:

$$\begin{aligned} \nabla \cdot \left(\frac{\mathbf{b}u^2}{2}\right) - \kappa \Delta u &= f, \quad \text{in } \Omega, \\ u &= u_D, \quad \text{on } \Gamma_D, \end{aligned} \tag{2.62}$$

with $\Omega = [0,1]^2$, $\kappa = 10^{-3}$ and a initial condition $u_0 = 0.5$ which induces an inner discontinuity. We impose the source term $f$ and Dirichlet boundary condition ($u_D$) from the exact solution:

$$u_{exa} = \frac{1}{2}\left(1 - \tanh\left(\frac{2x - y - 0.25}{\sqrt{5\kappa}}\right)\right).$$

We use $f'(w) = \mathbf{b}w$ to impose the local dissipation parameter in (2.46).

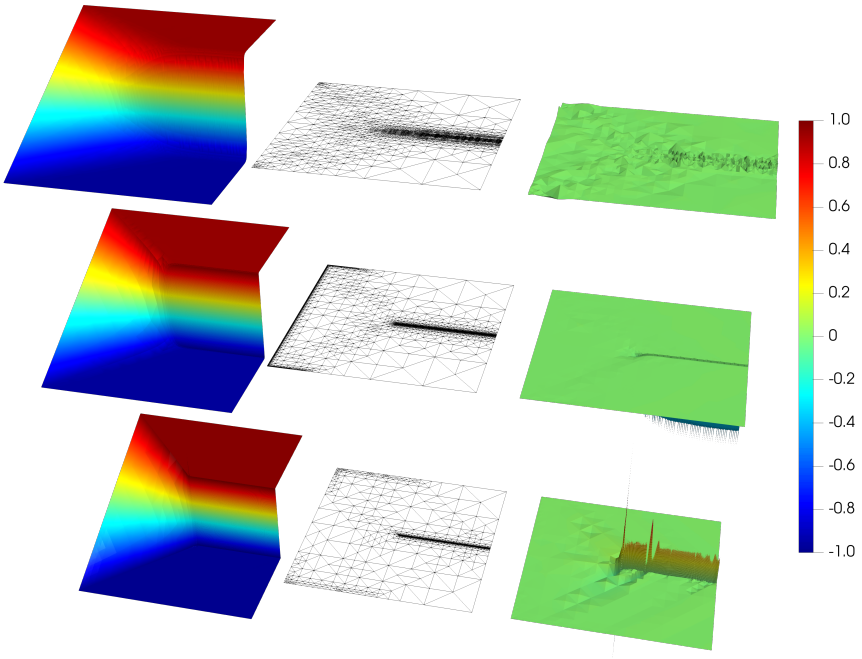


(a) Coarse-scale solution (b) Mesh (c) Fine-scale solution

**Figure 2.17:** Coarse-scale solution and scale approximations for different diffusivities. (top: $\kappa = 10^{-2}$, middle: $\kappa = 10^{-3}$ ,bottom: $\kappa = 10^{-4}$).

Figure 2.13 shows solution plots for $p = 1$, illustrating the smooth approach of the continuous solution and its correction for the fine scale along the discontinuity. Figure 2.14 displays four refinement levels to demonstrate the effectiveness of the refinement strategy in capturing the sharp inner layer, irrespective of the initial mesh. Figures 2.15 and 2.16 depict optimal convergence rates for $p = 1, 2, 3, 4$ in the $L_2$ and $\mathbb{V}_h$ norms. Moreover, we show our method recovers the full-scale solution (i.e., $u \approx \theta$) after refinement, regardless of the polynomial order. Furthermore, as in the linear case, the adjoint multiscale reconstruction ($\phi$) enhances the approximation quality in the $\mathbb{V}_h$ norm.

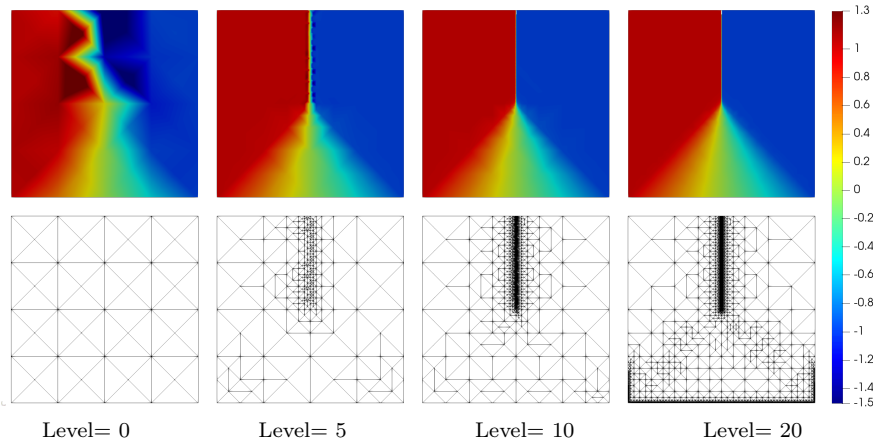


**Figure 2.18:** Solution for the Burgers equation for different refinement levels at $\kappa = 10^{-2}$

### Single-component Burgers' equation

Next, we introduce a second scenario to test the numerical performance in the presence of a sharp shock layer. We select a problem from Moro et al. [2012] to solve Burgers' equation in a single component, such that $\mathrm{f}(u) := \left[\frac{u^2}{2}, u\right]^T$. This problem represents a challenge, especially for convection-dominated problems, due to the shock presence at $x = 0$. The problem reads:

$$\frac{1}{2}\frac{\partial u^2}{\partial x} + \frac{\partial u}{\partial y} = \kappa\left(\frac{\partial^2 u}{\partial x^2} + \frac{\partial^2 u}{\partial y^2}\right), \qquad \text{in } \Omega, \tag{2.63}$$

with $\Omega = [0,1]^2$ and initial guess $u_0 = 1 - 2x$. We impose Dirichlet boundary conditions $u_D = u_0$ at $y = 0$, $x = 0$ and $x = 1$ and zero Neumann boundary conditions at $y = 1$. The local dissipation parameter in (2.46) uses $f'(w) = [u, 1]$. We used a polynomial degree of $p = 3$ and a uniform element size of $4 \times 4$ for the initial mesh. Figure 2.17 illustrates the coarse and fine solutions for $\kappa = 10^{-2}$, $\kappa = 10^{-3}$, and $\kappa = 10^{-4}$. Additionally, Figure 2.18 demonstrates how the adaptive strategy effectively reduces oscillations along the shock for coarse meshes, regardless of the initial mesh [Moro et al., 2012].

## 2.6 Concluding Remarks

In summary, our method is effective and reliable in solving challenging steady linear and non-linear problems, including those with highly heterogeneous, strongly anisotropic, and convective-dominated regimes. We demonstrate the advantage

of our formulation compared to classical methods by providing not only a stable coarse solution and an on-the-fly error estimator to guide adaptivity, but also an improvement in the approximation through a variational multiscale fine-scale reconstruction. We also show that for diffusion-dominated problems, we can use insights behind the adjoint residual-based estimator in goal-oriented adaptivity to formulate a heuristic dual-term contribution in the variational form, which improves the accuracy for the asymptotic regime in the energy norm. Using the tools provided by this framework, we can solve the highly anisotropic and heterogeneous hydraulic problem in Equation (1.1), which arises from the variations in iron concentration through the ore deposit. In the following chapter, we extend the problem to an unsteady case to overcome the challenging unsteady advective-dominated transport propagation.

# Chapter 3

# Unsteady convection-diffusion-reaction problems

In this chapter, we introduce a numerical framework for unsteady advection-diffusion-reaction problems.[1] Here, we extend the framework of Chapter 2 to simulate the unsteady advective-dominated transport propagation (1.2). The method constructs a stabilised finite element method for linear equations using the method of lines. We propose a residual minimisation strategy that uses an ad-hoc modified discrete system that couples a time-marching scheme and a semi-discrete discontinuous Galerkin formulation in space. Our approach offers robust spatial refinements for a user-selected time marching method. We first approximate the spatial derivatives using a space semi-discrete scheme and then solve the resulting system using a time-marching discretisation. As particular examples, we use implicit first- and second-order time-stepping (BDF1 and BDF2) discretisations [Bramble & Thomée, 1972; Crouzeix & Lisbona, 1984].

Compared to other techniques, the main advantage of this method relies on the non-conformity of the starting dG formulation, which allows us to work with stronger norms from the dG theory with a continuous trial space. Moreover, the

[1] The content of this chapter is published in: J.F. Giraldo & V.M. Calo [2023]. An adaptive in space, stabilized finite element method via residual minimization for linear and nonlinear unsteady advection–diffusion–reaction equations. *Mathematical and Computational Applications*; 28(1):7. Some of these results were presented in the 10th International Conference on Adaptative Modeling and Simulation (ADMOS) available on: J.F. Giraldo, S. Rojas & V.M. Calo [2021], An adaptive stabilized finite element method based on residual minimization for unsteady advection-diffusion problems.

refinement strategy and its efficiency in obtaining high-resolution approximations from coarse meshes allow us to overcome the computational cost of implicit temporal schemes and the extra degrees of freedom in the saddle-point formulation. As in the steady case, this combination delivers a stable continuous solution and an on-the-fly error estimate that robustly guides adaptivity at every discrete time. Finally, we incorporate ideas of the multiscale variational formulation in Chapter 2, to reconstruct the fine-scale solution an the adjoint multiscale approach. We show the method's performance in challenging advection-dominated problems to demonstrate stability in the solution and efficiency in the adaptivity strategy.

## 3.1 Problem definition

Maintaining the notation of Section 2.1.1 and letting $V$ represent a Hilbert space, we denote by $C^l(V) := C^l([0,T_f];V)$. This space is spanned by $V$-valued functions that are continuously differentiable up to $l$ times within the interval $[0,T_f]$. Consequently, $C^0(V)$ and $C^1(V)$ correspond to the spaces of continuous and continuously differentiable functions on $[0,T]$, respectively.
We consider the time evolution of the advection-diffusion-reaction solution defined in the space-time cylinder $\Omega \times (0,T]$ for $T>0$. The governing equations in strong form read:

$$\begin{aligned}
\partial_t u - \nabla\cdot\kappa\nabla u + \beta\cdot\nabla u + \mu u &= f && \text{in } \Omega \times (0,T],\\
u &= u_D && \text{on } \Gamma_D \times (0,T],\\
(-\beta u + \kappa\nabla u)\cdot\mathbf{n} &= h_N && \text{on } \Gamma_N^- \times (0,T],\\
\kappa\nabla u\cdot\mathbf{n} &= h_N && \text{on } \Gamma_N^+ \times (0,T],\\
u(\cdot\,, t=0) &= u_0(x) && \text{in } \Omega,
\end{aligned} \tag{3.1}$$

where $f \in C^0(L^2(\Omega))$ the source term, and $u_D \in C^0(H^{1/2}(\Gamma_D))$ and $h_N \in C^0(L^2(\Gamma_N))$ the Dirichlet and Neumann boundary values. We assume that $\beta$, $\kappa$ and $\mu$ are time-independent, and that $(v, \beta\cdot\nabla v + \mu v)_0 \geq 0$.

Denoting $L_\beta$, the Lipschitz modulus of $\beta$, we consider a reference velocity $\beta_c$ and a reference time $\tau_c$ defined respectively as: $\beta_c := \|\beta\|_\infty$ and $\tau_c := \{\max(\|\mu\|_\infty, L_\beta)\}^{-1}$.

## 3.2 Discontinuous Galerkin discretisation and time marching

The approach consists of two primary components. First, we use a spatial semi-discretisation method based on the dG description outlined in Chapter 2. Subsequently, we adopt the method of lines to advance the fully discrete system in time by using either the implicit first- and second-order time-stepping discretisations. The subsequent sections detail these strategies.

### 3.2.1 Space Semi-discretisation

We formulate the space semi-discretisation by combining the symmetric weighted interior penalty (SWIP) and the upwind (UPW) dG formulations of the steady advection-diffusion-reaction equation, see Section 2.1.2. We set $h_K \leq \beta_c \min(T, \tau_c)$ to avoid strong reaction regimes, to allow the mesh to resolve the spatial variation of the velocity field, and to guarantee that a particle at speed $\beta_c$ crosses at least one mesh element over the time interval $(0, T)$. Let the semi-discrete dG approximation (3.1) in the space $\mathbb{V}_h$ (2.3) be: For $t \in (0, T]$, find $\theta$, such that

$$(v, \partial_t \theta)_0 + b_h(v, \theta) = \ell_h(v) \quad \forall\, v \in \mathbb{V}_h, \tag{3.2}$$

with $\theta(0) = \theta_0$, the advection-diffusion-reaction bilinear form $b_h$ (2.6) and we recall $\ell_h(v)$ in (2.10) for weakly non-homogeneous boundary conditions as:

$$\begin{aligned}\ell_h(v) := \sum_{K\in\mathfrak{T}} (v, f_h(t)) + \sum_{F\in\mathscr{I}_h^D} (n_e \kappa (v, u_D)_F - (\kappa \nabla v \cdot \mathbf{n}_F, u_D)_F) \\ - \sum_{F\in\mathscr{I}_h^D \cap \Gamma^-} (v, (\beta \cdot \mathbf{n}_F)\, u_D)_F + \sum_{F\in\mathscr{I}_h^N} (v, u_N)_F.\end{aligned} \tag{3.3}$$

We set $f_h(t) = \pi_h f(t) \quad \forall t \in [0, T]$, where $\pi_h$ is the $L^2$ projection onto $\mathbb{V}_h$. Next, we manipulate functions of the form $(u(t) - v)$ in the space $\mathbb{V}_{*h} := H^1(\Omega) + \mathbb{V}_h$. Thus, we can write an equivalent form of (3.2) in terms of the discrete differential operator $B_h : \mathbb{V}_{*h} \to \mathbb{V}_h$, such that, for all $(u, v) \in \mathbb{V}_{*h} \times \mathbb{V}_h$,

$$(v, B_h u)_0 := b_h(v, u). \tag{3.4}$$

We use the discrete operator $B_h$ to formulate the space semi-discrete problem (3.5) in the form: for each $t \in (0, T]$, then

$$(v, \partial_t \theta(t))_0 + (v, B_h \theta(t))_0 = \ell_h(v) \quad \text{in} \quad \forall v \in \mathbb{V}_h, \tag{3.5}$$

with the initial condition $\theta(0) = \pi_h u(0)$. We endow $\mathbb{V}_h$ with the norm:

$$\|v\|_{\tilde{\mathcal{V}}}^2 := \|v\|_{\text{SWIP}}^2 + \|v\|_{\text{UPWc}}^2, \tag{3.6}$$

and

$$\|v\|_{\mathcal{V}}^2 := \|v\|_{\tilde{\mathcal{V}}}^2 + \sum_{K \in \mathfrak{T}} \beta_c^{-1} h_K \|\beta \cdot \nabla v\|_0^2, \tag{3.7}$$

where the Symmetric Weighted Interior Penalty form (SWIP) from (2.13) and coercive upwinding (UPWc) norms correspond to:

$$\|v\|_{\text{SWIP}}^2 := \kappa \|\nabla v\|_0^2 + \sum_{F \in \mathscr{S}_h} n_e \kappa \|[\![v]\!]\|_{0,F}, \tag{3.8}$$

and

$$\|v\|_{\text{UPWc}}^2 := \tau_c^{-1} \|v\|_0^2 + \tfrac{1}{2} |\beta \cdot \mathbf{n}_F| (v, v)_{0,\Gamma} + \sum_{F \in \mathscr{S}_h^0} \tfrac{1}{2} |\beta \cdot \mathbf{n}_F| ([\![v]\!], [\![v]\!])_{0,F}.$$

Also, we define their corresponding extended norms (3.6) and (3.7) as follows:

$$\|v\|_{\tilde{\mathcal{V}},*}^2 := \|v\|_{\tilde{\mathcal{V}}}^2 + \sum_{K \in \mathfrak{T}} \beta_c \|v\|_{0,\Gamma}^2 + \sum_{K \in \mathfrak{T}} h_K \kappa \|\nabla v \cdot \mathbf{n}\|_{0,\Gamma}^2, \tag{3.9}$$

$$\|v\|_{\mathcal{V},*}^2 := \|v\|_{\mathcal{V}}^2 + \sum_{K \in \mathfrak{T}} \beta_c \left( \|v\|_{0,\Gamma}^2 + h_K^{-1} \|v\|_0^2 \right) + \sum_{K \in \mathfrak{T}} h_K \kappa \|\nabla v \cdot \mathbf{n}\|_{0,\Gamma}^2. \tag{3.10}$$

The discrete operator $B_h$ has the following properties [Ern et al., 2009, § 3-4].

**Theorem 1.** *(Discrete operator $B_h$ properties)*

1. *Consistency: The exact solution $u$ of (3.1) satisfies*

$$\partial_t u(t) + B_h u(t) = \ell_h(t) \qquad \forall t \in (0, T].$$

2. *Boundedness: A constant $C_{bnd} < \infty$, independent of $h$ & $\tau$ exists, such that:*

$$(w, B_h v)_0 \leq C_{bnd} \|w\|_{\tilde{\mathcal{V}}} \|v\|_{\tilde{\mathcal{V}},*} \qquad \forall (w, v) \in \mathbb{V}_h \times \mathbb{V}_h^*.$$

3. *Discrete Coercivity: A constant $C_{sta} > 0$ independent of $h$ & $\tau$ exists, such that:*

$$(v, B_h v)_0 \geq C_{sta} \|v\|_{\tilde{\mathcal{V}}}^2 \qquad \forall v \in V_h.$$

4. *Discrete inf-sup stability: There is a constant $C'_{sta} > 0$, such that:*

$$C'_{sta} \|v\|_{\mathcal{V}} \leq \sup_{w \in \mathbb{V}_h \setminus \{0\}} \frac{b_h(v, w)}{\|w\|_{\mathcal{V}}} \qquad \forall v \in \mathbb{V}_h.$$

### 3.2.2 Backward Euler time discretisation

We first consider the Backward Euler method (BDF1) for time marching and implement the second-order Backward differentiation formula (BDF2) in Section 3.2.3. Herein, the $\lesssim$ symbol denotes less or equal to a mesh-independent constant. We define $\tau := T/N$ as the time step, where $T$ is the final time, and $N$ is a positive integer. We set $\tau \leq \min(T, \tau_c)$. We use the following first-order approximation of the time derivative:

$$\delta_t^{(1)} v^{n+1} := \frac{v^{n+1} - v^n}{\tau} \in V \quad \forall n \in 0, \dots N. \tag{3.11}$$

Thus, the fully discrete problem becomes: for $n = 0, \cdots, n-1$, find $\theta^{n+1} \in \mathbb{V}_h$, such that

$$(v^{n+1}, \delta_t^{(1)} \theta^{n+1})_0 + (v^{n+1}, B_h \theta^{n+1})_0 = (v^{n+1}, \ell_h^{n+1})_0 \quad \forall v^{n+1} \in \mathbb{V}_h, \tag{3.12}$$

where $\theta^0 = \pi_h u_0$ and $\ell_h^{n+1}$ denotes the discrete linear form on $\mathbb{V}_h^*$ (2.10) at time $n+1$. We define the discrete-in-time operator $B_{h,\tau} : \mathbb{V}_{*h} \to \mathbb{V}_h$, such that, for all $(w, u) \in \mathbb{V}_h \times \mathbb{V}_h^*$,

$$(w, B_{h,\tau} u) = b_{h,\tau}(w, u) := (w, u)_0 + \tau b_h(w, u). \tag{3.13}$$

Thus, we rewrite problem (3.12) in terms of the new operator $B_{h,\tau}$ as:

$$\begin{cases} \text{Given } \theta^n, \text{find } \theta^{n+1} \in \mathbb{V}_h \text{ such that:} \\ (v, B_{h,\tau} \theta^{n+1}) = (v, l_h^{\mathrm{dG}})_0 \quad \forall v \in \mathbb{V}_h, \end{cases} \tag{3.14}$$

with

$$l_h^{\mathrm{dG}} := \theta^n + \tau \ell_h^{n+1}. \tag{3.15}$$

We endow $\mathbb{V}_h$ with the time-step dependent norm and its extension, respectively:

$$\|w\|_{\tilde{\tau}}^2 := \|w\|_0^2 + \tau \|w\|_{\tilde{\mathcal{V}}}^2; \quad \|w\|_{\tilde{\tau},*}^2 := \|w\|_0^2 + \tau \|w\|_{\tilde{\mathcal{V}},*}^2 \tag{3.16}$$

and

$$\|w\|_{\tau}^2 := \|w\|_0^2 + \tau \|w\|_{\mathcal{V}}^2; \quad \|w\|_{\tau,*}^2 := \|w\|_0^2 + \tau \|w\|_{\mathcal{V},*}^2. \tag{3.17}$$

We establish discrete coercivity and boundedness of $B_{h,\tau}$ in terms of norms $\|w\|_{\tilde{\tau}}^2$ and $\|w\|_{\tilde{\tau},*}^2$ through the following lemma:

**Lemma 2.** *The operator $B_{h,\tau}$ satisfies the following by discrete coercivity:*

1. *Discrete coercivity:*

$$(v, B_{h,\tau} v) \gtrsim \|v\|_{\tilde{\tau}}^2, \qquad \forall v \in \mathbb{V}_h. \tag{3.18}$$

2. *Boundedness:*

$$(v, B_{h,\tau}(u - \pi_h u)) \lesssim \|v\|_{\tilde{\tau}} \|u - \pi_h u\|_{\tilde{\tau},*}, \qquad \forall (v, u) \in \mathbb{V}_h \times \mathbb{V}_{*h}. \tag{3.19}$$

*Proof.* Proof can be found in appendix A.1. □

In a strong advection regime, we find a better constant based on inf-sup stability in terms of norms $\|w\|_{\tau}^2$ and $\|w\|_{\tau,*}^2$ through the following lemma:

**Lemma 3.** *The operator $B_{h,\tau}$ satisfies the following by the inf-sup condition:*

1. *Discrete inf-sup stability: There is a constant $C_{st} > 0$, such that*

$$C_{st} \|v\|_{\tau} \leq \sup_{w \in \mathbb{V}_h \setminus \{0\}} \frac{b_{h,\tau}(v, w)}{\|w\|_{\tau}}, \quad \forall \ v \in \mathbb{V}_h. \tag{3.20}$$

2. *Boundedness: There is a constant $C_{bd} < \infty$, such that*

$$(v, B_{h,\tau} u) \leq C_{bd} \|v\|_{\tau} \|u\|_{\tau,*}, \qquad \forall (v, u) \in \mathbb{V}_h \times \mathbb{V}_{*h}. \tag{3.21}$$

*Proof.* Proof can be found in appendix A.2. □

### 3.2.3 Second-Order Backward Differencing Formula

As above, we use the second-order backward differencing formula as a time marching method to obtain a fully discrete solution,

$$\delta_t^{(2)} v^{n+1} := \frac{3v^{n+1} - 4v^n + v^{n-1}}{2\tau} \in V \quad \forall n \in 1, \dots N. \tag{3.22}$$

For $n = 1, \cdots, k-1$,find $\theta^{n+1} \in \mathbb{V}_h$, such that

$$(v^{n+1}, \delta_t^{(2)} \theta^{n+1})_0 + (v^{n+1}, B_h \theta^{n+1})_0 = (v^{n+1}, \ell_h^{n+1})_0 \quad \forall v^{n+1} \in \mathbb{V}_h, \tag{3.23}$$

for this case, we redefine the discrete-in-time operator $B_{h,\tau}$, as well as the bilinear form $b_{h,\tau}$ as: $B_{h,\tau} : \mathbb{V}_{*h} \to \mathbb{V}_h$, such that, for all $(w, u) \in \mathbb{V}_h \times \mathbb{V}_h^*$,

$$(w, B_{h,\tau} u) = b_{h,\tau}(w, u) := (w, u)_0 + \tfrac{3}{2}\tau b_h(w, u). \tag{3.24}$$

We now write problem (3.23) following the derivation of (3.14) with

$$l_h^{\mathrm{dG}} := \tfrac{2}{3}\tau \ell_h^{n+1} + \tfrac{4}{3}\theta^n - \tfrac{1}{3}\theta^{n-1} \tag{3.25}$$

and a given initial condition $\theta^0 = \pi_h u_0$. We compute $\theta^1$, if necessary, with a first-order method. This operator satisfies the stability properties described in Section 3.2.2. Thus, updating (3.14) with the definitions (3.24) and (3.25), the operator $B_{h,\tau}$ is well-posed.

**Remark 2** (Relation with other time marching schemes.)**.** *This analysis can be extended to encompass the one-parameter family of second-order time-marching schemes defined by the generalised-$\alpha$ methods [Jansen et al., 2000; Behnoudfar et al., 2020a] and other higher-order counterparts [Behnoudfar et al., 2020b, 2022]. In particular, BDF2 corresponds to the generalised-$\alpha$ method with $\rho_\infty = 0$.*

## 3.3 Fully Discrete Residual minimisation

We extend the method devised in Section 2.2 to address unsteady problems using the residual minimisation on dual discontinuous Galerkin norms to deliver a stabilised discrete solution within a continuous space by minimising the residual using a dual discontinuous norm at each time step. Thus, we choose $\mathbb{V}_h$ as a broken polynomial space described in (2.3) and $\bar{\mathbb{V}}_h$ as its $H^1$-conforming subspace.

Following the formulation (3.14) in $\mathbb{V}_h$, we chose a trial conforming subspace $\bar{\mathbb{V}}_h \subset \mathbb{V}_h$ to solve the following residual minimisation problem:

$$\begin{cases} \text{Given } u^n \text{ , find } \bar{u}^{n+1} \in \bar{\mathbb{V}}_h \subset \mathbb{V}_h, \text{ such that:} \\ \quad \bar{u}^{n+1} = \arg\min\limits_{z \in \bar{\mathbb{V}}_h} \dfrac{1}{2} \| l_h - B_{h,\tau} z \|^2_{\tau,*} \\ \quad\quad\quad = \arg\min\limits_{z \in \bar{\mathbb{V}}_h} \dfrac{1}{2} \| R_\tau^{-1} (l_h - B_{h,\tau} z) \|^2_{\tau}, \end{cases} \tag{3.26}$$

where $u^0 = \pi_h u_0$ and $l_h$ is defined as $l_h := \bar{u}^n + \tau \ell_h^{n+1}$ for BDF1 and $l_h := \frac{2}{3}\tau \ell_h^{n+1} + \frac{4}{3}\bar{u}^n - \frac{1}{3}\bar{u}^{n-1}$ for BDF2. $R_\tau^{-1}$ denotes the inverse of the Riesz map:

$$\begin{aligned} R_\tau : \quad & \mathbb{V}_h \to \mathbb{V}_h^* \\ & (v, R_\tau \cdot)_{\mathbb{V}_h \times \mathbb{V}_h^*} := g_\tau(v, \cdot) \quad \forall v \in \mathbb{V}_h. \end{aligned} \tag{3.27}$$

Problem (3.26) is equivalent to this saddle-point problem at every time step:

$$\begin{cases} \text{Given } u^n, \text{ find } (\varepsilon^{n+1}, \bar{u}^{n+1}) \in \mathbb{V}_h \times \bar{\mathbb{V}}_h, \text{ such that:} \\ g_\tau(v, \varepsilon^{n+1}) + (v, B_{h,\tau} \bar{u}^{n+1}) = (v, l_h)_0 \qquad \forall v \in \mathbb{V}_h, \\ (\bar{z}, B_{h,\tau} \varepsilon^{n+1}) = 0, \qquad \forall \bar{z} \in \bar{\mathbb{V}}_h, \end{cases} \tag{3.28}$$

where the residual representation function $\varepsilon^{n+1}$ is:

$$\varepsilon^{n+1} := R_\tau^{-1}(l_h - B_{h,\tau}) \in \mathbb{V}_h. \tag{3.29}$$

We write (3.28) in the dual space,

$$\begin{cases} \text{Given } u^n, \text{ find } (\varepsilon^{n+1}, \bar{u}^{n+1}) \in \mathbb{V} \times \bar{\mathbb{V}}_h, \text{ such that:} \\ R_\tau \varepsilon^{n+1} + B_{h,\tau} \bar{u}^{n+1} = l_h, \text{ in } \mathbb{V}_h^*, \\ B_{h,\tau} \varepsilon_h^{n+1} = 0, \text{ in } \bar{\mathbb{V}}_h^*. \end{cases} \tag{3.30}$$

**Remark 3.** *Substituting the source term ($\ell_h^{n+1}$) from (3.14) into the first identity in (3.30), we obtain, for BDF1, that:*

$$R_\tau \varepsilon^{n+1} + B_{h,\tau} u^{n+1} = u^n + B_{h,\tau} \theta^{n+1} - \theta^n. \tag{3.31}$$

*Rearranging and defining the spatial error at time step $n$ by $\xi^n := \theta^n - u^n$;*

*then,* (3.31) *implies that:*

$$\varepsilon^{n+1} = R_\tau^{-1}(B_{h,\tau}\xi^{n+1} - \xi^n). \tag{3.32}$$

*Or, equivalently, for the BDF2 implementation:*

$$\varepsilon^{n+1} = R_\tau^{-1}(B_{h,\tau}\xi^{n+1} - \tfrac{4}{3}\xi^n + \tfrac{1}{3}\xi^{n-1}).$$

*Hence, we can alternatively define* $\varepsilon^{n+1}$ *as an error measure distance from the continuous to discontinuous approximation at the* $n+1$ *time step with the* $k$ *previous time-step spatial error contributions (for a* $k$*-order BDF method).*

## 3.4 Variational multiscale reconstruction

Within the scope of discussion presented in Section 2.3, we extend the VMS interpretation by focusing on the recovery of both the VMS fine-scale solution and the adjoint multiscale reconstruction. We define the full-scale reconstruction at each time step by using a direct sum decomposition, i.e., $u^{n+1} = \bar{u}^{n+1} + \tilde{u}^{n+1}$, where $\bar{u}^{n+1}$ and $\tilde{u}^{n+1}$ are the coarse- and fine-scale solutions, respectively. The fine-scale solution satisfies the following problem at each refinement level:

$$\begin{cases} \text{Given } \varepsilon^{n+1}, \text{ find } \tilde{u}^{n+1} \in \mathbb{V}_h, \text{ such that:} \\ b_{h,\tau}(v, \tilde{u}^{n+1}) \;=\; g_\tau(v, \varepsilon^{n+1}) \qquad \forall v \in \mathbb{V}_h. \end{cases} \tag{3.33}$$

Similarly, we propose a heuristic fine-scale reconstruction, $\check{u} \in \mathbb{V}'_h$, that satisfies the following residual-driven problem:

$$\begin{cases} \text{Given } \varepsilon^{n+1}, \text{ find } \check{u}^{n+1} \in \mathbb{V}'_h, \text{ such that:} \\ b_{h,\tau}(v, \check{u}^{n+1}) \;=\; g_\tau(v, \varepsilon^{n+1}) + b_{h,\tau}(\varepsilon^{n+1}, v) \qquad \forall v \in \mathbb{V}_h. \end{cases} \tag{3.34}$$

The heuristic adjoint variational multiscale reconstruction at each time state as

$$\phi^{n+1} = \bar{u}^{n+1} + \check{u}^{n+1}.$$

**Remark 4.** *Since both the full-scale and the adjoint multiscale reconstructions belong to the* $\mathbb{V}_h$ *space, we can use either of them as a better initial estimation* $u^n$ *in the saddle problem* (3.28) *for each iteration. This approach works as an*

*improved dG-projection for the original continuous formulation.*

## 3.5 Numerical examples

We present four numerical examples to demonstrate the performance properties of our adaptive stabilised finite element method in handling unsteady problems. First, we solve the heat equation, obtaining optimal space and time convergence for uniform refinements. Next, we use the classic Eriksson-Johnson problem to test the adaptive refinement strategy and its convergence in space for different polynomial degrees and Péclet numbers. Besides, we show the improvement of the post-processing VMS reconstruction. Finally, we test the stability in two dimensions for the unsteady pure-advection problem where the mesh evolves in time. Here, we compare the computational time of the stabilised finite element method using adaptivity for a uniform mesh with the dG method. Since we minimise the residual in the energy norm ($\tau$), we focus on the spatial convergence in this norm. We implement the iterative algorithm described in Bank et al. [1989]; Calo et al. [2020b] to solve the resulting saddle point system (3.30).

### 3.5.1 Heat equation (2D)

We study the method's performance by solving the 2D heat equation while refining the spatial domain uniformly. Although this case does not challenge classical methods, it is a standard benchmark problem to test space and time convergences of parabolic problems. Let the domain $\Omega$ be $[0,1]^2$; we consider the problem:

$$\begin{aligned} \partial_t u - \Delta u &= f \quad \text{in } \Omega \times (0,T], \\ u &= 0 \quad \text{on } \Gamma_D \times (0,T], \\ u(\cdot\,, t=0) &= u_0 \quad \text{in } \Omega, \end{aligned} \tag{3.35}$$

with the initial condition:

$$u_0 = \sin(\pi x)\sin(\pi y),$$

and the source term $f$ that satisfies the exact solution:

$$u((x,y),t) = \exp(-\pi^2 t)\sin(\pi x)\sin(\pi y).$$

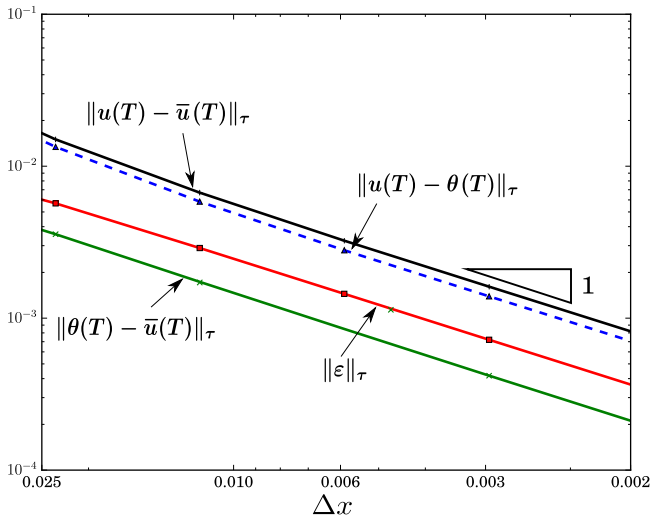


**Figure 3.1:** BDF1 spatial convergence using fixed time step and uniform meshes.

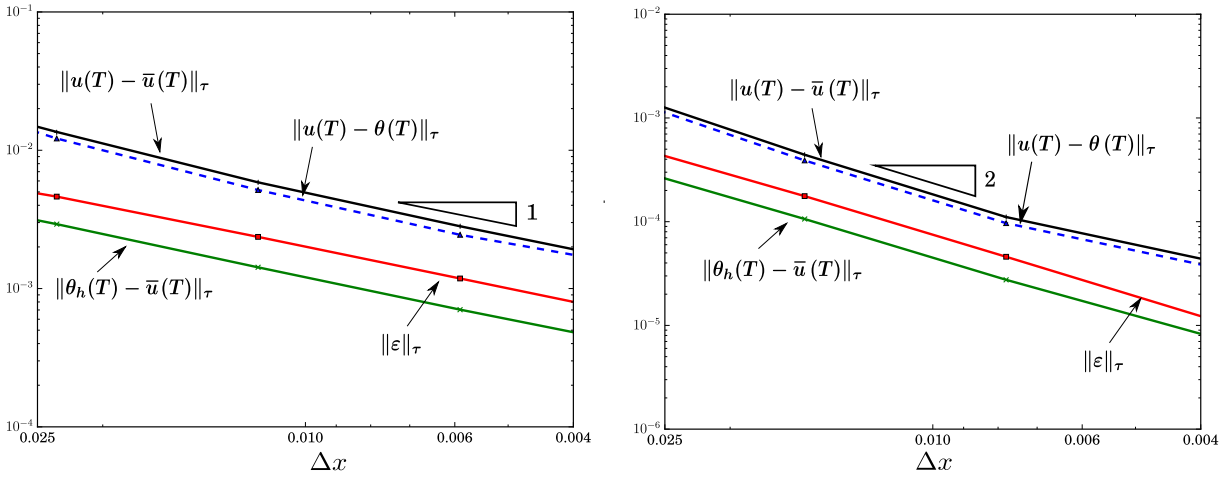


a) $T = 0.1, \tau = 0.001, p = 1$ b) $T = 1, \tau = 0.001, p = 2$

**Figure 3.2:** BDF2 spatial convergence using fixed time step and uniform meshes

We obtain the fully discrete problem by combining the SIP bilinear form (for $\kappa = 1$) with the BDF1/BDF2 time marching schemes. We show the convergence of linear and quadratic polynomials in space (Figures 3.1 and 3.2) and time (Figure 3.3). We analyse the spatial convergence by computing the errors $\|u - \bar{u}\|_\tau$ (in black), $\|u - \theta\|_\tau$ (in blue), $\|\theta - \bar{u}\|_\tau$ (in green) and $\|\varepsilon\|_\tau$ (in red) for different mesh sizes ($\Delta x$). We denote $\Delta x$ equal to $h_K$ for uniform meshes. We study the temporal convergence by studying how $\|u - \bar{u}\|_0$ varies with the time step size $\tau$ for $\Delta x = 0.01$. As a result, we recover space optimality for the continuous approximation (from dG formulation) and the first- and second-order time convergence for BDF1 and BDF2, respectively. We show that

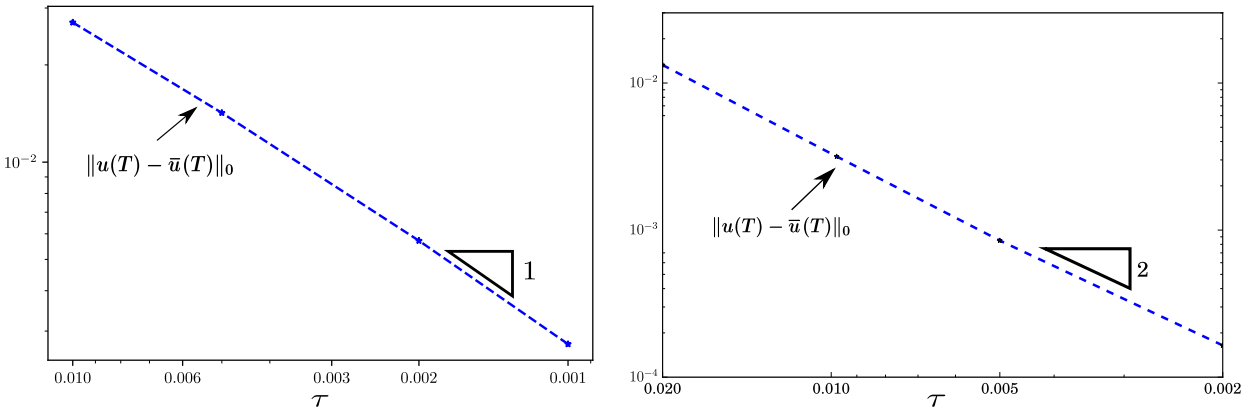


a) $T = 0.1, \Delta x = 0.01, p = 1$ b)$T = 1, \Delta x = 0.01, p = 2$

**Figure 3.3:** Time convergence for backward Euler (BDF1) and BDF2 for a fixed mesh.

the saturation assumption in Calo et al. [2020b] holds in our formulation (i.e., $\|u(T) - \theta(T)\|_\tau \lesssim \|u(T) - \bar{u}(T)\|_\tau$) and the residual representation is efficient until the error dominates (i.e., $\|\varepsilon\|_\tau \lesssim \|u(T) - \bar{u}(T)\|_\tau$ in Calo et al. [2020b]). Figure 3.2b shows that for $p = 2$ and a large number of degrees of freedom, the temporal error is no longer negligible with respect to the spatial error; however, the error estimator continues decaying as it does not appropriately consider the temporal error contribution.

### 3.5.2 Advection-diffusion problem

We complement the spatial convergence study of the previous example, using adaptive refinement for the unsteady advection-dominated Eriksson-Johnson problem. Let the domain $\Omega$ be $[0, 1] \times [-0.5, 0.5]$; we consider the exact solution

$$u((x, y), t) = \exp(-lt)[\exp(\lambda_1 x) - \exp(\lambda_2 x)] + cos(\pi y)\frac{\exp(s_1 x) - \exp(r_1 x)}{\exp(-s1) - \exp(-r_1)},$$

for $f = 0$ and $l = 2$, $\lambda_{1,2} = \frac{-1 \pm \sqrt{1-4\kappa l}}{-2\kappa}$, $r_1 = \frac{1+\sqrt{1+4\kappa^2\pi^2}}{2\kappa}$ and $s_1 = \frac{1-\sqrt{1+4\kappa^2\pi^2}}{2\kappa}$. Here, we set $\beta = [1, 0]$ and $\mu = 0$ for different diffusion coefficient values. Based on the exact solution, we apply Neumann boundary conditions at $x = -1$ and $t = 0$; meanwhile, we impose Dirichlet boundary conditions at $x = 0$, $y = -0.5$ and $y = 0.5$ at time $t = 0$.

The problem's main challenge is capturing the boundary layer, especially for high Péclet numbers. Figure 3.4 shows how the error estimator drives spatial adaptivity to smooth the regions with sharp gradients in each time step. Fig-

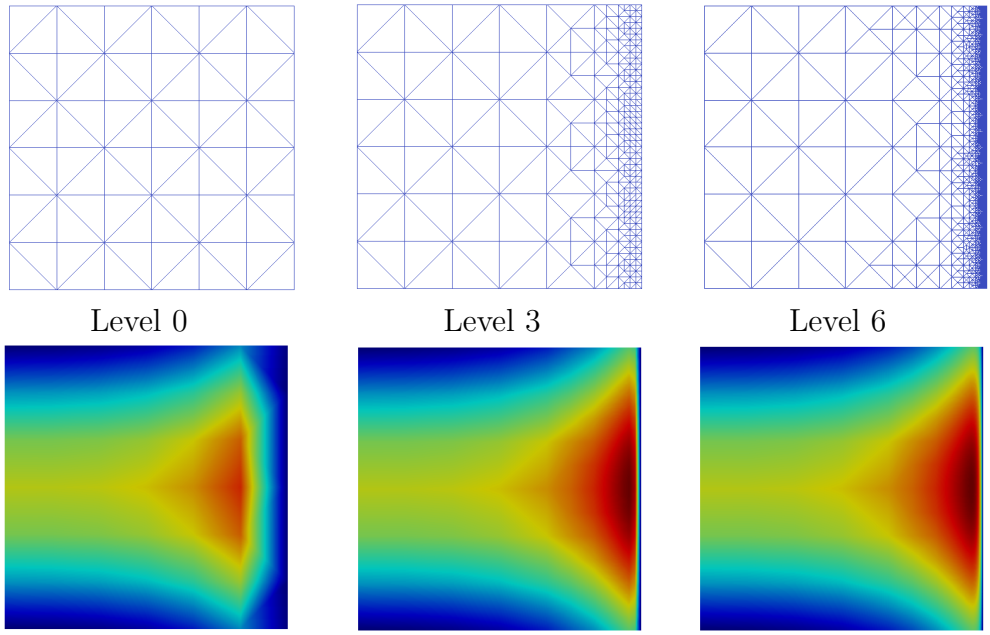


**Figure 3.4:** Mesh refinement $\tau = 0.005$, $T = 0.1, p = 1$.

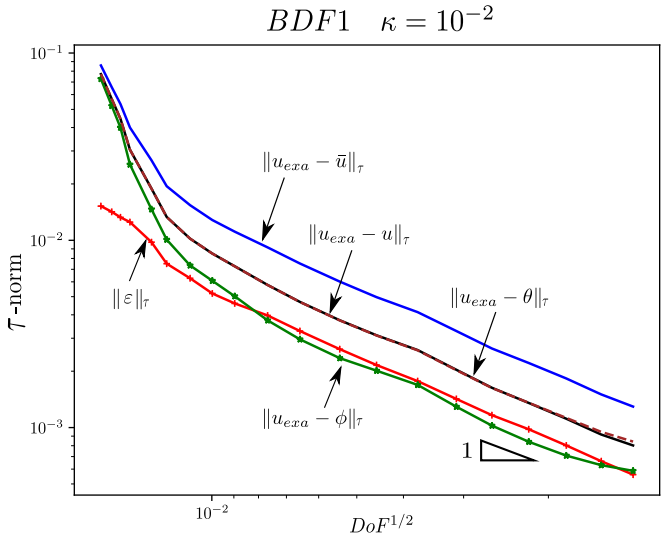


**Figure 3.5:** Spatial convergence for adaptive refinement (BDF1 : $\kappa = 10^{-2}$,$T = 0.1$, $\tau = 0.005$)

.

ures 3.5 and 3.6 present the decay rate in the energy norm ($\tau$) for the errors $|u_{exa} - \bar{u}|\tau$, $|u_{exa} - \theta|\tau$, $|u_{exa} - u|\tau$, $|u_{exa} - \phi|\tau$, and $|\varepsilon_h|\tau$, as a function of the square root of the total degrees of freedom ($DoF^{1/2}$). We show optimal spatial convergence achieved using BDF1 and BDF2 time integrators for linear and quadratic polynomial trial functions at $T = 0.1$ and $\tau = 0.005$, even when the diffusion coefficients vary. We verify that the fine-scale contribution $\tilde{u}$ recovers the

dG approximation $\theta$ (i.e., $u \approx \theta$ ). Besides, we show that the adjoint multiscale reconstruction ($\phi$) improves the approximation compared to the full-scale ($u$) and the dG ($\theta$) solutions regardless of the polynomial degree and the time integrator order (i.e BDF1 and BDF2). Figure 3.7 shows the evolution of our transient solution to the analytical steady-state Eriksson-Johnson problem. As for the uniform refinement case, we preserve the efficiency of the residual representative and the saturation assumptions for the adaptive steady-state case.

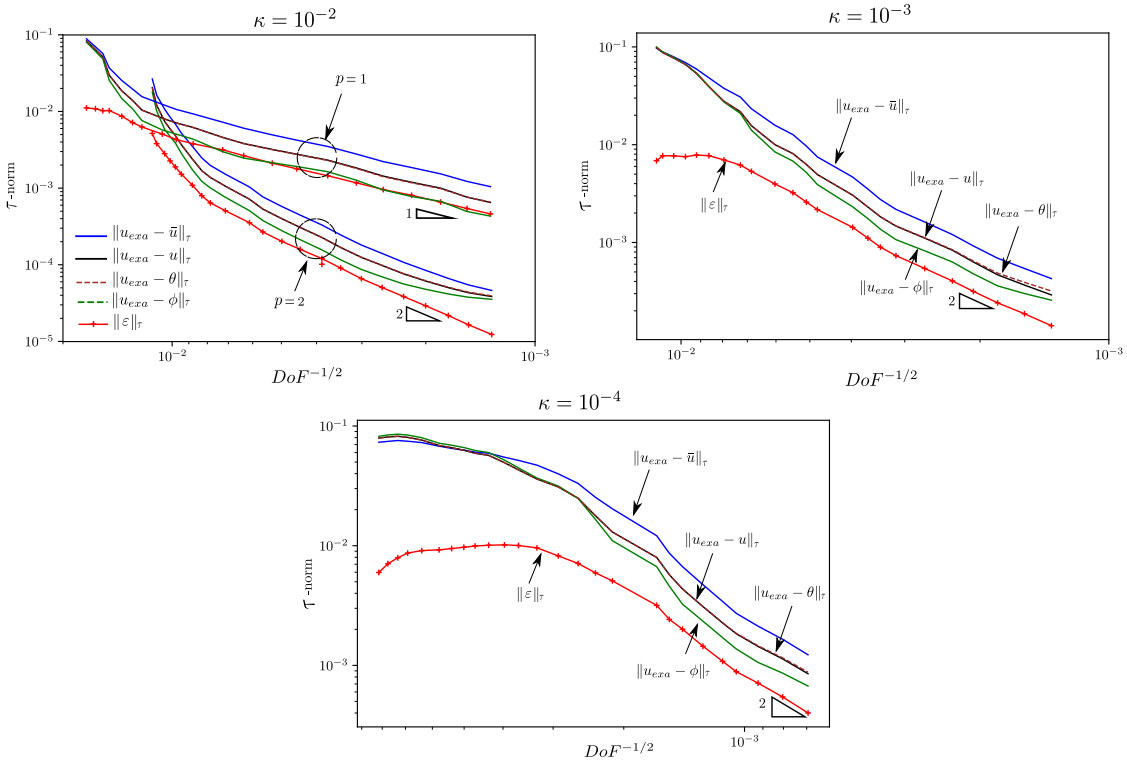


**Figure 3.6:** Energy norm convergence in space ($\tau$) for adaptive refinement (BDF2: $T = 0.1$, $\tau = 0.005$). Left: $\kappa = 10^{-2}$ for p=1,2. Right: $\kappa = 10^{-3}$ for p=2. Bottom: $\kappa = 10^{-4}$ for p=2

.

### 3.5.3 Rotating flow transporting a Gaussian profile

In this example, we analyse the performance of our method in a convective transport problem with a localised disturbance; we test the adaptive algorithm when the region of interest moves within the domain as time passes. Our algorithm evolves the mesh using residual estimates without prior knowledge of the solution

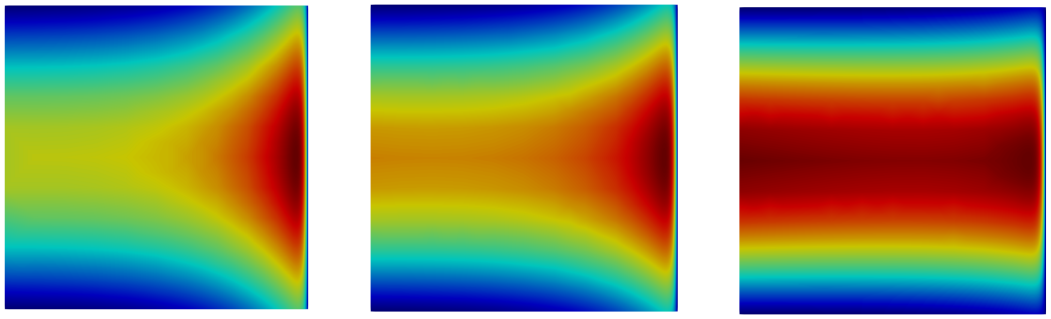


**Figure 3.7:** Solution convergence to the steady Eriksson–Johnson solution.

evolution profile. We study the solution of a 2D convection-diffusion transport by a rotating flow of a Gaussian profile. We set $\Omega = [-2, 2]^2$, $T = \pi$, $\beta = [y, -x]$, $\kappa = 10^{-5}$, $\mu = 0$ and $f = 0$, where the initial condition is

$$u_0 = \exp(-64(x - 0.5)^2) \exp(-64y^2).$$

We impose Dirichlet boundary conditions from the exact solution:

$$u((x, y), t) = \frac{1}{1 + 256\kappa t} \exp\left(-\frac{64(x - 0.5\cos(t))^2}{1 + 256\kappa t}\right) \exp\left(-\frac{64(y + 0.5\sin(t))^2}{1 + 256\kappa t}\right).$$

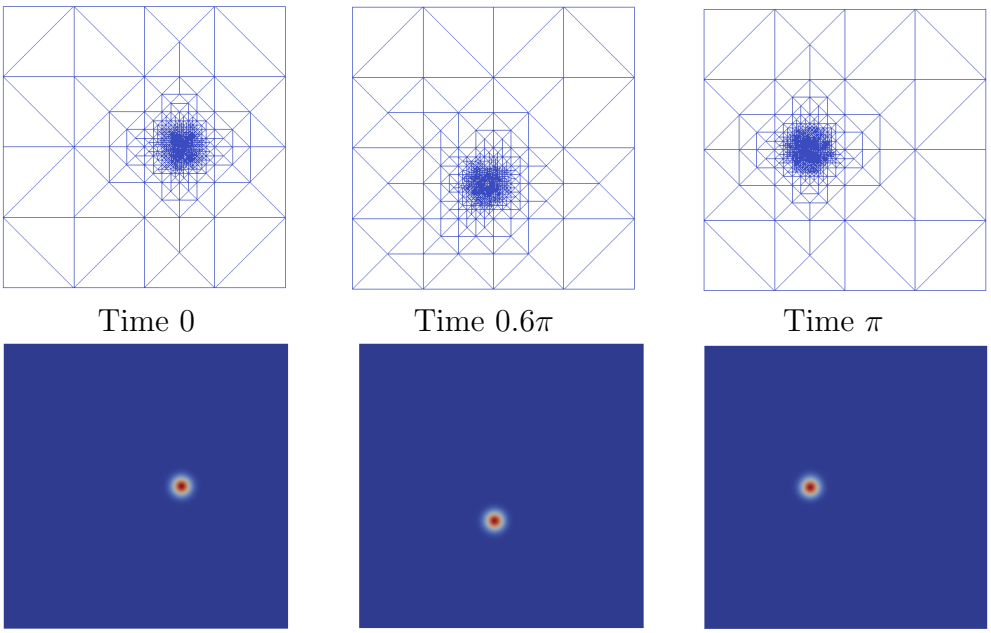


**Figure 3.8:** Time evolution $p = 1$ ($T = \pi, \tau = \pi/512$).

Figure 3.8 shows the profiles of the solutions and the corresponding adaptively refined meshes at different time steps, which demonstrate the continuous solution stability and consistency with the physical phenomena, even for low diffusivities. Moreover, the mesh refinement concentrates where the solution varies largely, showing the robustness of the error estimator and the efficiency of the marking strategy when adding new degrees of freedom. Regarding computational cost, our stabilised finite element formulation using adaptivity is competitive with the dG methodology using uniform refinement. Solving the saddle point formulation requires an extra cost due to the additional degrees of freedom. However, adaptivity compensates for the excess due to the solution's stability in coarse meshes and the robustness of the error estimator. Figure 3.9 shows a comparison between the total computational cost to solve with the adaptive stabilised method (blue line) and the computational cost using a regular mesh in the dG method (red line). Besides, the figure shows that the adaptivity can reduce the computational cost by up to one order of magnitude to get a resolution of 1e-5 in the energy norm.

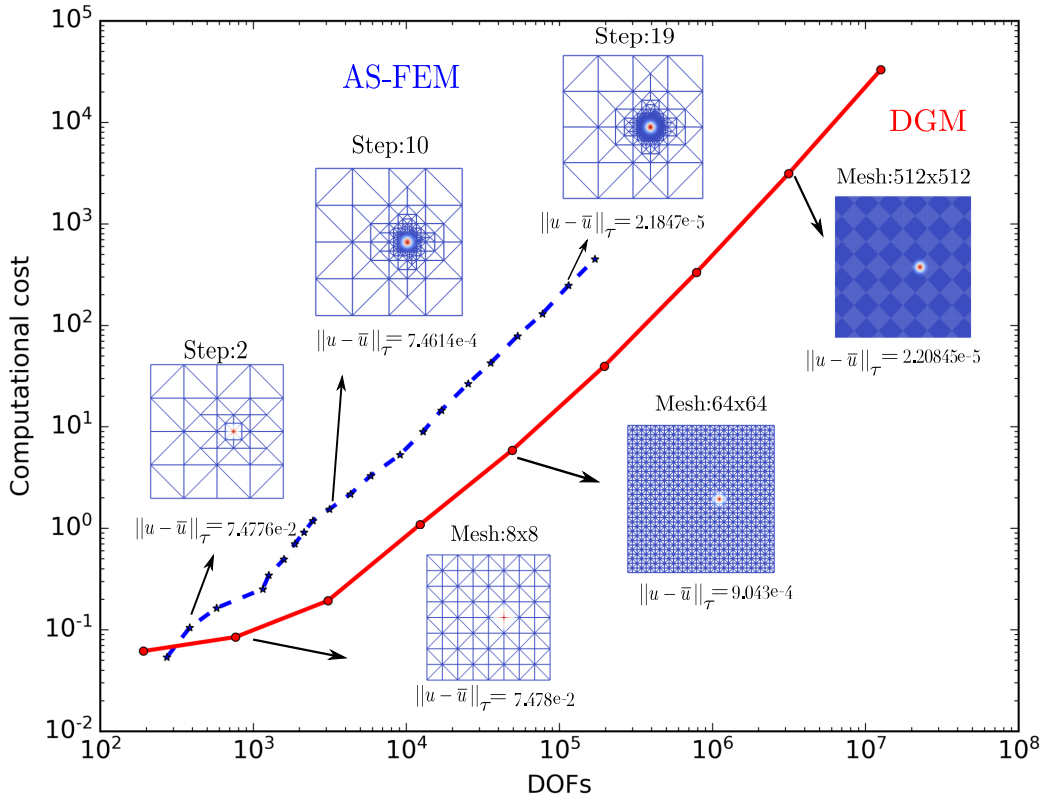


**Figure 3.9:** Computational cost [s] vs total degrees of freedom.

## 3.6 Unsteady nonlinear systems

We evaluate the method's performance by examining the solution of a nonlinear diffusion-reaction equation. Consider the domain $\Omega = [0,1]^2$ and let $\lambda$ be a positive real constant. We solve the unsteady Bratu problem that reads:

$$\begin{cases} \text{Find } u \text{ such that, for } T > 0, \\ \partial_t u = \Delta u + \lambda \exp(u) \quad \text{in } \Omega \ \times (0,T], \\ u = 0 \quad \text{on } \Gamma \ \times (0,T], \\ u(\cdot, t=0) = u_0(x) \quad \text{in } \Omega, \end{cases} \tag{3.36}$$

The 2D steady version of (3.36) has a branched solution for $\lambda < \lambda_c$ (lower and upper branches) and a unique solution at the critical point ($\lambda_c \approx 6.8081$). The lack of stable solutions in the upper branch and close to the critical point $\lambda_c$ make the problem challenging, leading to classical techniques converging only to the stable lower branch. We test our method's robustness, accuracy and performance in this transient bifurcation problem; we compare the solutions obtained in (3.36) when $t \to \infty$, with the 2D steady Bratu's approach obtained in Cier et al. [2021b]. We formulate the space semi-discretisation of (3.36) as follows:

$$\begin{cases} \text{Find } \theta \in \mathbb{V}_h, \text{ such that:} \\ (v, \partial_t \theta)_0 + \eta_h(v;\theta) = \ell_h(v), \quad \forall v \in \mathbb{V}_h, \end{cases} \tag{3.37}$$

where $\eta_h(v;u)$ denotes the nonlinear form, including the SWIP formulation in (2.7) with a non-linear reactive contribution. We define it as:

$$\begin{aligned} \eta_h(v;u) := & \sum_{K\in\mathfrak{T}} (\nabla v, \nabla u)_K - \sum_{K\in\mathscr{T}_h} (v, \lambda \exp(u))_K \\ & - \sum_{F\in\mathscr{F}_h^\partial} \Big( (\llbracket v \rrbracket, \{\nabla u\}\cdot \mathbf{n}_F)_F + (\{\nabla v\}\cdot \mathbf{n}_F, \llbracket u_h \rrbracket)_F - n_e \kappa (\llbracket v \rrbracket, \llbracket u \rrbracket)_F \Big). \end{aligned} \tag{3.38}$$

For BDF1 time marching, we define the discrete-time nonlinear form as:

$$\eta_{h,\tau}(v;u) \ := \ (v,u)_K + \tau \eta_h(v;u). \tag{3.39}$$

Thus, the full-discrete formulation for problem (3.36) is:

$$\begin{cases} \text{Given } \theta^n, \text{find } \theta^{n+1} \in \mathbb{V}_h \text{ such that:} \\ \eta_{h,\tau}(v;\theta^{n+1}) = (v, l_h^{\mathrm{dG}})_0 \qquad \forall v \in \mathbb{V}_h, \end{cases} \tag{3.40}$$

with $l_h^{\mathrm{dG}} := \theta^n + \tau \ell_h^{n+1}$. We use a Newton–Raphson iteration scheme combined with the residual minimisation strategy described in Section 3.3 to solve (3.40). We seek a solution at every Newton step increment $w$ for each time step $n+1$ by using the linearised form:

$$\begin{aligned} \eta'_{h,\tau}(v,w;u) := (v,w)_K + \tau\Big( \sum_{K\in\mathfrak{T}} (\nabla v, \nabla w)_K - \sum_{K\in\mathscr{S}_h} (v, \lambda \exp(u) w)_K \\ - \sum_{F\in\mathscr{S}_h} \Big( (\llbracket v \rrbracket, \{\nabla w\}\cdot \mathbf{n}_F)_F + (\{\nabla v\}\cdot \mathbf{n}_F, \llbracket w \rrbracket)_F - n_e \kappa (\llbracket v \rrbracket, \llbracket w \rrbracket)_F \Big) \Big). \end{aligned} \tag{3.41}$$

Since (3.41) takes the form of a diffusion-reaction problem, we use a time-step dependent norm (3.17), with the SWIP contribution to the $\mathbb{V}_h-$norm, to minimise the discrete residual of the linearised system. The norm $\|\cdot\|_\tau$ is enforced with an $L_2$ contribution to measure the nonlinear reactive term. Starting with an initial guess $(\varepsilon_0^{n+1}, u_0^{n+1})$ and given $(\varepsilon_i^{n+1}, \bar{u}_i^{n+1})$, we find:

$$\begin{cases} (\delta\varepsilon^{n+1}, \delta\bar{u}^{n+1}) \in \mathbb{V}_h \times \bar{\mathbb{V}}_h, \text{ such that: } \forall (v,\bar{z}) \in \mathbb{V}_h, \times \bar{\mathbb{V}}_h, \\ g_\tau(v, \delta\varepsilon^{n+1}) + \eta'_\tau(v, \delta\bar{u}^{n+1}; \bar{u}_i^{n+1}) = (v, l_h)_0 - g_\tau(v, \varepsilon_i^{n+1}) - \eta_\tau(v; \bar{u}_i^{n+1}), \\ \eta'_\tau(\delta\varepsilon^{n+1}, \bar{z}; \bar{u}_i^{n+1}) = -\eta'_\tau(\varepsilon_i^{n+1}, \bar{z}; \bar{u}_i^{n+1}). \end{cases} \tag{3.42}$$

$\bar{u}_i^{n+1}$ and $\varepsilon_i^{n+1}$ are updated at every $i$-th increment as follows:

$$\bar{u}_{i+1}^{n+1} = \bar{u}_i^{n+1} + k\delta\bar{u}^{n+1}, \qquad \varepsilon_{i+1}^{n+1} = \varepsilon_i^{n+1} + k\delta\varepsilon^{n+1},$$

where $k$ denotes a relaxation parameter from the Damped Newton's method [Bank & Rose, 1981], and it is detailed to our formulation's context in Cier et al. [2021b]. For the time step $n = 1$, we set the initial guess $(\varepsilon_0^{n+1}, \bar{u}_0^{n+1}) = (0, u_{\mathrm{IG}})$, where $u_{\mathrm{IG}}$ varies depending on the solution branch we want to capture. Here, we assume $u_{\mathrm{IG}}$ equal to the initial solution (i.e., $u_{\mathrm{IG}} = u_0$) with $u_0 = 0$ for the stable lower branch and $u_0 = u_{\mathrm{up}}$ for the upper branch. Since the lower branch is stable, many different initial guesses converge to it; however,

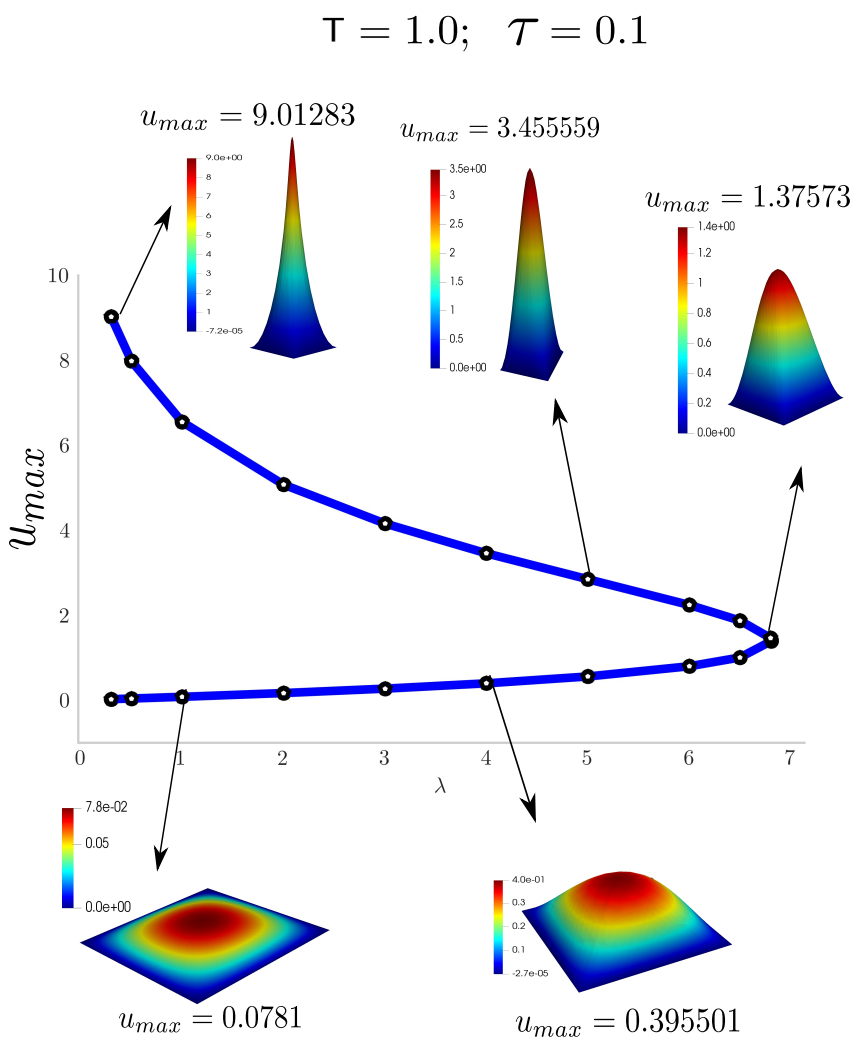


**Figure 3.10:** Bratu's bifurcation diagram for T=1.0 and $\tau$=0.1.

we only use one option. The unstable upper branch is more restrictive; therefore, we follow Hajipour et al. [2018] and use:

$$u_{\text{up}}(x, y) = \frac{50(2+\lambda)}{\lambda}(x - x^2)(y - y^2).$$

Figures 3.10 and 3.11 display the two branch solutions we obtain with a time step increment of $\tau = 0.1$, an initial mesh consisting of 4x4 elements, and a final time of $T = 1.0$. Figure 3.11 illustrates a time sequence for both lower and upper solutions, ranging from $t = 0$ to $t = T$, at $\lambda = 2$. Figure 3.10 presents the classic bifurcation diagram for Bratu's problem by evaluating the maximum value $u_{\max}$

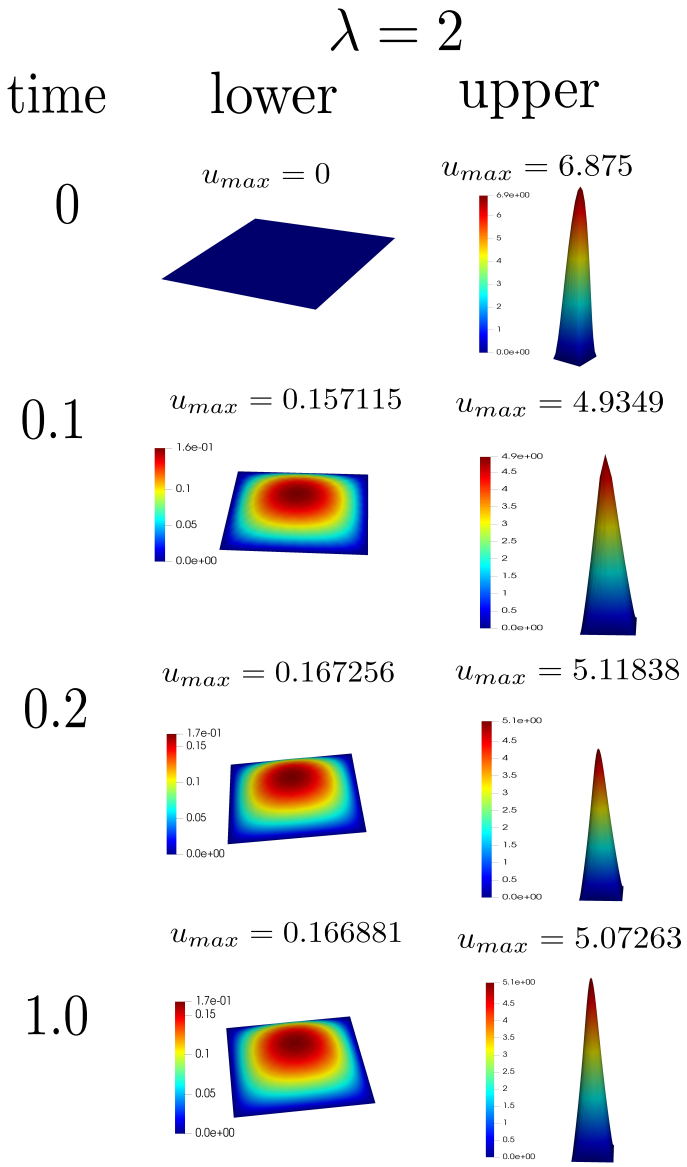


**Figure 3.11:** Solution's temporal evolution for $\lambda = 2$ for the lower and upper branches.

at time $T$ for various $\lambda$ values, ranging from 0 to $\lambda_c$. At this point, we ensure a convergent solution over time to approach the problem's steady state. Our approach is robust and delivers an efficient refinement strategy that captures the stable and unstable branches, even near the critical point ($\lambda_c$). We verify the accuracy of the results by successfully comparing our bifurcation map at time $T$ with published steady-state results [Hajipour et al., 2018; Cier et al., 2021b].

Summing up, we propose an adaptive-stabilised finite element method based on residual minimisation for unsteady advection-diffusion-reaction problems us-

ing the method of lines. The method provides a stable solution and a robust error representation to guide adaptivity at every discrete time. The method's performance for challenging linear and nonlinear problems is excellent delivering optimal spatial and temporal convergence by relying on an efficient adaptive refinement strategy to capture sharp inner and boundary layers. The adaptive refinement process reduces the computational cost to solve the saddle-point problem compared to the uniformly refined schemes on discontinuous Galerkin approximation. Next, we implement this framework to tackle the challenging unsteady advection-dominated transport mineralisation described in (1.2).

# Chapter 4

# A paleo stratigraphic model with anisotropic permeability for the genesis of martite-goethite iron-ore deposits

In this chapter, we present a genetic model to explain the mechanisms governing the formation of the BIF supergene Martite-Goethite iron-ore deposits.[1] Following Ockham's razor, the principle of parsimony that states that the preferred explanation for a phenomenon is the one that requires the fewest elements or assumptions. Accordingly, we reduce the supergene enrichment problem to a transport process in a porous medium, controlled by the formation's structure and stratigraphy [Conliffe, 2016], with permeability as the main driving factor. We ensure the reliability of our findings by using the numerical framework we introduced in earlier chapters to solve the equation system. Our model accurately reproduces mineralisation patterns in specific deposits, and we identify the paleo water table level and permeability anisotropy ratio as the primary controlling parameters for mineralisation distribution. Our research raises important questions about the volume of prospective mineralisation estimated previously and provides insights into the physical processes and timing involved in iron enrichment.

[1]The content of this chapter is published in: T. Poulet, J.F. Giraldo, E. Ramanaidou, A. Piechocka, & V.M. Calo [2023] The paleo-stratigraphic permeability anisotropy controls the supergene mimetic martite goethite deposits. *Basin Research*, 35(2):572591.

## 4.1 Permeability anisotropy

Addressing permeability anisotropy is a challenge that demands a thorough understanding of permeability across the entire domain of interest for accurate mineralisation phase modelling, which requires a detailed understanding of the spatial variations in all elements of the permeability tensor while considering factors that affect permeability, such as rock composition, geochemical transformations, and stress conditions. In light of the uncertainties associated with the involved physical processes (see Chapter 1), their timing, and the spatial distribution of material properties, we simplify the modelling approach by concentrating on strata geometry, which we assume to play a critical role in the transport process. Anisotropy within the permeability field is an intrinsic property of rocks, which exhibits a strong correlation with bedding orientation in a basinal setting [Clavaud et al., 2008]. The effects of anisotropy are frequently integrated into the sedimentary basin models for petroleum [Dai et al., 2019] and geothermal [Panja et al., 2021] applications; nevertheless, anisotropy has yet to be utilised in the formation of iron-ore deposits, despite the evident heterogeneity of BIF strata (Figure 1.1).

The permeability tensor in sedimentary basins is usually characterised by its horizontal and vertical components due to compaction, particularly in deeper layers. Conversely, in shallow regions, such as our supergene scenario, the principal directions of the permeability tensor correspond to the stratigraphy in order to capture the depositional history and, indirectly, the structural morphology. Consequently, we delineate the permeability tensor through its longitudinal (parallel to bedding) and transverse (perpendicular to bedding) components, with the orientation of these components (designated as $k_{\parallel}$ and $k_{\perp}$, respectively) following the strata throughout the domain of interest.

We assess our hypothesis in its most elementary form, assuming constant permeability components for each geological unit and ignoring secondary variations from mechanical forces. We constrain the anisotropy ratio, $r = k_{\parallel}/k_{\perp}$ (see Figure 1.1), using field observations [Knight et al., 2018] and a cross section through the Weeli Wolli anticline (Figure 4.1). We interpret the pattern of martite-goethite mineralisation as a direct consequence of the fault displacement. The mineralisation covers the whole thickness of the Marra Mamba iron formation above the fault of interest, but not in the lowest part of that same formation below the fault, as the propagating fluid from above entered the shifted lower segment. This mineralisation pattern suggests that lower fertility in the lower

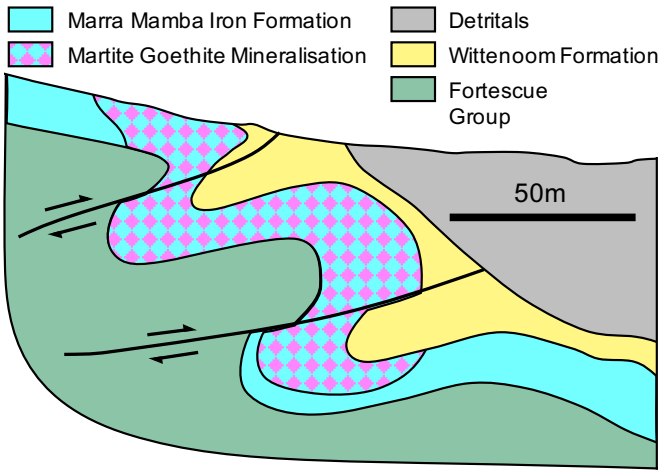


**Figure 4.1:** Simplified detail cross section of the Marra Mamba formation redrawn from [Knight et al., 2018], schematically represented from the original data of [Kepert, 2018]. The mineralisation is covering the whole layer in parts but only some sub-layers in others.

Marra Mamba formation is unlikely to be responsible for the lack of enrichment since that same zone is mineralised above the fault. Instead, the fault displacement prevented fluid access in that lower zone [Perring et al., 2020, Figures 7 to 9]. We interpret the data to imply that the enrichment remained contained in a given sublayer as evidence of high permeability anisotropy ratio $r$.

Following a continuum modelling approach, we describe the relevant material properties as homogenized quantities per geological unit instead of considering the individual contributions of all thinner layers. Since the inhomogeneity of the layers occurs at multiple scales, depending on shale content and distribution for instance, the spatial resolution of the model introduces a notion of length scale threshold which is selected on a case-by-case basis. We ignore a priori the small-scale distribution of thin sedimentary layers responsible for the strong anisotropy as seen in Figure 1.1, until these layers become thick or important enough that we must model them as separate units. (The determination of such a case will be illustrated in Section 4.4.3).

## 4.2 Numerical simulation

Long-term ore mineralisation processes are complex and not well-understood [e.g., Angerer et al., 2014; Perring et al., 2020]. Many questions still exist about the number of fluids involved and their nature, fluid-rock interactions, dissolution-

precipitation reactions, in-situ mineral replacement, and their effects on porosity and permeability evolution. Yet, the permeability anisotropy influences all these aspects; thus, we naturally focus first on this aspect. We then us a single-process model focused on fluid flow patterns' sensitivity to permeability anisotropy.

We reduce the transport problem to its simplest form, assuming necessary conditions for mineralisation are met. We classify rocks into two categories: (i) BIF, allowing mineralisation through fluid contact, and (ii) the other rocks, where fluid permeation does not cause mineralisation. We first propose a reasonable paleo-reconstruction of a given deposit, imposing a fixed tracer concentration in the model's upper region and assume that fluid flow carries the tracer into the domain based on the pressure head boundary conditions that simulate the supergene processes by descending meteoric fluid.

Our model simulates fluid flow in fully saturated rocks, with the top representing the paleo water table level. Given the lack of reliable information on paleo topography, unknown geological time, and hydrological data, we assume a constant height for this water table (i.e., flat) for a specific deposit. We employ the numerical framework of Chapters 2 and 3 to simulate the transport process characterized by significant anisotropy and heterogeneity. The controlling factor is permeability since we model the supergene mimetic substitution of BIF by transporting of an inert fluid, which excludes any chemical reactions. Our numerical stabilised formulation offers the advantage of handling considerable permeability differences between the BIF and shale units, as well as permeability anisotropy within these units. Moreover, our robust numerical formulation enables us to initiate simulations with coarse meshes throughout the domain, allowing the solution strategy to refine where needed for capturing essential solution features without incurring the cost of using a highly detailed mesh everywhere.

In practice, we solve the numerical model in two steps using dimensionless variables and parameters. First, we use the framework of Chapter 2 to simulate a steady-state, heterogeneous, and anisotropic diffusion problem to obtain a pore pressure field ($p$) that drives Darcy flow transport. Next, we use the unsteady extension in Chapter 3 to solve the transient pure advection problem providing the concentration field ($c$). This concentration serves as an iron-ore mineralisation proxy in our model. Although this approach is generic, we focus on two-dimensional cross sections for concise insights into the physical processes involved. We define two systems of equations as follows. Let $\Omega$ be a 2D real

space, $\Gamma$ its boundary. The hydraulic conductivity tensor, $\kappa$, includes local contributions of longitudinal and transverse (scalar permeability) components $\kappa_{\parallel}$ and $\kappa_{\perp}$ relative to the stratigraphic orientation:

$$\kappa := \kappa_{\perp}(n_s \otimes n_s) + \kappa_{\parallel}(\mathbb{I} - (n_s \otimes n_s)), \tag{4.1}$$

where $n_s$ is the stratigraphy's unit normal vector and $\mathbb{I}$ the identity tensor. The longitudinal and transverse components vary spatially. Following our simplification approach, we divide the domain into regions with similar permeability values and assume constant values per region, ideally using a single region. Thus, we express the hydraulic problem as:

$$\begin{aligned} -\nabla \cdot (\kappa \cdot \nabla p) = 0 \quad & \text{in } \Omega, \\ p = 0 \quad & \text{on } \Gamma_{D1}, \\ q \cdot n = h_N \quad & \text{on } \Gamma_{N1}, \end{aligned} \tag{4.2}$$

where $p$ denotes the pressure field and $q$ the Darcy flux, such that $q = \kappa \nabla p$. $\Gamma_{D1}$ and $\Gamma_{N1}$ represent the domain boundaries with constant pressure and flow boundary conditions, respectively. We express the transient transport problem for any instant $t$ in $(0, t_F]$ as:

$$\begin{aligned} \partial_t c + q \cdot \nabla c = 0 \quad & \text{in } \Omega \times (0, t_F], \\ c = g_D \quad & \text{on } \Gamma_{D2} \times (0, t_F], \\ c(\cdot\,, t = 0) = 0 \quad & \text{in } \Omega, \end{aligned} \tag{4.3}$$

where $\Gamma_{D2}$ denotes the domain boundary with constant tracer values as boundary conditions. Our initial unstructured meshes conform to large-scale stratigraphic features, utilizing a constant local rotated diffusion tensor, calculating $n_s$ at each element's centroid in the domain. We use an implicit BDF2 time marching for the unsteady tracer transport problem, an arbitrary final time ($t_F$), and time increments to match patterns across all cases.

We define hydraulic boundary conditions to represent the density-driven flow from descending heavier meteoric fluid, in line with the supergene nature of targeted deposits, without assuming fluid composition. We use a Neumann boundary condition dependent on strata orientation: $h_N = (\kappa \cdot \rho \mathbf{g}) \cdot n$, where $\rho$ represents the density of the strata, and $\mathbf{g}$ denotes the gravitational force. For horizontal

stratigraphy, inflow at the top is proportional to the transverse component ($\kappa_\perp$); for vertical, it's proportional to the longitudinal component ($\kappa_\parallel$). We impose this condition on all boundaries except the bottom, where we set a pressure condition for a unique solution. Boundary conditions dictate flow patterns, and geometric buffers may be added to prevent distortion pollution. For the transient inert tracer problem, we apply homogeneous Dirichlet boundary conditions: zero on all boundaries except the top, where the concentration value is one to simulate mineralisation influx from incoming fluid.

## 4.3 Preprocessing

Reconstructing the geological cross section of Figure 1.2 at the time of mineralisation requires reconstructing various geological features such as topography and strata properties. The height of the paleo water table is the parameter that determines the boundary condition for pore pressure at the top. We consider this parameter as a degree of freedom and use simulation results to determine its value by matching observations; that is, we use a simple inversion process where we match the pattern in a small region by setting appropriate paleo water values and allow the flow in the remainder of the region to evolve given this match. We simulate using a mesh that incorporates the large-scale orientation of the strata in the paleo cross section. In this reconstruction process, we extend the top of the model's geometry to account for potential erosion effects and simplify it with a flat water table profile.

We describe the existing geological cross section using isovalues of an implicit function (potential field) that follows the strata. The gradient of the implicit function provides directional information, which allows us to construct a local permeability tensor using longitudinal and transverse components (see Section 4.1). We extrapolate this information to the upper part of the model, extending the geometric boundaries to align with geological expectations. We utilize the *LoopStructural* [Grose et al., 2021] software for implicit modelling and generate the implicit function using generalized radial basis interpolation. The actual values of the potential field are arbitrary, as only the direction of the gradient matters.

As we describe in the previous chapters, the automatic refinement feature of our numerical framework addresses permeability variations among distinct geological units like shale and BIF. However, due to software constraints, the

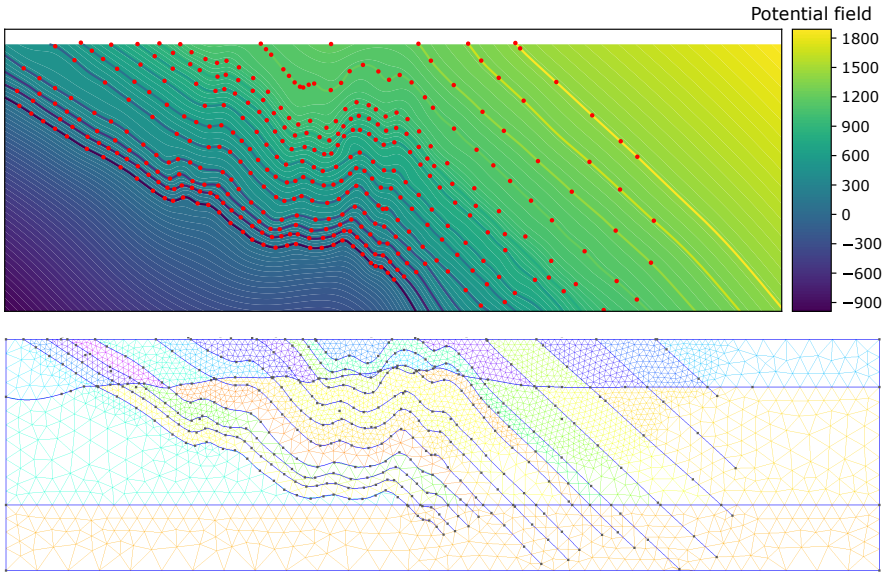


**Figure 4.2:** Input potential field (top) and mesh (bottom) to the supergene mineralisation model. We generate them from the digitised points (red, top figure) representing the stratigraphic layers, either as isopotential values or geometrical boundaries, using respectively *Loop-Structural* and *gmsh* programmatically.

implicit function can only be exported on uniform grids. As a result, we use the *gmsh* meshing package [Geuzaine & Remacle, 2009] separately to create the initial coarse mesh Figure 4.2. We define the different regions using digitised points that outline the geological units and contribute to the implicit function. Using two separate tools can sometimes result in imperfect alignment between mesh region boundaries and the implicit function, necessitating finer meshes near stratigraphic lines to minimise the difference between the spline interpolation of *gmsh* and the radial basis interpolation of *SurfE*.

The position of the model's top is especially significant for boundary conditions (refer to Section 4.2). As we initially solve a pore pressure equilibration problem, the top surface symbolises the paleo water table during mineralisation. In the absence of specific constraints, we opt for flat top surfaces in all cases. The modelling method outlined in this section simplifies the intricate physical process of iron-ore enrichment into a basic transport component with only two adjustable parameters: the elevation, $a$, of the paleo water table and the anisotropy ratio, $r$, of permeability. In short, the modelling approach we describe in this section reduces the complex physical process of iron-ore enrichment to a simplistic transport component with only two free parameters: the altitude, $a$, of the paleo water table and the anisotropy ratio, $r$, of permeability.

## 4.4 Results

We model three scenarios from published cross sections involving separate structural domains in the Hamersley Basin, using the methodology previously mentioned. These applications demonstrate the influence of stratigraphy on mineralisation, irrespective of the structure . The data we employ is accessible to the public, derived from either deposit-scale drilling data (Section 4.4.1 and 4.4.3) or schematic interpretation (Section 4.4.2).

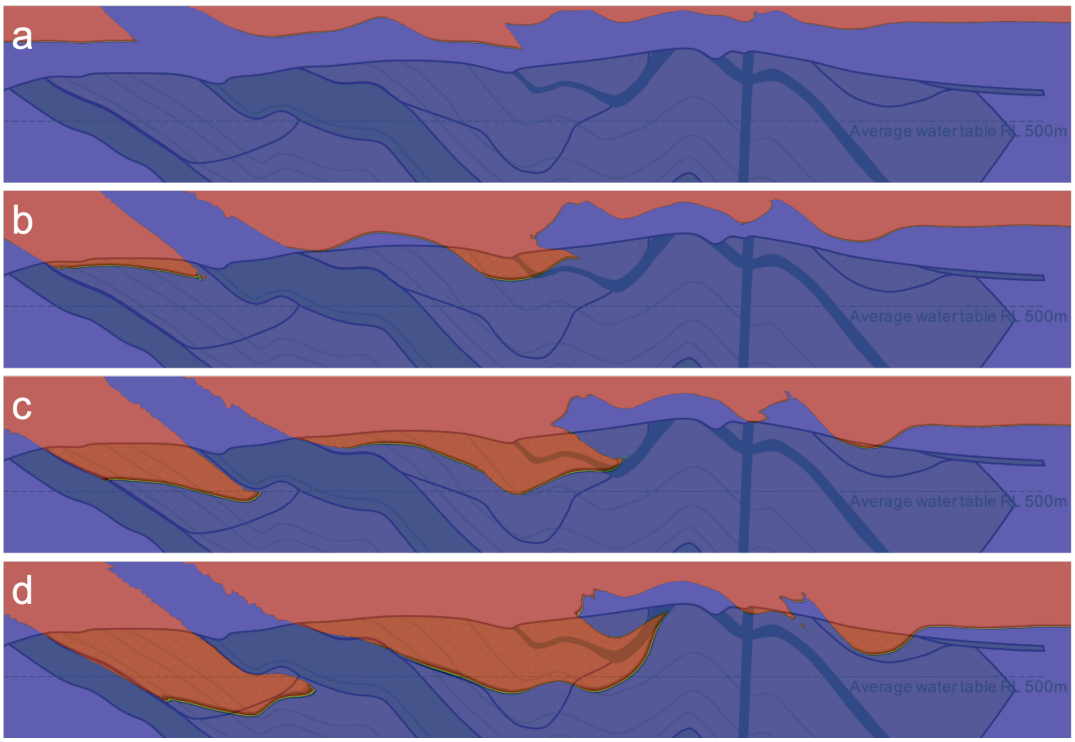


**Figure 4.3:** Snapshots, respectively shown from (a) to (d), of cropped tracer distribution for paleo water table altitude $a = 680m$ at $t = t_1 < t_2 < t_3 < t_4$ during a simulation, highlighting the propagation from the paleo water table (top of the model) and following the strata.

### 4.4.1 Brockman Syncline deposit

The anticline separating the two mineralised regions on the northern side of the cross section of Figure 1.2 is the most interesting feature of the scenario. We hypothesise that the interaction between this geological feature and strata permeability anisotropy leads to the separation of mineralised zones. We test this hypothesis by conducting simulations with different paleo water table heights, using constant permeability values in the BIF and shale regions. We describe

the transport process using a dimensionless form for simplicity, and normalise the permeability values to the longitudinal permeability value in the BIF (i.e., $k_{\parallel}^{BIF} = 1$, while the other values are relative factors). We set $k_{\perp}^{BIF} = \frac{1}{r} = \frac{1}{10}$ and $k_{\parallel}^{shale} = k_{\perp}^{shale} = \frac{1}{3000}$. The low permeability value in the shales imply that the anisotropy parameter is irrelevant since the flow in them is negligible.

The simulations run until the southernmost mineralised area reaches a depth similar to that portrayed in Figure 1.2, with Figure 4.3 showing an example time sequence observed. The distribution is uneven before the tracer reaches the current topography due to the magnitude of the top influx depending on strata orientation. The top boundary position significantly impacts the results, with a paleo water table level of $a \approx 680m$ best matches the observations with the area covered by the simulated tracer as a mineralisation proxy. Figure 4.4 shows a qualitative match for three main mineralisation zones, with the largest discrepancy in the modeled northernmost area's depth (right-hand side of Figure 4.4). Next, we address this discrepancy by introducing a slightly modification of the assumed permeability values (keeping the anisotropy ratio fixed) in the stratigraphic layer above the dolerite sill, even though it forms part of the same geological unit below the sill. Figure 4.5 shows the corresponding plot for a run where the permeability is reduced by a factor 2 in those upper BIF layers.

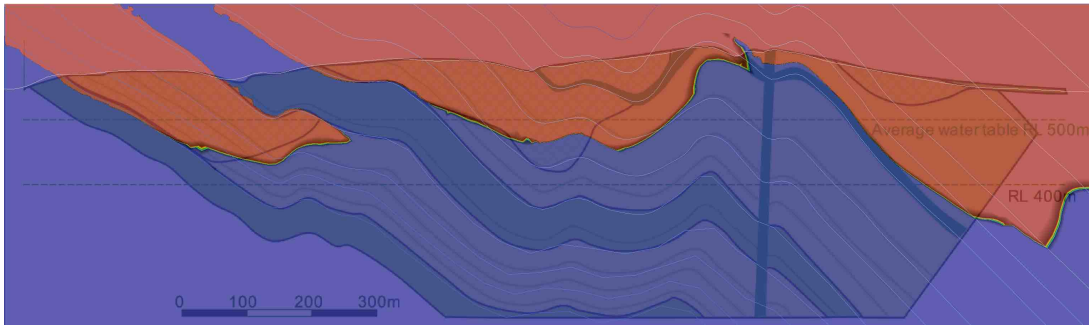


**Figure 4.4:** Tracer distribution for paleo water table altitude $a = 680m$, superimposed over Figure 1.2, using a single set of longitudinal and transverse permeability values in all BIF areas. We define mineralisation by proxy in the area, shaded in red, where the tracer concentration exceeds 20% of the maximal input.

In our simplified model, only two key variables significantly influence the results: the paleo water table head $a$ and the permeability anisotropy ratio $r$. We first show the sensitivity to the paleo water table level $a$ in Figure 4.6, comparing Figure 4.5 with simulations run at $a = 650m$, $680m$, $700m$, and $750m$. The best visual assessment of fit quality between all models and the reference is supported

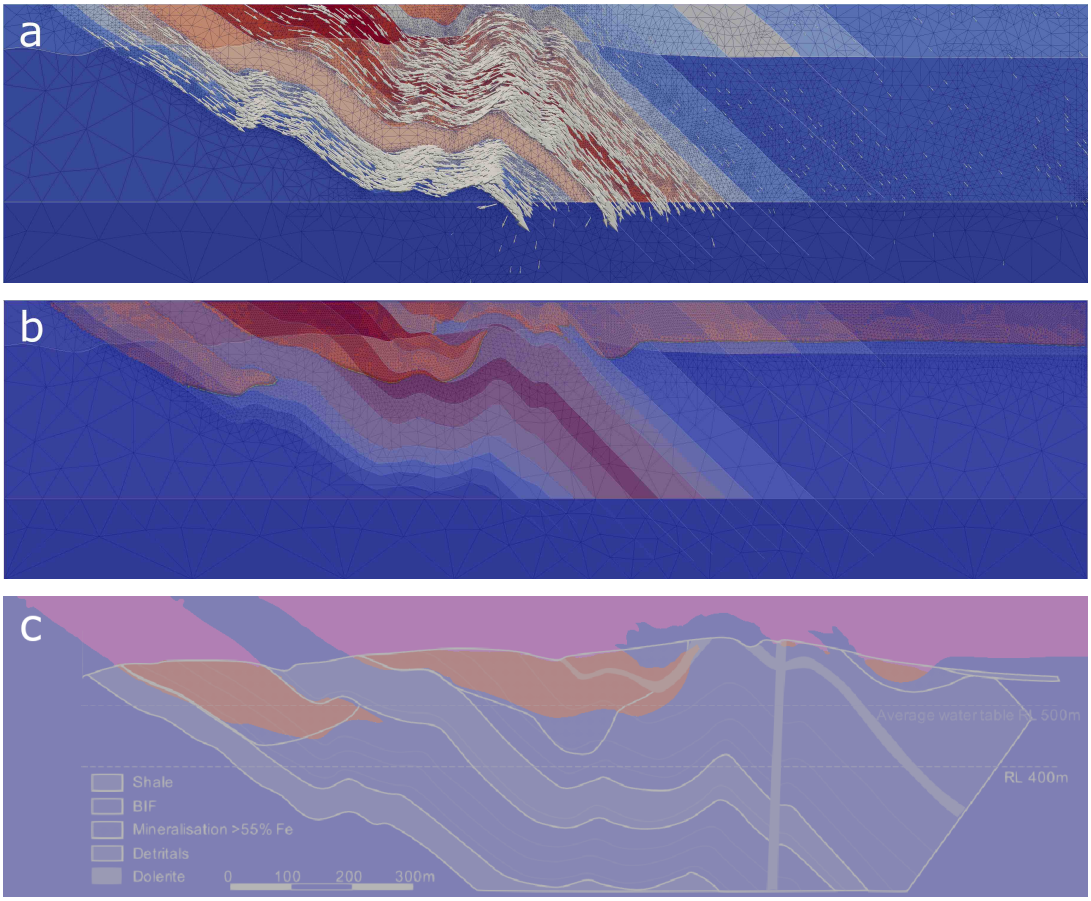


**Figure 4.5:** Decreased permeability above dolerite sill; (a) flow vectors and final mesh after automatic refinement for hydraulic pressure computation; colours display model's arbitrary partition regions highlighting stratigraphy; (b) tracer concentration and mesh after automatic refinement for the final transient transport; (c) tracer concentration, cropped and superimposed over geological cross section for comparison, showing the mineralised areas in orange below the existing topography and in pink in the paleo-reconstruction. The orange colour enhances the visual contrast between the simulation results and the reference geological cross section.

| $a$ **value (m)** | **Precision (-)** | **Recall (-)** | **F1 score (-)** |
|---|---|---|---|
| **650** | 0.609 | 0.896 | 0.725 |
| **680** | 0.874 | 0.829 | 0.851 |
| **700** | 0.870 | 0.790 | 0.828 |
| **750** | 0.909 | 0.769 | 0.833 |

**Table 4.1:** Quantifying simulation results fit for the parameter sensitivity analysis of the paleo water table level $a$, Figure 4.6 shows. Appendix B defines Precision, Recall and F1 score.

by quantitative measures in Appendix B (table 4.1). Simulations show that if the paleo water table level is too low ($a = 650m$), the two northernmost miner-

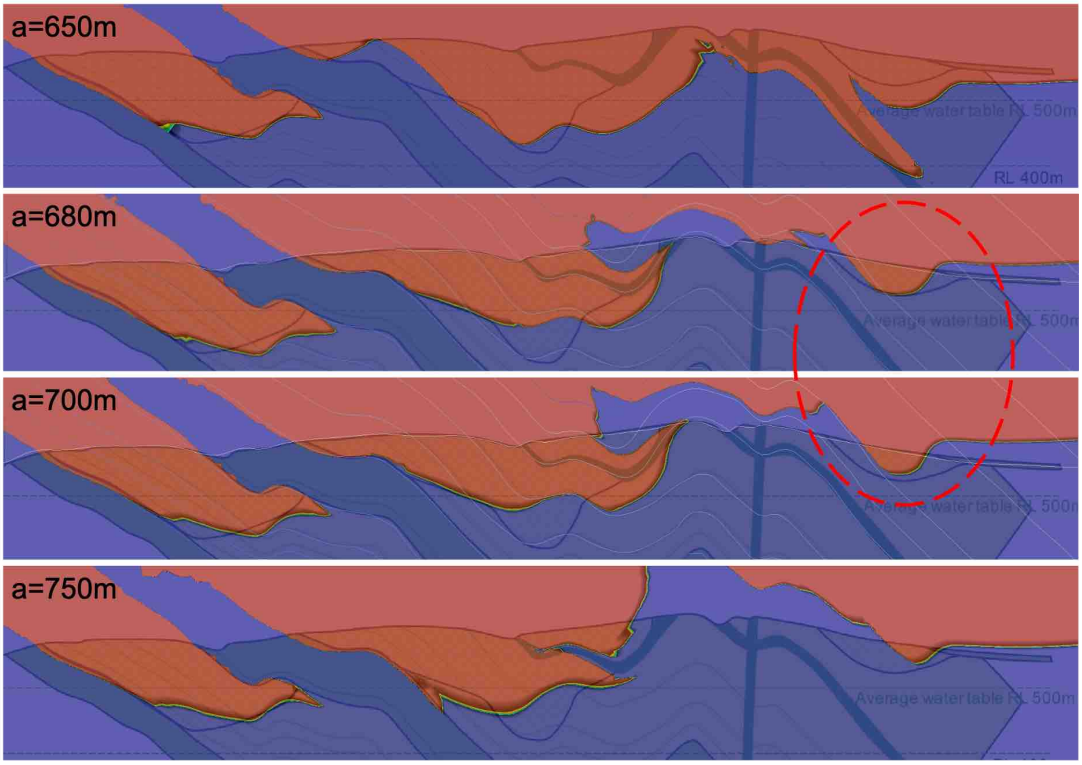


**Figure 4.6:** Sensitivity analysis for water table level $a$, showing tracer results for $a$ = 650, 680, 700 and 750$m$.

alisation areas are inaccurately connected (figure's right hand side). In contrast, if it is too high ($a = 750m$), the two mineralisation zones are separate but the northernmost one is misplaced. These findings reveal the monotonic effect of $a$, suggesting an optimal value around 680$m$. The simulation results for $a = 680m$ and 700$m$ are almost identical in most areas, yet the minor but noticeable differences indicate a significant sensitivity of parameter $a$ due to the differing location and width of the northernmost mineralisation area.

| $r$ **value (-)** | **Precision (-)** | **Recall (-)** | **F1 score (-)** |
|---|---|---|---|
| **1** | 0.758 | 0.773 | 0.765 |
| **20** | 0.874 | 0.829 | 0.851 |
| **100** | 0.815 | 0.850 | 0.832 |

**Table 4.2:** Quantifying simulation results fit for the parameter sensitivity analysis of the anisotropy ratio $r$. Appendix B defines Precision, Recall and F1 score.

Lastly, we analyse the sensitivity of the second parameter by comparing tracer concentration distributions generated with three different permeability anisotropy

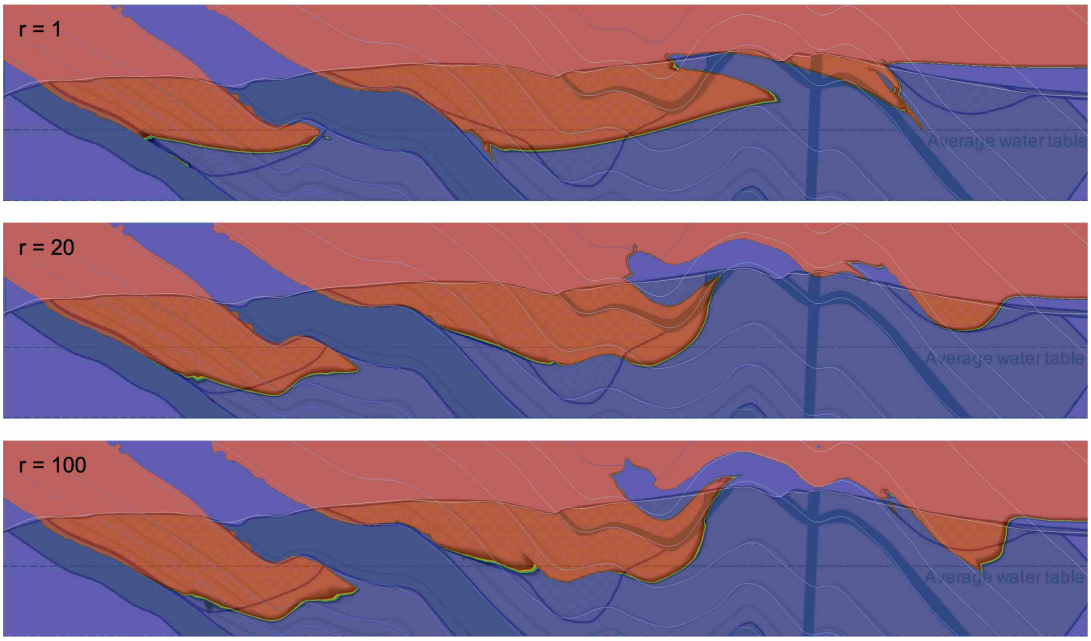


**Figure 4.7:** Permeability anisotropy $r$ sensitivity, tracer results for BIF ratios $r = 1, 20, 100$, while other parameters remain unchanged, superimposed over the geological cross section.

ratio $r$ values (Figure 4.7) at $a = 680m$. The corresponding quantitative fits can be found in table 4.2. As $r$ decreases, permeability becomes less anisotropic, resulting in smoother tracer fronts, as demonstrated by the isotropic case ($r = 1$). The propagation front still exhibits spatial variations due to flow boundary conditions on the top surface. Patterns for higher $r$ values deviate from observations, as the $r = 100$ case indicates with less regular fronts. Despite the order of magnitude difference between $r = 1, 20, 100$ values, the variations are not especially pronounced, suggesting that the model is less sensitive to parameter $r$. Thus, this simple model captures to first-order the mineralisation patterns; next, we test the approach further in another scenario.

### 4.4.2 Marandoo deposit

Section 4.4.1 shows the influence of paleo stratigraphic control on permeability orientation for supergene deposits and underscores the significance of geometric arrangements of favorable geological layers like the Marra Mamba and Brockman Iron Formations. Considering this, we reevaluate Morris [1982] interpretation of the Marandoo ore body's origin. Morris suggested a highly schematic model, which we reproduce in Figure 4.8a. Since the observed mineralisation is limited to the upper part of the Marra Mamba Iron Formation, Morris' original interpre-

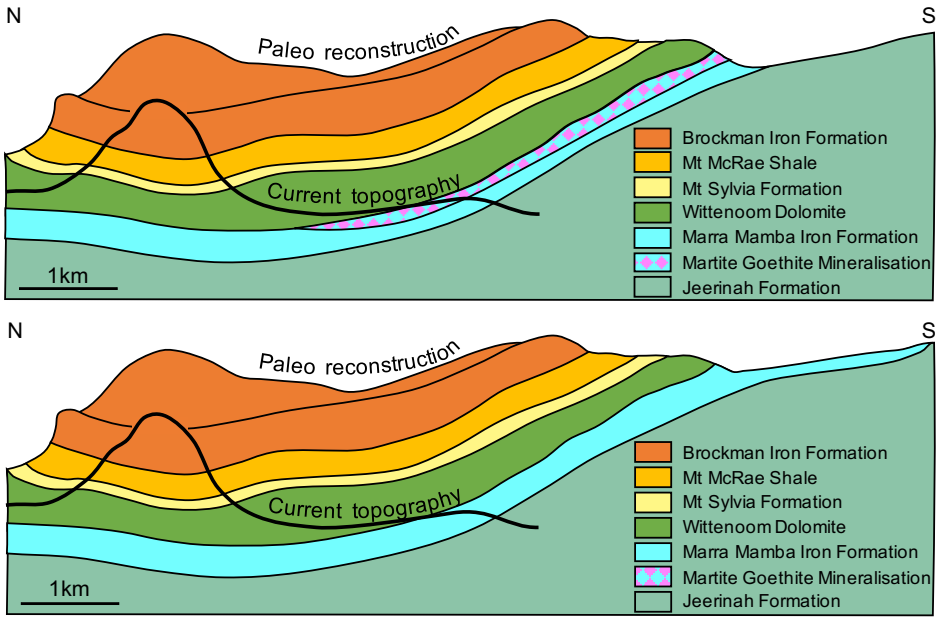


**Figure 4.8:** Marandoo scenario from [Morris, 1982], 1.5x vertical exaggeration. (a) Redrawn version of the original, with observed and inferred mineralisation areas marked, and (b) new proposed model, only altering the geometrical configuration of the Marra Mamba formation around the paleo-topography at the southern end of the cross section to add an extra undulation, as Morris suggested elsewhere on the same figure.

tation extended the same configuration to the paleo reconstruction, leaving the lower part of that unit unmineralised. While the different compositions of geological sublayers might explain this, other areas of the lowest Marra Mamba unit are mineralised [Clout, 2006; Angerer et al., 2014]. This observation warrants re-evaluating the Marandoo scenario from a different perspective to determine if a combination of geometry and permeability distributions could explain the observations without needing to introduce differences in material properties within the Marra Mamba Iron Formation itself. Consequently, we adjust the reconstruction on the southern part of the cross section (see Figure 4.8b) by exposing the Marra Mamba Iron Formation at the paleo-surface over a broader area with a low-angle intersection between that formation and the top surface. We assume the entire Marra Mamba unit can host mineralisation, with longitudinal and transverse permeability values $k^{BIF}\| = 1$ and $k^{BIF}\perp = \frac{1}{50}$.

In contrast, we assume the other units behave like shale with very low permeability, $k^{shale} = \frac{1}{10{,}000}$ to minimise the flow in those areas which are not of interest (including the Brockman Iron Formation in that example). This setup leads to the simulation results shown in Figure 4.9. These results validate our hypothesis

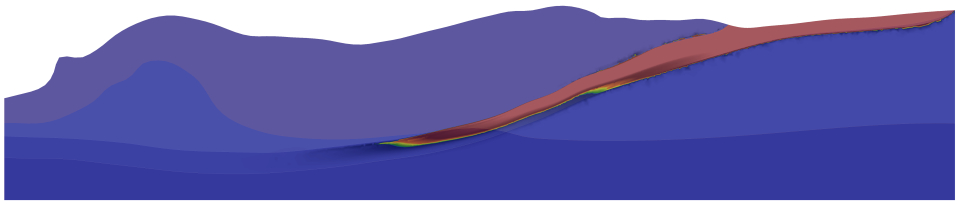

**Figure 4.9:** Simulation results from initial configuration of Figure 4.8b; mineralisation pattern below current topography is restricted to the upper part of the Marra Mamba Iron Formation and matches therefore observations (see Figure 4.8a). Note, however, the main difference with Figure 4.8a above current topography, where mineralisation covers most of the unit.

that the observed mineralisation pattern occurs without extra assumptions regarding the sublayer's fertility for this particular paleo reconstruction. Moreover, we introduce a critical conceptual difference from Morris' interpretation in the Marra Mamba as we conclude that fully mineralised regions may have eroded since then. Finally, the third example extends this scenario to several layers that can potentially host mineralisation.

### 4.4.3 South Flank deposit

The South Flank deposit in the Hamersley Province has a considerably more complex structure, as described by [Perring et al., 2020]. The hydraulic properties of thrusts in that deposit make explaining the mineralisation patterns more challenging; in fact, a three-dimensional reconstruction might be necessary to clarify certain aspects. Nevertheless, we demonstrate that the simplified framework of Section 4.2 can describe a subset of the mineralisation patterns detailed by [Perring et al., 2020], which we replicate in Figure 4.10, in order to draw new conclusions. The data from Perring et al. [2020] is insufficient to reconstruct the paleo-stratigraphy of the deposit as accurately as in Section 4.4.1. Therefore, we propose a conceptual reconstruction that explicitly highlights what we suggest to be the primary driver of the first-order mineralisation pattern: a fold hinge to the north causing the stratigraphy to interact with the paleo topography at a low angle. Extending the bedding upwards at an approximate constant dip would lead to mineralisation in all favourable units, including Newman1 formation where no mineralisation is actually observed.

We test our scenario numerically to determine if this feature is adequate to explain why the mineralisation is limited to only a subset of the potential layers. Lacking available constraints, we assume all units from West Angela 1 downwards

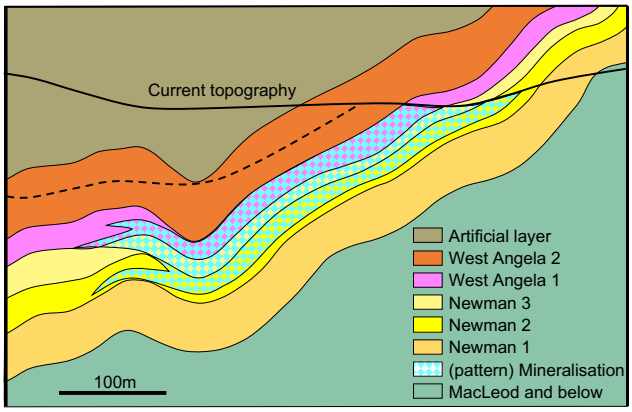


**Figure 4.10:** Model of a section of the South Flank deposit, redrawn from [Perring et al., 2020], showing localized mineralisation mainly within three geological units. The dashed line indicates the upper part of West Angela 2, above which we do not capture the stratigraphy since not relevant for this example. We extrapolate the stratigraphic model above the current topography to suggest an interpreted configuration that could be responsible for the observations.

have the same anisotropic permeability, characterized by constant longitudinal and transverse components, $k^{BIF}\| = 1$ and $k^{BIF}\perp = \frac{1}{50}$. We also lower the permeability components of the West Angela 2 unit by an order of magnitude to reflect its higher shale content compared to the mineralised formations [Simonson et al., 1993; Knight et al., 2018]. The geometric approximation of that layer does not influence the results given the overprinting by other units in the current cross section [see Perring et al., 2020, Figure 8b]. We add an artificial shale layer above West Angela 2 with low permeability $k^{shale} = \frac{1}{3{,}000}$ to reduce that area's impact.

Figure 4.11a shows that a flattened stratigraphy at the paleo-topographic surface level, combined with strong permeability anisotropy, can account for the restricted mineralisation primarily in the Newman 2, Newman 3, and West Angela 1 formations. The lower permeability of West Angela 2 limits the fluid progression, keeping the mineralisation above the current topographic level. Furthermore, the low transverse permeability and the model's top-layer geometry constrain the mineralisation below those three layers. However, the length of the mineralised areas along the units implies a relatively long transport time, during which the fluid propagates deeper than the Newman 2 formation towards the top of the model. These results also offer alternative interpretations. The V-shaped tongue, representing the thinning of the mineralisation pattern at its front, is due to the longitudinal and transverse permeability ratio $r$, which allows a progressively thicker inflow of mineralising fluid at the model's top over

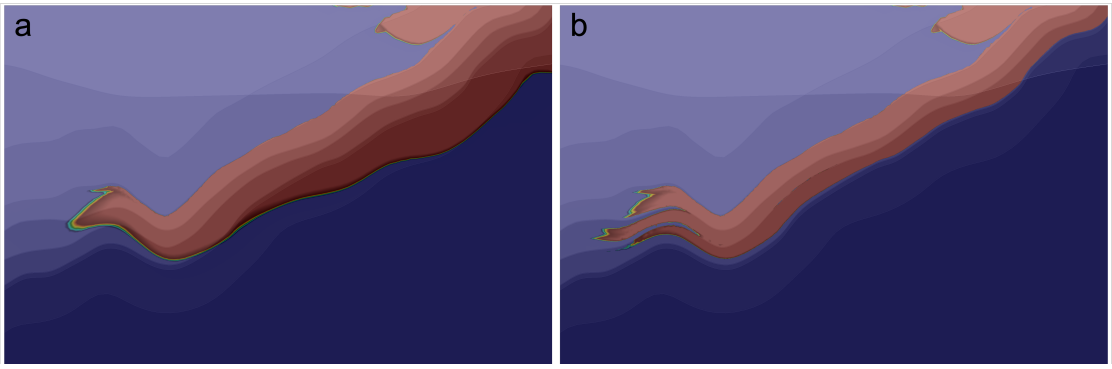


**Figure 4.11:** Two tracer concentrations scenarios, see Figure 4.10. (a) Geological units from West Angela 1 downwards have the same anisotropic permeability. (b) Thin shale layers added at interfaces between West Angela 1, Newman 3, Newman 2 and Newman 1 sub-units.

time through the non-zero transverse permeability component. This flow then propagates faster along the stratigraphic layers, creating a V pattern where the angle/opening of the V front depends on $r$.

By increasing the anisotropy ratio $r$, we can match the overall mineralisation pattern in Figure 4.10. Thus, the mineralising fluids would not propagate below the Newman 2 formation at the top of the model when they have reached their final position laterally. However, this method requires an unreasonably large value of $r$, resulting in a single tongue tip on the propagation front. Observations reveal three tongues (see Figure 4.10), suggesting the presence of at least two low-permeability layers directing fluid propagation parallel to the bedding (see Newman 2 region in Figure 4.10). Therefore, we introduce a thin permeability layer at each interface between the West Angela 1, Newman 3, Newman 2, and Newman 1 sub-units to demonstrate the role of these channelling aquitards. We decrease the permeability in these thin aquitards by two orders of magnitude and arbitrarily set their thickness to 1m. The results in Figure 4.11b qualitatively align with the observations in Figure 4.10.

## 4.5 Discussion

The paleo stratigraphic permeability anisotropy generates fluid flow patterns that match mineralisation areas in the supergene mimetic iron-ore deposits. The discontinuous mineralisation observed in the upper and lower BIF of the Brockman Syncline deposit scenario (Section 4.4.1), as well as within the upper BIF itself, suggests that a single fluid event is responsible for the concurrent supergene

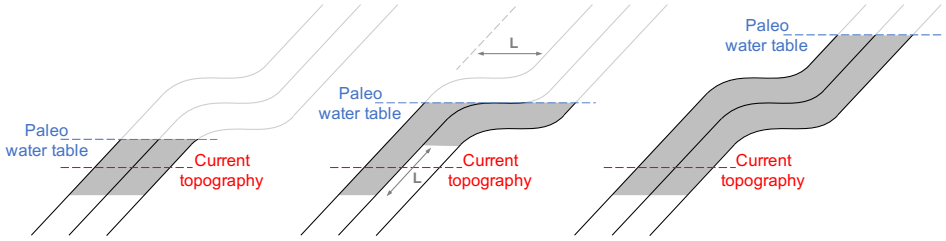


**Figure 4.12:** Analogy with fluid pipes to highlight the conceptual effect of paleo water table level given a particular stratigraphic geometry and strong permeability anisotropy. The scenario at the centre leads to visible mineralisation (i.e., below topography) only in one part of the model, whereas the other scenarios do not allow for it.

mimetic enrichments of all BIF. These results, derived solely from non-reactive fluid flow in a 2D cross section, emphasise the effectiveness of a simplified model in analysing a single aspect of an otherwise highly complex physical process. By excluding most physical processes, our modelling framework reduces the unknowns to two parameters—paleo water table level and permeability anisotropy ratio. This approach captures the core aspects of supergene mimetic ore formation; these examples do not confirm our genetic model, they adequately explain most observed features, reinforcing the supergene origin of the selected deposits. Additionally, the framework can evaluate other deposits' nature and allow us to infer new constraints on the genetic model without further assumptions. Thus, using only uncalibrated absolute permeability values for a transport problem, our model can help interpret numerous complex real physical processes.

A schematic analogy using fluid pipes that mimic a case of infinite anisotropy ratio, where fluid is confined within the strata, can help illustrate the impact of paleo water level on mineralisation (Figure 4.12). This conceptual approach offers an intuitive understanding of how strata geometry and paleo water table levels influence the resulting mineralisation patterns (below the current water topography), resulting in either identical mineralisation in both pipes (Figures 4.12a and c) or distinct mineralisation (Figure 4.12b). The latter configuration is particularly fitting for the Marandoo deposit (Section 4.4.2) and demonstrates that considering lithological differences between sub-units is not always necessary to explain selective mineralisation. A similar schematic approach applies to the mineralisation of the Brockman Syncline deposit (Section 4.4.1 and Figure 4.13).

A water table positioned 180-200m above its current level is necessary for the M-G mineralisation (see Section 4.4.1) and aligns with known climatic conditions featuring increased rainfall during the Paleocene/Eocene period 66-34Ma

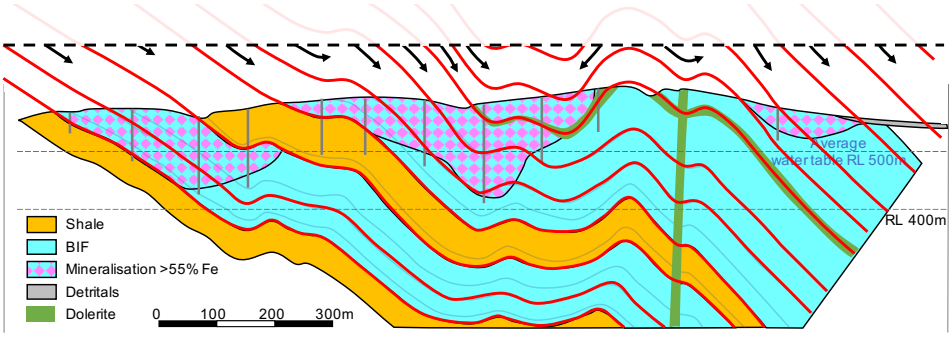


**Figure 4.13:** Schematic drawing of reconstructed strata for the scenario of Section 4.4.1, to highlight the role of the paleo water table (horizontal dashed line) as top boundary condition for the fluid flow (black arrows), whose direction and intensity is strongly affected by the strata orientation and anisotropy coefficient.

[U/Th/He dating, e.g., Vasconcelos et al., 2013]. The accuracy of the modelling results relies on the reliability of the reconstructed stratigraphy, particularly at the model's borders where boundary conditions are enforced. Besides the fact that the predictive ability declines rapidly with the extrapolation distance from the current stratigraphy, it is remarkable how non-horizontal layers supply the necessary information to overcome approximately 200m of erosion with sufficient precision to capture inherent mineralisation patterns. This offers considerable potential for those interested in paleo-reconstruction and timing of supergene deposits in general [e.g., Sanchez et al., 2017].

Our framework's strength lies in its simplicity and flexibility. As shown previously, the geometric configuration of the prospective geological layers, such as the Marra Mamba and Brockman iron formations, determines the mineralisation patterns without distinguishing between the units. This prompts a shift in focus from lithology to strata configuration and a reevaluation of dating studies involving these units with this new perspective of a single fluid flow event across all layers. We re-examine Morris's interpretation of the Marandoo ore body's origin, demonstrating that a combination of geometric configurations and strong permeability anisotropy can account for the current structure while acknowledging that mineralisation can occur in the lower part of the Marra Mamba, consistent with other observations. By slightly adjusting Morris's Marandoo reconstruction on the southern portion of the cross section, we achieve similar mineralisation distributions but with a notable conceptual difference. The mineralisation pattern could potentially arise solely from permeability anisotropy and the configuration of the exposed area during mineralisation (Figure 4.9). While matching current

observations, this scenario presents an alternative interpretation: we predict double the potential mineralisation volume in the paleo reconstructed zone, a crucial factor for any analysis focusing on prospectivity and iron-ore mass budgets. A similar conclusion can be drawn from the Brockman syncline (Figure 4.5), where vast mineralised areas were arguably eroded just above barren or low mineralisation zones. The chosen three deposit locations from different structural domains in the Hamersley Basin demonstrate that permeability anisotropy controls mineralisation, putting existing discussions about the influence of structure into perspective, especially in the context of mineral exploration. These results show that permeability orientation during mineralisation is more important than the structural history responsible for that configuration.

Herein, we only consider 2D cross sections, but this does not negate the crucial role of 3D effects in potentially controlling mineralisation. Limiting ourselves to 2D was a design choice rather than a methodological limitation, as we could illustrate our points without adding extra complexity. Incorporating 3D features in the geometry might change the flow patterns but would necessitate more observations. Likewise, our emphasis on permeability anisotropy alone does not disregard the importance of other physical processes, coupling feedbacks, or spatial variations of the paleo water table and material parameters. In particular, forward stratigraphic modelling [e.g., Barabasch et al., 2018] or more specific analyses involving diagenesis [Mangenot et al., 2019] could provide additional valuable information on stratigraphy and permeability. While these refinements may enhance our predictions, introducing unconstrained new parameters might weaken our approach. The most significant outcome of this study is the first-order match of observations by our simulations without assuming ad hoc parametrisations of those factors. Our framework's extreme simplicity allows us to draw meaningful conclusions by focusing on a single aspect of the problem: the permeability anisotropy resulting from the paleo-stratigraphic orientation. This approach is especially effective for gaining insights in complex situations.

Our numerical framework can readily handle 3D scenarios, even though the computational cost increases (see Chapters 2 and 3). Similarly, the methodology can address various complex modelling features, like discontinuities around faults. The combined power of the modelling and simulation frameworks opens new avenues for investigating the relative timing of structural evolution concerning the last fluid flow component responsible for mineralisation. Lastly, while we only

discuss the transport component to minimise the number of parameters involved, the methodology allows for further physical complexity to test other aspects of the iron-ore enrichment process. Drawing upon our numerical framework's results, we anticipate the potential to tackle more complex supergene mineralisation processes by incorporating explicit chemistry. This modification would introduce non-linear terms into our framework, a challenge we have shown our capability to manage (see sections 2.5 and 3.6). This strategy is promising for reactive systems where non-linearity arises from chemical reactions, as observed in genetic models such as weathering or electrochemical processes.

# Chapter 5

# Conclusions and research perspectives

## 5.1 Concluding Remarks

This work studies the genetic model that explains the mechanism governing the genesis of the (Banded Iron Formations) BIF supergene martite-goethite ore deposits using a robust computational framework we construct. Our research has substantially advanced the understanding of the role of paleo-stratigraphic permeability anisotropy in controlling mineralisation patterns within these geological formations. We use a simplified flow model to implicitly represent strata with a potential function, which accurately orients the permeability tensor from a paleo reconstruction of the relevant geological features, including topography and strata properties. The model regulates the supergene enrichment transport process and distribution patterns of mineralisation by the permeability anisotropy of the paleo-stratigraphy. Building on the anisotropy that the strata deposition induces on the sedimentary layers, our model allows for greater permeability along the strata than across them.

The first part of this thesis presents a stabilised finite element method based on residual minimisation on dual norms and reinterprets the method using a variational multiscale approach to improve the solution's accuracy. This method obtains a coarse-scale approximation by minimising the residual on a dual discontinuous Galerkin norm and derives fine-scale approximations using the variational multiscale framework. This framework allows the model to handle sharp permeability changes, avoiding ill-defined stabilisation terms in the variational formula-

tion and reducing the computational effort using an optimal adaptive refinement scheme. The work covered the steady and unsteady advection-dominated diffusion equations, as well as some nonlinear extensions.

The second part of this thesis uses this robust numerical framework to constrain the relative timing of mineralisation within well-established BIF deposits from existing literature and reinforce our approach's validity. The critical outcomes of our study are as follows:

- We developed a theoretical model to understand iron-ore genesis in BIF. This model attributes the mineralisation patterns within these formations predominantly to paleo-stratigraphic permeability anisotropy, enhancing our comprehension of these processes.

- We postulate that the supergene mimetic mineralisation in various geological members stems from a singular fluid flow event. This highlights the pivotal role of transport processes over chemical effects in dictating mineralisation patterns in these formations.

- We successfully demonstrated the efficiency of a robust numerical framework for studying Martite-Goethite iron-ore formation scenarios. Our approach applies to steady and unsteady problems encountered in BIF deposits, providing a novel perspective on these geological formations.

- By employing a numerical modelling approach, we managed to delineate the relative timing of mineralisation, particularly to the paleo water table level and anisotropy ratio. Comparing the predictions of our model with well-documented BIF deposits from existing literature, we have reinforced the validity of our methodology. This understanding broadens our knowledge of how these variables (paleo water table level and anisotropy ratio) influence the mineralisation process.

In numerical analysis, our study made several significant contributions:

- We developed an automated, stabilised finite element method specifically for unsteady, diffusion-advection-reaction problems. Rooted in the principles of residual minimisation and the method of lines, this method ensures stable solutions and robust error representation. The versatility and robustness of our approach have enabled its application to a broad range of challenging

problems, including those characterised by high heterogeneity and strong anisotropic diffusion tensors, as well as those dominated by advection.

- We utilised the variational multiscale approach as an effective post-processing tool, which allowed us derive a fine-scale approximation from a reinterpretation of a residual projection. This methodology delivers stable coarse- and fine-scale solutions from a symmetric saddle-point formulation. We also introduced a heuristic duality-inspired post-processing approach to enhance the variational form, improving the full-scale approximation for symmetric formulations such as the diffusion problem.

- Our adaptive-stabilised method handles different linear and nonlinear problems, reaching ideal spatial and temporal convergence. This method may help us deal with more complex supergene mineralisation processes through the inclusion of explicit chemistry. This approach could be useful for reactive systems, where non-linearity comes from chemical reactions, as seen in genetic models like weathering or electrochemical processes.

- The adaptive refinement process of our method can effectively reduce the computational cost required to solve the saddle-point problem resulting from residual minimisation. This technique demonstrated improvements in computational cost for different localised discontinuities compared to uniformly refined schemes based on discontinuous Galerkin approximation.

## 5.2 Research Outlook

The research conducted in this study lays a strong foundation for future investigations. There are several directions in which this research can be extended:

- Additional experimental and field studies are needed to better understand the permeability anisotropy in rocks at various stages of mineralisation. Such studies will further refine our understanding of the mineralisation processes and provide more sophisticated tools for mineral exploration.

- The generic nature of our fluid flow simulations suggests the potential for broader application. The conceptual simplification and modelling components could be extended to a more comprehensive range of commodities in sedimentary basins that involve a supergene component like porphyry,

epithermal and strata-bound deposits in general, all around the world. Besides, our research could be expanded to more complex and realistic 3D geological settings and commodities.

- The introduction of our stabilised finite element method opens up possibilities for more advancements in numerical analysis. This method is applicable to a wide variety of problems, such as those found in aerospace or environmental engineering, bio-medicine, and other fields. This could make it more useful and reliable for a broader range of applications.

Our methodology, proven effective for identifying enriched mineralisation zones for iron ore, is a valuable tool in practical scenarios, including for mineral exploration of other commodities globally. By precisely predicting mineral locations, it holds the potential to trim exploration costs and mitigate environmental impacts. The possibility of applying our methodology across various sectors in the extraction and manufacturing industries further elevates its utility. Our research improved the community's understanding of mineralisation processes and stratigraphic permeability anisotropy while enhancing numerical analysis methodologies. With ongoing advancements in computational power and modelling complexity, we look forward to refining our understanding and improving prediction accuracy.

# Appendices

# Appendix A

# Proof. Discrete coercivity and inf-sup condition for $B_{h,\tau}$

## A.1 Discrete coercivity

*Proof.* (I) The operator $B_{h,\tau}$ satisfies discrete coercivity (1); then,

$$(v, B_{h,\tau}v) = (v, v + \tau B_h v) \geq \|v\|_0^2 + C_{sta}\tau\|v\|_{\tilde{\mathcal{V}}}^2. \tag{A.1}$$

Therefore,

$$(v, B_{h,\tau}v) \geq \|v\|_0^2 + C_{sta}\tau\|v\|_{\tilde{\mathcal{V}}}^2 \geq \min(1, C_{sta})\|v\|_{\tilde{\tau}}^2, \tag{A.2}$$

thereby proving 3.18.

(II) Using the Cauchy-Schwartz inequality for the first term, and implementing the coercivity for the operator $B_h$, we obtain that, for all $(v, w) \in \mathbb{V}_h \times \mathbb{V}_*$:

$$(v, B_{h,\tau}w) := (v, w + \tau B_h w) \leq \|v\|_0\|w\|_0 + \tau(v, B_h w)_0, \tag{A.3}$$

$$(v, B_{h,\tau}w) \leq \|v\|_0\|w\|_0 + \tau C_{bnd}\|v\|_{\tilde{\mathcal{V}}}\|w\|_{\tilde{\mathcal{V}},*} \leq \|v\|_0\|w\|_0 + C_{bnd}\sqrt{\tau}\|v\|_{\tilde{\mathcal{V}}}\sqrt{\tau}\|w\|_{\tilde{\mathcal{V}},*}. \tag{A.4}$$

Using $\|w\|_{\tilde{\tau},*} \geq \|w\|_0$ and $\|v\|_{\tilde{\tau}} \geq \|v\|_0$, and the inequalities $\|w\|_{\tilde{\tau},*} \geq \sqrt{\tau}\|w\|_{\tilde{\mathcal{V}},*}$ and $\|v\|_{\tilde{\tau}} \geq \sqrt{\tau}\|v\|_{\tilde{\mathcal{V}}}$ from the norm definitions (3.16), then,

$$(v, B_{h,\tau}w) \leq \|v\|_0\|w\|_0 + C_{bnd}\|v\|_{\tilde{\tau}}\|w\|_{\tilde{\tau},*} \leq (1 + C_{bnd})\|v\|_{\tilde{\tau}}\|w\|_{\tilde{\tau},*}. \tag{A.5}$$

□

## A.2 Inf-sup condition

*Proof.* To establish the inf-sup condition property in the operator $B_{h,\tau}$, we adopt a similar approach as presented in Di Pietro & Ern [2011] and Ayuso & Marini [2009] to demonstrate Theorem 1. The proof of the operator $B_h$ relies on certain assumptions made in these sources. We recall the definition of the norm $\|u\|_{\tau^*}^2$ in terms of $\|u\|_\beta^2$, defined as:

$$\|u\|_\beta^2 := \sum_{K\in\mathfrak{T}} \beta_c^{-1} h_T \|\beta\cdot\nabla u\|^2, \tag{A.6}$$

then,

$$\|u\|_\tau^2 := \|u\|_{\tilde{\tau}}^2 + \tau\|u\|_\beta^2. \tag{A.7}$$

Using the discrete coercivity property in (3.18), and setting $\mathbb{S} := \sup_{w\in\mathbb{V}_h\setminus\{0\}} \frac{b_{h,\tau}(v,w)}{\|w\|_\tau}$ for $v\in\mathbb{V}_h\setminus\{0\}$, then:

$$\|v\|_{\tilde{\tau}}^2 \lesssim b_{h,\tau}(v,v) = \frac{b_{h,\tau}(v,v)}{\|v\|_\tau}\|v\|_\tau \leq \mathbb{S}\|v\|_\tau, \tag{A.8}$$

where, we set $w = \beta_c^{-1} h_K \langle\beta\rangle_K \nabla v$ for all $K\in\mathfrak{T}_\mathfrak{h}$ with $w\in\mathbb{V}_h$. We define $\langle\beta\rangle_K$ as the mean value of $\beta$ over $K$. We divide the proof in five parts:
(i) Since $\|w\|_\beta \lesssim \|v\|_\beta$ (see proof of Lemma 2.35 in Di Pietro & Ern [2011]) and the inverse inequality $\|w\|_0 \lesssim \|v\|_0$ (see lemma 1.44 in Di Pietro & Ern [2011]), then,

$$\|w\|_\tau \lesssim \|v\|_\tau.$$

(ii) From the definition of the norm (3.16), we infer that $\|v\|_{\tilde{\tau}}^2 > \tau\|v\|_{\tilde{\mathcal{V}}}^2$ and $\|v\|_{\tilde{\tau}} > \sqrt{\tau}\|v\|_{\tilde{\mathcal{V}}}$. In addition, from (3.17) we obtain that $\|v\|_\tau > \sqrt{\tau}\|v\|_{\mathcal{V}}$. Hence,

$$\|v\|_{\tilde{\tau}}\|v\|_\tau \geq \sqrt{\tau}\|v\|_{\tilde{\mathcal{V}}}\|v\|_\tau \geq \tau\|v\|_{\tilde{\mathcal{V}}}\|v\|_{\mathcal{V}}.$$

(iii) Starting from definition (3.13) and recalling the section (ii) in the Lemma 2.35 in Di Pietro & Ern [2011]:

$$\sum_{K\in\mathfrak{T}} \beta_c^{-1} h_T \|\beta\cdot\nabla v\|^2 = b_h(w,v) - \mathcal{I}, \tag{A.9}$$

where,

$$\mathcal{I} := -b_h(w,v)^{\text{sip}} - \sum_{K\in\mathfrak{T}} (w,\mu v)_K + \sum_{K\in\mathfrak{T}} \beta_c^{-1} h_T(\nabla v, (\beta\cdot\nabla v)(\beta - \langle\beta\rangle_T))_K$$
$$- \sum_{F\in\mathscr{S}_h^\partial\cap\Gamma^-} (w,(\beta\cdot n)\, v)_F + \sum_{F\in\mathscr{S}_h^0} (\{w\}, (\beta\cdot\mathbf{n}_F)[\![v]\!]) - \sum_{F\in\mathscr{S}_h^\partial} \left(\tfrac{1}{2}|\beta\cdot\mathbf{n}_F|[\![w]\!],[\![v]\!]\right)_F. \tag{A.10}$$

We can write $\|v\|_\tau^2$ in terms of the new bilinear operator $b_{h,\tau}(\cdot,\cdot)$, such that

$$\tau\|v\|_\tau^2 = b_{h,\tau}(w,v) - (w,v)_0 - \tau\mathcal{I}. \tag{A.11}$$

We can bound the first term in the rhs of (A.11) by using (A.8) and (i); the second term through the Cauchy-Schwartz inequality; and, the last term having an extension of the proof (ii) in Di Pietro & Ern [2011], such that

$$|b_{h,\tau}(w,v)| \le \mathbb{S}\|w\|_\tau \lesssim \mathbb{S}\|v\|_\tau, \qquad |(w,v)_0| \lesssim \|w\|_0\|v\|_0 \lesssim \|v\|_0^2$$

and

$$\tau\mathcal{I}_a \lesssim \tau(\|v\|_{\tilde{\mathcal{V}}}\|v\|_{\mathcal{V}} + \|v\|_{\mathcal{V}}^2),$$

with $\tau\mathcal{I}_a := \tau(|\mathcal{I}_1| + |\mathcal{I}_2| + \cdots + |\mathcal{I}_6|)$. Summarising, it holds that:

$$\tau\sum_{K\in\mathfrak{T}} \beta_c^{-1} h_T\|\beta\cdot\nabla u\| \lesssim \mathbb{S}\|v\|_\tau + \|v\|_0^2 + \tau(\|v\|_{\tilde{\mathcal{V}}}\|v\|_{\mathcal{V}} + \|v\|_{\tilde{\mathcal{V}}}^2) \tag{A.12}$$

$$\tau\sum_{K\in\mathfrak{T}} \beta_c^{-1} h_T\|\beta\cdot\nabla u\| \lesssim \mathbb{S}\|v\|_\tau + \tau\|v\|_{\tilde{\mathcal{V}}}\|v\|_{\mathcal{V}} + \|v\|_{\tilde{\tau}}^2 \tag{A.13}$$

Using (ii), we obtain:

$$\tau\sum_{K\in\mathfrak{T}} \beta_c^{-1} h_T\|\beta\cdot\nabla u\| \lesssim \mathbb{S}\|v\|_\tau + \|v\|_{\tilde{\tau}}\|v\|_\tau + \|v\|_{\tilde{\tau}}^2 \tag{A.14}$$

(v) Combining the above result with (A.8) and using Young's inequality, hence,

$$\tau\sum_{K\in\mathfrak{T}} \beta_c^{-1} h_T\|\beta\cdot\nabla v\| \lesssim \|v\|_\tau^2 \lesssim \mathbb{S}\|v\|_\tau + \|v\|_{\tilde{\tau}}\|v\|_\tau \tag{A.15}$$

$$\|v\|_\tau^2 \lesssim \mathbb{S}\|v\|_\tau + \|v\|_{\tilde{\tau}}^2 \lesssim \mathbb{S}\|v\|_\tau \quad \forall\ v\in\mathbb{V}_h, \tag{A.16}$$

which yields de assertion. □

# Appendix B

# Quantifying the fit between simulations and observations

The fit between simulation results and corresponding references (based on observation) can partly be assessed using classical model evaluation techniques. While no method exists that fully replaces expert human interpretation (e.g. accounting for specific qualitative features of interest in particular areas), the following metrics are particularly useful to derive quantitative values overall.

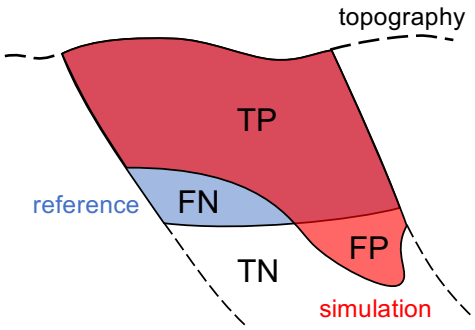


**Figure B.1:** Quantifying the fit between simulation (red) and reference (blue) areas of mineralisation. Image processing allows to classify the match in zones of True Positive (TP), False Positive (FP), True Negative (TN) and False Negative (FN).

For a given scenario, we analyse the images representing respectively the simulated and reference mineralisation areas below the current topography, as illustrated on Figure B.1. We identify through image processing the respective areas of the True Positive ($TP$), False Positive ($FP$), True Negative ($TN$) and False Negative ($FN$) zones, which in turn allow the calculations of $P$, $R$, and

$F1$ scores defined as:

$$P = \frac{TP}{TP + FP}, \tag{B.1}$$

$$R = \frac{TP}{TP + FN}, \tag{B.2}$$

$$F1 = 2 \times \frac{P \times R}{P + R}. \tag{B.3}$$

All scores are values between 0 and 1, with higher values indicating a better match. The $P$ indicates the proportion of simulated mineralisation area that falls within the reference mineralisation area, i.e the percentage of correct prediction. The $R$ score measures the True Positive rate, i.e the proportion of reference mineralisation area captured by the simulation. The *F1* score encompasses both aspects, with a value of 1 denoting a perfect match and the value of 0 signifying that no pixel of simulated mineralisation falls within the reference mineralisation area at all.

For the example shown in Figure B.1, the values obtained are $P \approx 0.880$, $R \approx 0.869$ and $F1 \approx 0.875$. (It is only incidental that those three values are so similar in that example, as they capture different concepts.) In this study, we use mainly the *F1* score to quantify the fits when quantifying the sensitivity of specific parameters.

# Bibliography

J.F. Giraldo & V.M. Calo (2023). 'An Adaptive in Space, Stabilized Finite Element Method via Residual Minimization for Linear and Nonlinear Unsteady Advection–Diffusion–Reaction Equations'. *Mathematical and Computational Applications* **28**(1):7.

J.F. Giraldo, S. Rojas & V.M. Calo (2021). 'An Adaptive Stabilized Finite Element Method Based on Residual Minimization for Unsteady Advection-diffusion Problems'. Presentations and videos to 10th International Conference on Adaptative Modeling and Simulation (ADMOS).

M. Alnæs, et al. (2015). 'The FEniCS project version 1.5'. *Archive of Numerical Software* **3**(100).

T. Angerer, et al. (2014). 'A mineral system approach to iron ore in Archaean and Palaeoproterozoic BIF of Western Australia'. *Geological Society, London, Special Publications* **393**(1):81–115.

R. Araya & P. Venegas (2014). 'An a posteriori error estimator for an unsteady advection-diffusion- reaction problem'. *Computers and Mathematics with Applications* **66**(12):2456–2476.

D. N. Arnold, et al. (2001). 'Unified analysis of discontinuous Galerkin methods for elliptic problems'. *SIAM Journal on Numerical Analysis* **39**(5):1749–1779.

Australia (2021). 'Resources and Energy Quarterly, December 2021'.

B. Ayuso & L. D. Marini (2009). 'Discontinuous Galerkin methods for advection-diffusion-reaction problems'. *SIAM J. Numer. Anal.* **47**(2):1391–1420.

I. Babuška & M. Zlámal (1973). 'Nonconforming elements in the finite element method with penalty'. *SIAM J. Numer. Anal.* **10**:863–875.

R. E. Bank & D. J. Rose (1981). 'Global approximate Newton methods'. *Numerische Mathematik* **37**(2):279–295.

R. E. Bank, et al. (1989). 'A class of iterative methods for solving saddle point problems'. *Numerische Mathematik* **56**(7):645–666.

J. Barabasch, et al. (2018). 'Integrated 3D forward stratigraphic and petroleum system modeling of the Levant Basin, Eastern Mediterranean'. *Basin Research* .

M. Barley, et al. (1999). 'Hydrothermal origin for the 2 billion year old Mount Tom Price giant iron ore deposit, Hamersley Province, Western Australia'. *Mineralium Deposita* **34**(8):784.

V. A. Baskov (1987). 'Regional groundwater flow and the formation of Mississippi Valley-type lead-zinc deposits'. *Geology* **15**(11):1001–1004.

Y. Bazilevs, et al. (2007). 'Variational multiscale residual-based turbulence modeling for large eddy simulation of incompressible flows'. *Computer Methods in Applied Mechanics and Engineering* **197**(1):173–201.

Y. Bazilevs, et al. (2010). 'Isogeometric variational multiscale modeling of wall-bounded turbulent flows with weakly enforced boundary conditions on unstretched meshes'. *Computer Methods in Applied Mechanics and Engineering* **199**(13):780–790. Turbulence Modeling for Large Eddy Simulations.

P. Behnoudfar, et al. (2020a). 'A variationally separable splitting for the generalized-$\alpha$ method for parabolic equations'. *International Journal for Numerical Methods in Engineering* **121**(5):828–841.

P. Behnoudfar, et al. (2022). 'A variational splitting of high-order linear multistep methods for heat transfer and advection–diffusion parabolic problems'. *Journal of Computational Science* **63**:101807.

P. Behnoudfar, et al. (2020b). 'High-order generalized-$\alpha$ method'. *Applications in Engineering Science* **4**:100021.

C. M. Bethke (1989). 'Modeling subsurface flow in sedimentary basins'. *Geologische Rundschau* **78**:129–154.

P. Bochev, et al. (2005). 'A multiscale discontinuous Galerkin method'. In *International Conference on Large-Scale Scientific Computing*, pp. 84–93. Springer.

M. Boni & N. Mondillo (2015). 'The "Calamines" and the "Others": The great family of supergene nonsulfide zinc ores'. *Ore Geology Reviews* **67**:208–233.

R. Borker, et al. (2017). 'A high-order discontinuous Galerkin method for unsteady advection–diffusion problems'. *Journal of Computational Physics* **332**:520–537.

J. H. Bramble & V. Thomée (1972). 'Semidiscrete least-squares methods for a parabolic boundary value problem'. *Mathematics of Computation* **26**(119):633–648.

F. Brezzi, et al. (2006). 'Stabilization mechanisms in discontinuous Galerkin finite element methods'. *Computer Methods in Applied Mechanics and Engineering* **195**(25-28):3293–3310.

A. N. Brooks & T. J. Hughes (1982). 'Streamline upwind/Petrov-Galerkin formulations for convection dominated flows with particular emphasis on the incompressible Navier-Stokes equations'. *Computer methods in applied mechanics and engineering* **32**(1-3):199–259.

A. Buffa, et al. (2006). 'Analysis of a multiscale discontinuous Galerkin method for convection-diffusion problems'. *SIAM Journal on Numerical Analysis* **44**(4):1420–1440.

E. Burman (2009). 'A posteriori error estimation for interior penalty finite element approximations of the advection-reaction equation'. *SIAM J. Numer. Anal.* **47**(5):3584–3607.

E. Burman & A. Ern (2005). 'Stabilized Galerkin approximation of convection-diffusion-reaction equations: discrete maximum principle and convergence'. *Math. Comp.* **74**(252):1637–1652.

E. Burman & A. Ern (2007). 'Continuous interior penalty *hp*-finite element methods for advection and advection-diffusion equations'. *Math. Comp.* **76**(259):1119–1140.

E. Burman & P. Hansbo (2004). 'Edge stabilization for Galerkin approximations of convection-diffusion-reaction problems'. *Comput. Methods Appl. Mech. Engrg.* **193**(15-16):1437–1453.

E. Burman & P. Zunino (2006). 'A domain decomposition method based on weighted interior penalties for advection-diffusion-reaction problems'. *SIAM Journal on Numerical Analysis* **44**(4):1612–1638.

V. Calo, et al. (2021). 'Isogeometric Residual Minimization Method (iGRM) with direction splitting preconditioner for stationary advection-dominated diffusion problems'. *Computer Methods in Applied Mechanics and Engineering* **373**:113214.

V. M. Calo, et al. (2014). 'Analysis of the discontinuous Petrov–Galerkin method with optimal test functions for the Reissner–Mindlin plate bending model'. *Computers & Mathematics with Applications* **66**(12):2570–2586.

V. M. Calo, et al. (2020a). 'An adaptive stabilized conforming finite element method via residual minimization on dual discontinuous Galerkin norms'. *Computer Methods in Applied Mechanics and Engineering* **363**:112891.

V. M. Calo, et al. (2020b). 'An adaptive stabilized conforming finite element method via residual minimization on dual discontinuous Galerkin norms'. *Computer Methods in Applied Mechanics and Engineering* .

B. Campana (1966). 'Stratigraphic-Structural-Paleoclimatic controls of the newly discovered iron ore deposits of Western Australia'. *Mineralium Deposita* **1**:53–59.

A. Cangiani, et al. (2014). 'Adaptive discontinuous Galerkin methods for non-stationary convection-diffusion problems'. *IMA Journal of Numerical Analysis* **34**(4):1578–1597.

J. Chan & J. A. Evans (2013). 'A minimum-residual finite element method for the convection-diffusion equation'. Tech. rep., Texas Univ at Austin inst for computational engineering and science.

K. Chang, et al. (2012). 'Isogeometric variational multiscale large-eddy simulation of fully-developed turbulent flow over a wavy wall'. *Computers & Fluids* **68**:94–104.

R. J. Cier, et al. (2021a). 'A nonlinear weak constraint enforcement method for advection-dominated diffusion problems'. *Mechanics Research Communications* **112**:103602.

R. J. Cier, et al. (2021b). 'Automatically adaptive, stabilized finite element method via residual minimization for heterogeneous, anisotropic advection–diffusion–reaction problems'. *Computer Methods in Applied Mechanics and Engineering* **385**:114027.

J.-B. Clavaud, et al. (2008). 'Permeability anisotropy and its relations with porous medium structure'. *Journal of Geophysical Research* **113**(B1).

J. M. F. Clout (2006). 'Iron formation-hosted iron ores in the Hamersley Province of Western Australia'. *Applied Earth Science* **115**(4):115–125.

B. Cockburn, et al. (2012). *Discontinuous Galerkin methods: theory, computation and applications*, vol. 11. Springer Science & Business Media.

B. Cockburn & C. W. Shu (1998). 'The local discontinuous galerkin method for time-dependent convection-diffusion systems'. *SIAM Journal on Numerical Analysis* **35**(6):2440–2463.

A. Cohen, et al. (2012). 'Adaptivity and variational stabilization for convection-diffusion equations'. *ESAIM: Mathematical Modelling and Numerical Analysis* **46**(5):1247–1273.

C. Coley & J. A. Evans (2018). 'Variational multiscale modeling with discontinuous subscales: analysis and application to scalar transport'. *Meccanica* **53**(6):1241–1269.

J. Conliffe (2016). 'Geology and geochemistry of high-grade iron-ore deposits in the Kivivic Timmins and Ruth Lake areas, Western Labrador.'. Tech. rep., Current Research, Newfoundland and Labrador Department of Natural Resources, Geological Survey.

M. Crouzeix & F. Lisbona (1984). 'The convergence of variable-stepsize, variable-formula, multistep methods'. *SIAM journal on numerical analysis* **21**(3):512–534.

S. Dai, et al. (2019). 'Permeability anisotropy and relative permeability in sediments from the National Gas Hydrate Program Expedition 02, offshore India'. *Marine and Petroleum Geology* **108**:705–713.

L. Demkowicz & J. Gopalakrishnan (2010). 'A class of discontinuous Petrov–Galerkin methods. Part I: The transport equation'. *Computer Methods in Applied Mechanics and Engineering* **199**(23-24):1558–1572.

L. Demkowicz & J. Gopalakrishnan (2011). 'A class of discontinuous Petrov–Galerkin methods. II. Optimal test functions'. *Numerical Methods for Partial Differential Equations* **27**(1):70–105.

L. Demwkowicz & J. Gopalakrishnan (2011). 'Analysis of the DPG Method for the Poisson equation'. *SIAM Journal on Numerical Analysis* **49**(5/6):1788–1809.

D. A. Di Pietro & A. Ern (2011). *Mathematical aspects of discontinuous Galerkin methods*, vol. 69. Springer Science & Business Media.

W. Dörfler (1996). 'A convergent adaptive algorithm for Poisson's equation'. *SIAM Journal on Numerical Analysis* **33**(3):1106–1124.

J. Douglas, Jr. & T. Dupont (1976). 'Interior penalty procedures for elliptic and parabolic Galerkin methods'. In *Computing methods in applied sciences (Second Internat. Sympos., Versailles, 1975)*, Lecture Notes in Phys., Vol. 58, pp. 207–216. Springer, Berlin.

A. Ern & J. Proft (2005). 'A posteriori discontinuous Galerkin error estimates for transient convection-diffusion equations'. *Applied Mathematics Letters* **18**(7):833–841.

A. Ern, et al. (2009). 'A discontinuous Galerkin method with weighted averages for advection–diffusion equations with locally small and anisotropic diffusivity'. *IMA Journal of Numerical Analysis* **29**(2):235–256.

A. Ern & M. Vohralík (2010). 'A posteriori error estimation based on potential and flux reconstruction for the heat equation'. *SIAM Journal on Numerical Analysis* **48**(1):198–223.

A. Erőss, et al. (2018). 'Uranium in groundwater–The importance of hydraulic regime and groundwater flow system's understanding'. *Journal of environmental radioactivity* **195**:90–96.

T. Führer, et al. (2021). 'Analysis of backward Euler primal DPG methods'. *Computational Methods in Applied Mathematics* **21**(4):811–826.

K. Garikipati & T. Hughes (2000). 'A variational multiscale approach to strain localization–formulation for multidimensional problems'. *Computer Methods in Applied Mechanics and Engineering* **188**(1-3):39–60.

D. D. Garven (1985). 'Groundwater flow and heat transport in sedimentary basins'. *Annual Review of Earth and Planetary Sciences* **13**:339–376.

D. D. Garven, et al. (1993). 'Groundwater flow and heat transport in sedimentary basins: Implications for the genesis of hydrothermal ore deposits'. *Reviews of Geophysics* **31**(3):441–488.

C. Geuzaine & J.-F. Remacle (2009). 'Gmsh: A 3-D finite element mesh generator with built-in pre- and post-processing facilities'. *International Journal for Numerical Methods in Engineering* **79**(11):1309–1331.

Y. Ghaffari Motlagh, et al. (2013). 'Simulation of laminar and turbulent concentric pipe flows with the isogeometric variational multiscale method'. *Computers & Fluids* **71**:146–155.

J. F. Giraldo & V. M. Calo (2023). 'A variational multiscale method derived from an adaptive stabilized conforming finite element method via residual minimization on dual norms'. *Computer Methods in Applied Mechanics and Engineering* p. 116285.

L. Grose, et al. (2021). 'LoopStructural 1.0: time-aware geological modelling'. *Geoscientific Model Development* **14**(6):3915–3937.

M. Hajipour, et al. (2018). 'On the accurate discretization of a highly nonlinear boundary value problem'. *Numerical Algorithms* **79**(3):679–695.

T. J. Hughes (1995). 'Multiscale phenomena: Green's functions, the Dirichlet-to-Neumann formulation, subgrid scale models, bubbles and the origins of stabilized methods'. *Computer methods in applied mechanics and engineering* **127**(1-4):387–401.

T. J. Hughes, et al. (1998). 'The variational multiscale method—a paradigm for computational mechanics'. *Computer Methods in Applied Mechanics and Engineering* **166**(1-2):3–24.

T. J. Hughes, et al. (2000). 'Large eddy simulation and the variational multiscale method'. *Computing and visualization in science* **3**(1):47–59.

T. J. Hughes, et al. (2006). 'A multiscale discontinuous Galerkin method with the computational structure of a continuous Galerkin method'. *Computer Methods in Applied Mechanics and Engineering* **195**(19-22):2761–2787.

T. J. R. Hughes, et al. (1989). 'A new finite element formulation for computational fluid dynamics: VIII. The Galerkin/Least-Squares method for advection-diffusive equations'. *Comput. Methods Appl. Mech. Engrg.* **73**:173–189.

K. E. Jansen, et al. (2000). 'A generalized-$\alpha$ method for integrating the filtered Navier–Stokes equations with a stabilized finite element method'. *Computer Methods in Applied Mechanics and Engineering* **190**(3):305–319.

C. Johnson & J. Pitkäranta (1986). 'An analysis of the discontinuous Galerkin method for a scalar hyperbolic equation'. *Mathematics of computation* **46**(173):1–26.

R. Juanes & T. W. Patzek (2005). 'Multiscale-stabilized solutions to one-dimensional systems of conservation laws'. *Computer methods in Applied Mechanics and engineering* **194**(25-26):2781–2805.

Z. S. Kahou, et al. (2021). 'Mineralogical and chemical characterization of supergene copper-bearing minerals: Examples from Chile and Burkina Faso'. *Ore Geology Reviews* **133**:104078.

D. A. Kepert (2018). 'The mapped stratigraphy and structure of the mining area C region, Hamersley Province'. Tech. Rep. 185, Geological Survey of Western Australia, Perth, Western Australia. 282p.

J. Kidder, et al. (2020). 'A review of hydrogeochemical mineral exploration in the Atacama Desert, Chile'. *Ore Geology Reviews* **124**:103562.

J. Knight, et al. (2018). 'Discovery, Geologic Setting, and Controls on Iron Mineralization, South Flank, Western Australia'. In *Metals, Minerals, and Society*. Society of Economic Geologists (SEG).

F. E. Kyburg, et al. (2022). 'Incompressible flow modeling using an adaptive stabilized finite element method based on residual minimization'. *International Journal for Numerical Methods in Engineering* **123**(8):1717–1735.

N. A. Labanda, et al. (2022). 'A spatio-temporal adaptive phase-field fracture method'. *Computer Methods in Applied Mechanics and Engineering* **392**:114675.

D. F. Lascelles (2002). 'A New Look at Old Rocks - An Alternative Model for the Origin of In Situ Iron Ore Deposits Derived From Banded Iron-Formation'. In R. Holmes (ed.), *Iron Ore 2002 Conference*, vol. 7/2002, pp. 107–126, Australia. Australasian Institute of Mining and Metallurgy. A New Look at Old Rocks - An Alternative Model for the Origin of In Situ Iron Ore Deposits Derived From Banded Iron-Formation ; Conference date: 01-01-2002.

D. F. Lascelles (2016). 'The origin of terrestrial pisoliths and pisolitic iron ore deposits: Raindrops and sheetwash in a semi-arid environment'. *Sedimentary Geology* **341**:232–244.

X. Mangenot, et al. (2019). 'Thermal and exhumation histories of the northern subalpine chains (Bauges and Bornes–France): Evidence from forward thermal modeling coupling clay mineral diagenesis, organic maturity and carbonate clumped isotope ($\Delta 47$) data'. *Basin Research* **31**(2):361–379.

A. Masud & R. Khurram (2004). 'A multiscale/stabilized finite element method for the advection–diffusion equation'. *Computer Methods in Applied Mechanics and Engineering* **193**(21-22):1997–2018.

W. F. Mitchell (2013). 'A collection of 2D elliptic problems for testing adaptive grid refinement algorithms'. *Applied mathematics and computation* **220**:350–364.

D. Moro, et al. (2012). 'A hybridized discontinuous Petrov–Galerkin scheme for scalar conservation laws'. *International journal for numerical methods in engineering* **91**(9):950–970.

R. C. Morris (1980). 'A textural and mineralogical study of the relationship of iron ore to banded iron-formation in the Hamersley iron province of Western Australia'. *Economic Geology* **75**:184–209.

R. C. Morris (1982). 'Petrological aspects of the Marandoo iron ore deposit'. Tech. rep., CSIRO, Perth.

R. C. Morris (1985). *Handbook of strata-bound and stratiform ore deposits*, vol. 13, chap. Genesis of iron ore in banded iron-formation by supergene and supergene-metamorphic processes – a conceptual model, pp. 73–235. Elsevier, Amsterdam.

A. H. Niemi, et al. (2011). 'Discontinuous Petrov-Galerkin method based on the optimal test space norm for one-dimensional transport problems'. *Procedia Computer Science* **4**:1862–1869. Proceedings of the International Conference on Computational Science, ICCS 2011.

A. H. Niemi, et al. (2013a). 'Automatically stable discontinuous Petrov–Galerkin methods for stationary transport problems: Quasi-optimal test space norm'. *Computers & Mathematics with Applications* **66**(10):2096–2113. ICNC-FSKD 2012.

A. H. Niemi, et al. (2013b). 'Discontinuous Petrov–Galerkin method based on the optimal test space norm for steady transport problems in one space dimension'. *Journal of Computational Science* **4**(3):157–163. Agent-Based Simulations, Adaptive Algorithms, ICCS 2011 Workshop.

J. E. Ortiz, et al. (1980). 'Numerical simulation of groundwater flow and heat transport in the Paradox Basin, Utah'. *Water Resources Research* **16**(6):1057–1071.

P. Panja, et al. (2021). 'Influence of permeability anisotropy and layering on geothermal battery energy storage'. *Geothermics* **90**:101998.

C. S. Perring (2021). 'Petrography of martite–goethite ore and implications for ore genesis, South Flank, Hamersley Province, Western Australia'. *Australian Journal of Earth Sciences* **68**(6):782–798.

C. S. Perring, et al. (2020). 'A New Fluid-Flow Model for the Genesis of Banded Iron Formation-Hosted Martite-Goethite Mineralization, with Special Reference to the North and South Flank Deposits of the Hamersley Province, Western Australia'. *Economic Geology* **115**(3):627–659.

A. Pestiaux, et al. (2014). 'Discontinuous Galerkin finite element discretization of a strongly anisotropic diffusion operator'. *International Journal for Numerical Methods in Fluids* **75**(5):365–384.

E. R. Ramanaidou & R. C. Morris (2010). 'A synopsis of the channel iron deposits of the Hamersley Province, Western Australia'. *Applied Earth Science* **119**:56–59.

E. R. Ramanaidou & M. Wells (2014). 'Sedimentary Hosted Iron Ores'. In *Treatise on Geochemistry*, pp. 313–355. Elsevier.

W. H. Reed & T. R. Hill (1973). 'Triangular mesh methods for the neutron transport equation'. Tech. rep., Los Alamos Scientific Lab., N. Mex.(USA).

B. Rivière (2008). *Discontinuous Galerkin methods for solving elliptic and parabolic equations: theory and implementation*. SIAM.

N. V. Roberts & S. Henneking (2020). 'Time-stepping DPG formulations for the heat equation'. *Computers and Mathematics with Applications* .

S. Rojas, et al. (2021). 'Goal-oriented adaptivity for a conforming residual minimization method in a dual discontinuous Galerkin norm'. *Computer Methods in Applied Mechanics and Engineering* **377**:113686.

C. Sanchez, et al. (2017). 'Exhumation history and timing of supergene copper mineralisation in an arid climate: New thermochronological data from the Centinela District, Atacama, Chile'. *Terra Nova* **30**(1):78–85.

G. Sangalli (2004). 'A discontinuous residual-free bubble method for advection-diffusion problems'. *Journal of engineering mathematics* **49**(2):149–162.

N. Sergeev, et al. (2017). 'The Paroo Station Mine supergene lead deposits, Western Australia: geological and geochemical constraints'. *Ore Geology Reviews* **80**:564–593.

K. Shahbazi (2005). 'An explicit expression for the penalty parameter of the interior penalty method'. *Journal of Computational Physics* **205**(2):401–407.

B. M. Simonson, et al. (1993). 'Lithology and proposed revisions in stratigraphic nomenclature of the Wittenoom Formation (Dolomite) and overlying formations, Hamersley Group, Western Australia'. Tech. Rep. 34, Geological Survey of Western Australia, Perth, Western Australia. 16p.

B. Sommerville, et al. (2014). 'Mineral resource estimation of the Brockman 4 iron ore deposit in the Pilbara region'. *Applied Earth Science* **123**(2):135–145.

S. K. Stoter, et al. (2022). 'Discontinuous Galerkin methods through the lens of variational multiscale analysis'. *Computer Methods in Applied Mechanics and Engineering* **388**:114220.

T. Poulet, J.F. Giraldo, E. Ramanaidou, A. Piechocka, & V.M. Calo (2023). 'Paleo-stratigraphic permeability anisotropy controls supergene mimetic martite goethite deposits'. *Basin Research* **35**(2):572–591.

D. Taylor, et al. (2001). 'Genesis of high-grade hematite orebodies of the Hamersley Province, Western Australia'. *Economic Geology* **96**(4):837–873.

J. Tóth (2016). 'The evolutionary concepts and practical utilization of the tóthian theory of regional groundwater flow'. *Int. J. Earth Envrion. Sci* **1**:111.

U. S. G. S. USGS (2022). 'Iron Ore Statistics and Information'. https://www.usgs.gov/centers/national-minerals-information-center/iron-ore-statistics-and-information. Accessed: 2022/01/28.

P. M. Vasconcelos, et al. (2013). '40Ar/39Ar and (U–Th)/He – 4He/3He geochronology of landscape evolution and channel iron deposit genesis at Lynn Peak, Western Australia'. *Geochimica et Cosmochimica Acta* **117**:283–312.

A. D. Webb, et al. (2003). 'From banded iron-formation to iron ore: geochemical and mineralogical constraints from across the Hamersley Province, Western Australia'. *Chemical Geology* **197**(1-4):215–251.

D. E. White (1971). 'Numerical analysis of groundwater flow in the White Pine copper deposit, Michigan'. *Economic Geology* **66**(3):487–512.

D. A. Wood & D. F. Hewett (1984). 'The role of groundwater in the formation of Mississippi Valley-type lead-zinc deposits'. *Economic Geology* **79**(4):714–736.

L. Zhu & D. Schötzau (2010). 'A robust a posteriori error estimate for hp-adaptive DG methods for convection–diffusion equations'. *IMA Journal of Numerical Analysis* **31**(3):971–1005.

J. Zitelli, et al. (2011). 'A class of discontinuous Petrov–Galerkin methods. Part IV: The optimal test norm and time-harmonic wave propagation in 1D'. *Journal of Computational Physics* **230**(7):2406–2432.
ΩŁoś et al.

M. Łoś, et al. (2021). 'DGIRM: Discontinuous Galerkin based isogeometric residual minimization for the Stokes problem'. *Journal of Computational Science* **50**:101306.